Yang, Bowen (2021) *Mixed-numerology for radio access network slicing.* PhD thesis.

https://theses.gla.ac.uk/82683/

Copyright and moral rights for this work are retained by the author

A copy can be downloaded for personal non-commercial research or study, without prior permission or charge

This work cannot be reproduced or quoted extensively from without first obtaining permission in writing from the author

The content must not be changed in any way or sold commercially in any format or medium without the formal permission of the author

When referring to this work, full bibliographic details including the author, title, awarding institution and date of the thesis must be given

Enlighten: Theses
https://theses.gla.ac.uk/
research-enlighten@glasgow.ac.uk

Mixed-Numerology for Radio Access Network Slicing

Bowen Yang

Submitted in fulfilment of the requirements for the
Degree of Doctor of Philosophy

School of Engineering
College of Science and Engineering
University of Glasgow

December 2021

Abstract

Network slicing is a sustainable solution to support the various service types in future networks. In general, network slicing is composed of core network slicing and radio access network (RAN) slicing. The former can be realized by allocating dedicated virtualized core network functionalities to specific slices. Similarly, RAN slicing includes the virtualization and allocation of the limited RAN resources. From the physical layer perspective, supporting RAN slicing implies the need of unique radio-frequency (RF) and baseband (BB) configurations, *i.e.*, numerology, for each slice to fulfil its quality of service requirements. To support such a heterogeneous mixed-numerology (MN) system, the transceiver architecture and widely used signal processing algorithms in the traditional single-service system need to be significantly changed. A clear understanding of mixed-numerology signals multiplexing and isolation is of importance to enable spectrum and computation efficient RAN slicing. Meanwhile, an effective channel estimation is the guarantee of performing almost all receiver signal processing. Fundamental channel estimation investigations also constitute a crucial piece of MN study.

This thesis aims to systematically investigate the OFDM-based MN wireless communication systems in terms of system modeling, channel equalization/estimation, and power allocation. First, a comprehensive mixed-numerology framework with two numerologies is proposed and characterized by physical layer parameters. According to the BB and RF configurations imparities among numerologies, four scenarios are categorized and elaborated on the configuration relationships of different numerologies. System models considering the most generic scenario are established for both uplink and downlink transmissions. Two theorems are proposed as the basis of MN algorithms design, which generalize the original circular convolution property of the discrete Fourier transform. The proposed theorems verifies the feasibility of the one-tap channel equalization in MN systems. However, they also indicate that both BB and RF configuration differences result in inter-numerology-interference (INI). Besides, severe signal distortion may occur when the transmitter and receiver numerologies are different.

Therefore, a pre-coding algorithm is designed by utilizing the theorems to compensate the system degradation resulting from the signal distortion. INI cancellation algorithms are proposed based on collaboration detection scheme and joint numerologies signal models for downlink and uplink, respectively. Numerical results shows that the proposed algorithms are able to significantly improve the system performance.

Another objective of this thesis is to verify the effectiveness of the existing channel estimation algorithms and to develop new ones in the presence of MN. To achieve these goals, three channel estimation methods, *i.e.*, least-square linear interpolation, least-square '*sinc*' interpolation, and minimum mean square error '*sinc*' interpolation are implemented and theoretically analyzed in both single-user and multi-user scenarios. The analysis reveals that the pilot signal to noise ratio, pilot distance, and position of pilot signals jointly affect the channel estimation. In particular, a signal distortion factor caused by the RF configuration difference is spotted to seriously affect the channel estimation performance, whose values are mainly decided by the degree of configuration mismatch. On the other hand, INI also degrades the channel estimation in the MN system. The existence of interference-free subcarriers is demonstrated based on the derived closed-form expression of the INI. Pilot design principles in terms of pilot signal placement are developed according to the analyses. Numerical results shows that minimum mean square error based channel estimation has the best performance and robustness to the configuration mismatch. In addition, the proposed pilot design principles could produce comparable channel estimation results with the legacy OFDM systems where no INI and signal distortion exist.

The two problems associated with the MN system, *i.e.*, signal distortion and INI, could negatively affect the power distribution of the received MN signals, and the system performance in terms of spectrum efficiency may be seriously degraded. Consequently, it becomes outstandingly important to introduce an efficient subcarrier-level power allocation scheme in such kinds of systems to counter the performance degradation caused by the configuration mismatch. As such, this thesis makes the attempt to extend the two-numerology model to contain 'M' different numerologies. Based on the model, closed-form expressions of desired signal, interference, and noise are derived. The derivation shows that interference generated from different numeroloies are linearly superimposed in the frequency domain. The distribution of signal-to-interference-plus-noise-ratio (SINR) is analyzed theoretically. An iterative convex approximation power allocation algorithm is proposed by applying the derived SINR. Results show that the power allocation algorithm contributes to remarkable spectrum efficiency improvement compare to the other schemes, and an extra subband filtering process could bring about even higher performance.

The work presented in this thesis provides guidance for multi-numerology system design in terms of parameter selection, and the frame structure and algorithms design. Moreover, it presents a solution as to how the radio access network slicing can be underpinned in the physical layer in a spectrum-efficient way.

University of Glasgow

College of Science & Engineering

Statement of Originality

Name: Bowen Yang
Registration Number:

I certify that the thesis presented here for examination for a PhD degree of the University of Glasgow is solely my own work other than where I have clearly indicated that it is the work of others (in which case the extent of any work carried out jointly by me and any other person is clearly identified in it) and that the thesis has not been edited by a third party beyond what is permitted by the University's PGR Code of Practice.

The copyright of this thesis rests with the author. No quotation from it is permitted without full acknowledgement.

I declare that the thesis does not include work forming part of a thesis presented successfully for another degree.

I declare that this thesis has been produced in accordance with the University of Glasgow's Code of Good Practice in Research.

I acknowledge that if any issues are raised regarding good research practice based on the review of the thesis, the examination may be postponed pending the outcome of any investigation of the issues.

Signature: ....Bowen Yang...............
Date: ....07/Dec/2021....................

List of Publications

Journal Papers

- **Yang, B.**, Zhang, L., Onireti, O., Xiao, P., Imran, M. A. and Tafazolli, R. (2020) Mixed-numerology signals transmission and interference cancellation for radio access network slicing. IEEE Transactions on Wireless Communications, 19(8), pp. 51321-5147.

- **Yang, B.**, Mao, J., Ijaz, A. , Zhang, L., Sun, Y., Wang, R., and Imran, M. A. Uplink Channel Estimation and Pilot Design for Radio-Frequency Differed Mixed-Numerology Systems. (Under Revision from IEEE Transactions on Vehicular Technology)

- **Yang, B.**, Mao, J., Zhang, L., Sun, Y., Wang, R., and Imran, M. A. Power Allocation in the Presence of Mixed-numerology. (Under Revision from IEEE Communication Letters)

- Sun, Y., Zhang, L., Feng, G., **Yang, B.**, Cao, B. and Imran, M. A. (2019) Blockchain-enabled wireless internet of things: performance analysis and optimal communication node deployment. IEEE Internet of Things Journal, 6(3), pp. 5791-5802.

- Wang, R., Sun, Y., Imran, M. A., **Yang, B.**, Zhang, L. A Novel Handover Scheme for Millimeter Wave Network: An Approach of Integrating Reinforcement Learning and Optimization. (To be submitted)

Book Chapters

- **Yang, B.**, Zhang, X., Zhang, L., Farhang, A., Xiao, P.andImran, M. A.(2020) Windowed OFDM for mixed-numerology 5G and beyond systems. In: Zhang, L., Farhang, A., Feng, G. and Onireti, O. (eds.) Radio Access Network Slicing and Virtualization for 5G Vertical Industries. Wiley.

- **Yang, B.**, Zhang, L., Deng, Y., Qiao, D. and Imran, M.(2018) Algorithms and performance analysis for narrowband internet of things (NB-IoT) and broadband LTE coexisting system. In: Wu, Y.,Huang, H.,Wang, C.-X. and Pan, Y.(eds.) 5G-Enables Internet of Things. CRC Press.

Conference Papers

- **Yang, B.**, Zhang, L. , Qiao, D., Zhao, G. and Imran, M. A. (2019) Narrowband Internet of Things (NB-IoT) and LTE Systems Co-existence Analysis. In: IEEE GLOBECOM 2018, Abu Dhabi, United Arab Emirates, 09-13 Dec 2018.
- **Yang, B.**, Molu, M. and Zhang, L. (2018) Advanced Hybrid Beamforming Design for MIMO Systems. In: 10th IEEE Sensor Array and Multichannel Signal Processing Workshop (SAM 2018), Sheffield, UK, 8-11 July 2018, pp. 80-83.
- Liu, Y., Zhang, L., **Yang, B.**, Guo, W. and Imran, M. A. (2020) Programmable Wireless Channel for Multi-user MIMO Transmission Using Meta-surface. In: IEEE GLOBECOM 2019, Waikoloa, HI, USA, 09-13 Dec 2019.
- Sun, Y. , Zhang, L. , Feng, G., **Yang, B.**, Cao, B. and Imran, M. A. (2020) Performance Analysis for Blockchain Driven Wireless IoT Systems Based on Tempo-Spatial Model. In: CyberC 2019 International Conference on Cyber-Enabled Distributed Computing and Knowledge Discovery, Guilin, China, 17-19 Oct 2019, pp. 348-353.

Contents

Abstract i

Statement of Originality v

List of Publications vii

List of Tables xiii

List of Figures xv

List of Acronyms xix

Acknowledgements xxiii

1 Introduction 1
- 1.1 Network Slicing 1
  - 1.1.1 Core Network Slicing 3
  - 1.1.2 Radio Access Network Slicing 4
  - 1.1.3 Mixed-Numerology 5
- 1.2 Motivation 6
- 1.3 Objectives 7
- 1.4 Research Contributions 9
- 1.5 Thesis Outline 10

2 Background and Literature Review 13
- 2.1 Overview of Multiple Access Techniques 13
  - 2.1.1 Frequency Division Multiple Access 14
  - 2.1.2 Time Division Multiple Access 14
  - 2.1.3 Code Division Multiple Access 14
  - 2.1.4 Space Division Multiple Access 15
  - 2.1.5 Orthogonal Frequency Division Multiple Access 15
- 2.2 Overview of Current Radio Access Networks 16

2.2.1 LTE and LTE-Advanced 16
2.2.2 NB-IoT 17
2.2.3 5G New Radio 18
2.3 Overview of Advanced Waveforms 21
2.3.1 Windowed-OFDM 22
2.3.2 Filtered-OFDM 23
2.4 Overview of Channel Estimation Methods 24
2.5 State-of-the-Art in Mixed-Numerology Systems 25
2.5.1 Baseband-Differed Mixed-Numerology 25
2.5.2 Radio Frequency-Differed Mixed-Numerology 26
2.6 Relevant Techniques 27
2.6.1 Realization of OFDM 27
2.6.2 Sampling 30

3 Mixed-Numerology Framework, Signals Transmission, and Interference Cancellation 37
3.1 Introduction 37
3.2 Mixed-Numerology Framework Construction 40
3.2.1 Scenarios Categorization 41
3.2.2 System Configurations 43
3.3 Generalized Circular Convolution Properties 47
3.4 Uplink Mixed-Numerology System 51
3.4.1 DBDR System Model 51
3.4.2 One-tap Channel Equalization 54
3.4.3 Signal Distortion Analysis and Proposed Power Compensation Algorithm 54
3.4.4 INI Analysis and Cancellation for SBDR Scenario 56
3.5 Downlink Mixed-Numerology System 58
3.5.1 DBDR System Model, Equalization, and Power Compensation Algorithm 58
3.5.2 SBDR INI Analysis and Cancellation 60
3.6 Numerical Results 61
3.7 Conclusions 67

4 Mixed-Numerology Channel Estimation and Pilot Design 69
4.1 Introduction 69
4.2 Preliminary: Signal Structure 71
4.3 Single-User Model and Channel Estimation 73
4.3.1 SU System Model 73

4.3.2 Channel Estimation in the SU Scenario 75
4.3.3 Pilot Design in the SU Scenario 79
4.4 Multi-User Model and Channel Estimation 80
4.4.1 MU System Model 81
4.4.2 Channel Estimation in the MU Scenario 82
4.4.3 Pilot Design in the MU Scenario 85
4.5 Numerical Results 86
4.5.1 Results for the SU Scenario 86
4.5.2 Results for the MU Scenario 90
4.6 Conclusion 92

5 Power Allocation in the Presence of Mixed-Numerology 93
5.1 Introduction 93
5.2 System Model 94
5.2.1 Transmitter Baseband Processing of Numerology i 95
5.2.2 Equivalent RF Processing and MN Multiplexing 96
5.2.3 Receiver Baseband Processing of Numerology i 98
5.3 SINR Analysis and Signal Power Allocation 98
5.3.1 SINR Analysis 98
5.3.2 Subcarrier-Level Power Allocation 101
5.4 Numerical Results 103
5.5 Conclusion 106

6 Conclusions and Future Trends 107
6.1 Conclusions 107
6.2 Future Trends 109
6.2.1 Extension of Current Researches 109
6.2.2 Promising Future Directions 110

Appendices 113

A Generality Proof of the Two-Slice Model 113

B Proof of Theorem 1 115

C Proof of Theorem 2 117

D Proof of Eq. (3.27) and Eq. (3.28) 119

E Derivation of Eq. (4.43) and Eq. (4.44) 121

List of Tables

3.1 List of Important Symbols 40

4.1 CE error component values for LSLI, $Q = 1$ 88
4.2 CE error component values for LSLI, $Q = 5$ 88

5.1 Configurations of all numerologies 103

List of Figures

1.1 Illustration of vertical network slicing. 2

1.2 Illustration of horizontal network slicing. 2

1.3 Core network slicing architecture with SDN and NFV. 3

1.4 Radio access network slicing architecture. 4

2.1 Operation modes of NB-IoT, where the blue blocks indicate LTE subcarriers, and the other colors indicate the subcarriers allocated to NB-IoT users in different operation modes. 18

2.2 Typical operation scenario for a 5G wireless communication system. 19

2.3 Power spectral density comparison of the candidate 5G waveforms. 21

2.4 Comparison between CP-OFDM symbols and W-OFDM symbols, where the roll-off portion of adjacent W-OFDM symbols overlaps with each other. 22

2.5 Comparison between CP-OFDM symbols and F-OFDM symbols, where well designed filters could help reducing the ISI between adjacent F-OFDM symbols to a negligible level. 23

2.6 Spectrum divisions of FDM and OFDM. 28

2.7 A simplified process to generate OFDM symbols in the transmitter. 29

2.8 OFDM signal demodulation in the receiver. 29

2.9 A simplified process for signal converts from analog to digital with f_s being the sampling rate. 31

2.10 A *zero-order hold* process for signal converts from digital to analog with $\dot{f}_s$ being the sampling rate. 32

2.11 The recover of $\mathbf{s}[n]$ via normal sampling process. 32

2.12 Normal up-sampling process with $Q_u = 2$. 33

2.13 Unintentional up-sampling of $\mathbf{r}(t)$. The sample duration before and after up-sampling is ΔT and $\Delta T'$, respectively, and the up-sampling rate is $Q_u = 3$. 34

2.14 Unintentional down-sampling of $\mathbf{r}(t)$. The sample duration after down-sampling is $\Delta T''$ with down-sampling rate being $Q_d = 2$. . . 35

3.1 Spectrum allocation of the two slices within the system bandwidth: $B_1 = M_1 \Delta f_1$ for slice1 and $B_2 = M_2 \Delta f_2$ for slice2. 43

3.2 Frame structure example of DBDR system with two slices: $\Delta T_2 = 2\Delta T_1$ (*i.e.*, $O = 2$ and $\Delta f_1 = 2\Delta f_2$). At UE side, DFT size $N_{U1} = 16$, $N_{U2} = 4$; RF sampling rate $S_{U1} = 8S_{U2}$, (*i.e.*, $Q = 8$). At the BS side, DFT size $N_{B1} = 16$, $N_{B2} = 32$; RF sampling rate $S_{B1} = S_{B2}$ (Note that the two slices are frequency domain multiplexed). 44

3.3 Transmitter and receiver block diagram of DBDR MN system for uplink transmission. (Note that the downlink transmission case is similar, thus, is omitted in this thesis.) 52

3.4 Filter and phase shift frequency responses versus subcarrier index ($M_2 = 12$): a) Filter frequency response diag$|\mathbf{G}_2^H \mathbf{G}_2|^2$ (F-OFDM system [82]); b), Phase shift diag$|\mathbf{\Lambda}_0|^2$ response with $Q = 2, 4, 8, 16$, and joint response diag$|\mathbf{G}_2^H \mathbf{G}_2 \mathbf{\Lambda}_0|^2$ (in red, where we consider $Q = 16$.). 55

3.5 SINR versus subcarrier index with different guard band ΔB_1 for both F-OFDM and OFDM waveforms for uplink transmission (Red lines are for OFDM and blue dashed lines are for F-OFDM). . . . 62

3.6 SINR versus subcarrier index with and without proposed algorithms for both F-OFDM and OFDM waveforms in uplink transmission (Red lines are for slice1 and blue lines are for slice2). 63

3.7 BER versus E_b/N_o with and without proposed algorithms for SBDR scenario in uplink transmission (Red lines are for slice1 and blue lines are for slice2). 64

3.8 SINR versus subcarrier index with and without proposed algorithms for both F-OFDM and OFDM waveforms in downlink transmission (Red lines are for slice1 and blue lines are for slice2). 65

3.9 SINR versus subcarrier index in downlink transmission with different guardband (Red: OFDM, Blue: Proposed). 66

3.10 BER versus E_b/N_o with and without proposed algorithms for SBDR scenario in downlink transmission (Red lines are for slice1 and blue lines are for slice2). 66

4.1 Symbol structure of the two different numerologies, where numerology 1 is the low sampling rate numerology with $N_L = 5$ and numerology 2 is the high sampling rate numerology with $N_H = 10$. 72

4.2 Mixed-numerology system model in single-user scenario, where yellow and blue blocks denote the components of numerology 1 and numerology 2 devices, respectively. The red dish boxes represent the equivalent process which transforms the RF processing into digital domain. 73

4.3 Comb-type pilot pattern applied in this chapter. 75

4.4 $(\mathbf{\Gamma}^H\mathbf{\Gamma})^{-1}$ v.s. subcarrier index within 1 PRB, where $\mathbf{\Gamma}$ is the signal distortion factor caused by the sampling rate mismatch between the Tx and Rx. The entries of $\mathbf{\Gamma}$ is mainly decided by the upsampling rate, as shown in Eq. (4.8). 80

4.5 Mixed-numerology system model in multi-user scenario, where the yellow and blue blocks denote the components of numerology 1 and numerology 2 devices, respectively. The red dish boxes represent the equivalent process which transforms the RF processing into digital domain. 81

4.6 MSE of channel estimation v.s. PNR in the SU scenario. The green lines, red lines, and the blue lines corresponding to the results for LSLI, LS-DFT, and MMSE, respectively; while the black dash lines represent results in single-numerology scenarios. 87

4.7 MSE of channel estimation (with the unit of dB) v.s. Pilot distance L in the SU scenario. The green line, red line, and the blue line corresponding to the result for LSLI, LS-DFT, and MMSE, respectively; while the black dash lines represent results in single-numerology scenarios. 88

4.8 BER performance in the SU scenario with different CE methods and pilot position sets: $\mathbf{P}_{12}^{1} \in [1, 13, 25, 37, 49]$, $\mathbf{P}_{12}^{11} \in [11, 23, 35, 47, 59]$, and $\mathbf{P}_{12}^{12} \in [12, 24, 36, 48, 60]$. The results with pre-compensation are illustrated in black dash lines for comparison purpose. 89

4.9 MSE of channel estimation v.s. PNR in the MU scenario. The green lines, red lines, and the blue lines corresponding to the results for LSLI, LS-DFT, and MMSE, respectively; while the black dash lines are the results in single-numerology system, *i.e.*, without interference. 90

4.10 CE performance with interference cancellation (labeled as '$\mathbf{P}_{12}^{1}$ + IC') and interference free pilot transmission (labeled as '$\mathbf{P}_{12}^{2}$(IF)') in the MU scenario. The black dash lines are the results in the single-numerology system, *i.e.*, without interference. 91

5.1 Uplink model of an RF-differed mixed-numerology system. It composes of M numerologies in the Tx side and a BS numerology in the Rx side. 95
5.2 Example of mixed-numerology signal structure 97
5.3 SINR distribution among subcarriers with $B_g = [0.5, 1, 1.5]$PRB. Both OFDM and F-OFDM waveforms are simulated for comparison. Signal power is evenly allocated to all symbols with $E_b/N_0 = 20$ dB. 104
5.4 BER v.s. E_b/N_0 for each numerology by considering different configurations. The guard band is 1 PRB and the coding rate is 0.5. Signal power is evenly allocated in each $\mathbf{p^{(i)}}$, and the power offset is defined as $\rho = \frac{\mathbf{p^{(1)}}}{\mathbf{p^{(2)}}} = \frac{\mathbf{p^{(1)}}}{\mathbf{p^{(3)}}}$. 105
5.5 System spectrum efficiency versus E_b/N_0 with different power allocation schemes. In addition, the SE of a traditional single numerology OFDM system is presented as the benchmark. 106

A.1 Frequency band division for a MN system with three slices: slice1, slice2 and slice3. The bandwidth for slice2 is wide enough to prevent the interference between slice1 and slice3. 114
A.2 Frequency band division for a MN system with three slices: slice1, slice2 and slice3. The bandwidth for slice2 is very small so that the slice1 and slice3 suffer from the INI generated by each other. . 114

List of Acronyms

1G	First Generation
2G	Second Generation
3G	Third Generation
3GPP	3rd Generation Partnership Project
4G	Fourth Generation
5G	Fifth Generation
ABS	Almost Blank Subframe
ACF	Autocorrelation Function
ACI	Adjacent Channel Interference
ADC	Analog-to-Digital Converter
AMPS	Advanced Mobile Phone System
BB	Baseband
BF-OFDM	Block-Filtered Orthogonal Frequency Division Multiplex
BER	Bit Error Ratio
BS	Base Station
CA	Carrier Aggregation
CCI	Co-Channel Interference
CDMA	Code Division Multiple Access
CE	Channel Estimation
CN	Core Network
CNN	Convolutional Neural Network
CoMP	Coordinated Multi-Point
CP	Cyclic Prefix
CPS-OFDM	Circularly Pulse-Shaped Orthogonal Frequency Division Multiplex
CSI	Channel State Information
C-plane	Control Plane
DAC	Digital-to-Analog Converter
DBDR	Different Baseband Different Radio Frequency

DBSR	Different Baseband Same Radio Frequency
DFT	Discrete Fourier Transform
DFT-S-OFDM	DFT-Single-Carrier Orthogonal Frequency Division Multiplex
DSP	Digital Signal Processing
eICIC	Enhanced Inter-Cell Interference Coordination
eMBB	Enhanced Mobile Broadband
EPA	Extended Pedestrian A
ETU	Extended Typical Urban
E-UTRA	Evolved Universal Mobile Telecommunications System Terrestrial Radio Access
FBMC	Filter-Bank Multi-Carrier
FC	Fast-Convolution
FC-OFDM	Flexible Configured Orthogonal Frequency Division Multiplex
FDD	Frequency Domain Duplexing
FDM	Frequency Division Multiplexing
FDMA	Frequency Division Multiple Access
FFT	Fast Fourier Transform
F-OFDM	Filtered Orthogonal Frequency Division Multiplex
GB	Guard Band
GFDM	Generalized Frequency Division Multiplexing
GSM	Global System for Mobile Communications
G-CCP	Generalized Circular Convolution Property
G-CCP-DS	G-CCP with Down-Sampling
G-CCP-US	G-CCP with Up-Sampling
HARQ	Hybrid Automatic Repeat Request
ICI	Inter-Channel-Interference
IC	Interference Cancellation
IDFT	Inverse Discrete Fourier Transform
IF	Interference-Free
INI	Inter-Numerology-Interference
IoT	Internet of Things
ISI	Inter-Symbol-Interference
ISBI	Inter-Service-Band-Interference
ISubI	Inter-Service-Band-Interference
KPI	Key Performance Indicators
LCM	Least Common Multiplier
LI	Linear Interpolation
LS	Least Square

LTE	Long-Term Evolution
LTE-A	LTE-Advanced
MA	Multiple Access
MIMO	Multiple-Input-Multiple-Output
mmwave	Millimeter-Wave
mMTC	Massive Machine-Type Communications
MMSE	Minimum Mean Square Error
MN	Mixed-Numerology
MOCN	Multi-Operator Core Network
MR	Multi-Rate
MU	Multi-User
MVNO	Mobile Virtual Network Operator
NBI	Narrow-Band Interference
NB-IoT	Narrow-Band Internet-of-Things
NFV	Network Function Virtualization
NOMA	Non-Orthogonal Multiple Access
NS	Network Slicing
NS-ICF	Noise-Shaped Iterative Clipping and Filtering
NR	New Radio
OFDM	Orthogonal Frequency Division Multiplex
OFDMA	Orthogonal Frequency Division Multiple Access
OMA	Orthogonal Multiple Access
OoBE	Out of Band Emission
OSBE	Out of Subbabd Emission
O-CCP	Original Circular Convolution Property
PA	Power Amplifier
PAPR	Peak-to-Average-Power-Radio
PDMA	Pattern Division Multiple Access
PHY	Physical
PINR	Pilot Signal to Interference Plus Noise Ratio
PNR	Pilot Signal to Noise Ratio
PRB	Physical Resource Block
PSD	Power Spectral Density
PSK	Phase Shift Keying
QAM	Quadrature Amplitude Modulation
QoS	Quality of Service
RAN	Radio Access Network
RAT	Radio Access Technology

RB	Resource Block
RE	Resource Element
RF	Radio Frequency
RFID	Radio Frequency Identification
Rx	Receiver
SBDR	Same Baseband Different Radio Frequency
SBSR	Same Baseband Same Radio Frequency
SCALE	Successive Convex Approximation for Low Complexity
SCS	Subcarrier Spacing
SDMA	Space Division Multiple Access
SDN	Software-Defined Network
SFMC	Subband Filtered Multi-Carrier
SINR	Signal to Interference Plus Noise Ratio
SN	Single-Numerology
SNR	Signal to Noise Ratio
SOTA	State-of-the-Art
SU	Single-User
TDD	Time Domain Duplexing
TDMA	Time Division Multiple Access
TDM	Time Division Multiplexing
TTI	Transmit Time Interval
Tx	Transmitter
UE	User Equipment
UFMC	Universal Filtered Multi-Carrier
UHDV	Ultra-High-Definition Video
USRP	Universal Software Radio Peripheral
URLLC	Ultra-Reliable Low Latency Communications
U-plane	User-Plane
V2V	Vehicle-to-Vehicle
WCDMA	Wideband Code Division Multiple Access
W-OFDM	windowed Orthogonal Frequency Division Multiplex
ZF	Zero-Forcing

Acknowledgements

First and foremost, I would like to express my deepest gratitude to my supervisor, Dr. Lei Zhang, for his professional guidance and unconditional support throughout my entire Ph.D. study. I am grateful to him for always believing me and giving me the freedom to explore my researches to the greatest extent. He provided me with indispensable help whenever I needed it, not only as the supervisor but also as a friend. His wide knowledge, strong research enthusiasm and hard-working attitude have inspired me during all my Ph.D. period and will have a profound effect on my future career. It is extremely lucky to have Dr. Lei Zhang as my supervisor.

Secondly, I would like to thank Prof. Muhammad Ali Imran, who is my second supervisor, and Dr. Yao Sun, who is my friend and also my third supervisor, for their very good suggestions and key insights on each of my publications. I could not finish all of these works without their endless help.

I would also like to thank my girlfriend for supporting me, keeping me motivated, and relaxing my pressure and anxiety during the 'lock down' period. Without her, this journey would have been much harder and arduous. I would also like to acknowledge the support and help of all my friends. Thank you all for the discussions in and out of the university.

Finally, I would like to thank my family from the bottom of my heart. Thanks to my mother and father for their support and concerns, which are invaluable and irreplaceable for me to pursue my yearning lifestyle.

Chapter 1

Introduction

Nowadays, with the globally accelerating smartphone penetration, the wireless industry is facing the challenge of exploiting new services to expand the market [1]. Fortunately, opportunities are around the corner: the deployment of narrowband internet-of-things (NB-IoT) [2] implies the possibility to contain vertical industries into wireless networks. As such, the fifth-generation (5G) wireless network and beyond are supposed to facilitate a fully mobile and connected community, where a variety of use cases with very diverse requirements in terms of throughput, latency, reliability, and scalability are supported concurrently [3]. Based on the unique features and technical requirements of different services, three main use cases have been identified for 5G, i.e., enhanced mobile broadband (eMBB), massive machine-type communications (mMTC), and ultra-reliable low latency communications (URLLC) [4]. By connecting more devices instead of only mobile phones, the world around us could become more intelligent. On the other hand, it is becoming challenging to further improve the spectral utilization efficiency with current technologies. New approaches need to be found to meet the ever-increasing capacity demand. It is anticipated that the current network structure is not feasible and scalable enough to support a wide range of services when each has specific quality of service (QoS) requirements [5]. Network slicing (NS) is thus proposed as a sustainable solution, which enables design, deployment, customization, and optimization of different network slices on *a common infrastructure* [6, 7].

1.1 Network Slicing

NS is basically "to use virtualization technology to architect, partition and organize computing and communication resources of a physical infrastructure to enable flexible support of diverse use case realizations" [8]. With the broad consensus on the necessity of applying network slicing to support widely diverse services in future networks, there are different views on how sliced networks should be constructed. In [9] and [10], network slicing is considered as a necessary technology to allow different services, *i.e.*, in core network (CN) and radio access network (RAN), over the same physical infrastructure, as shown in Fig. 1.1. It

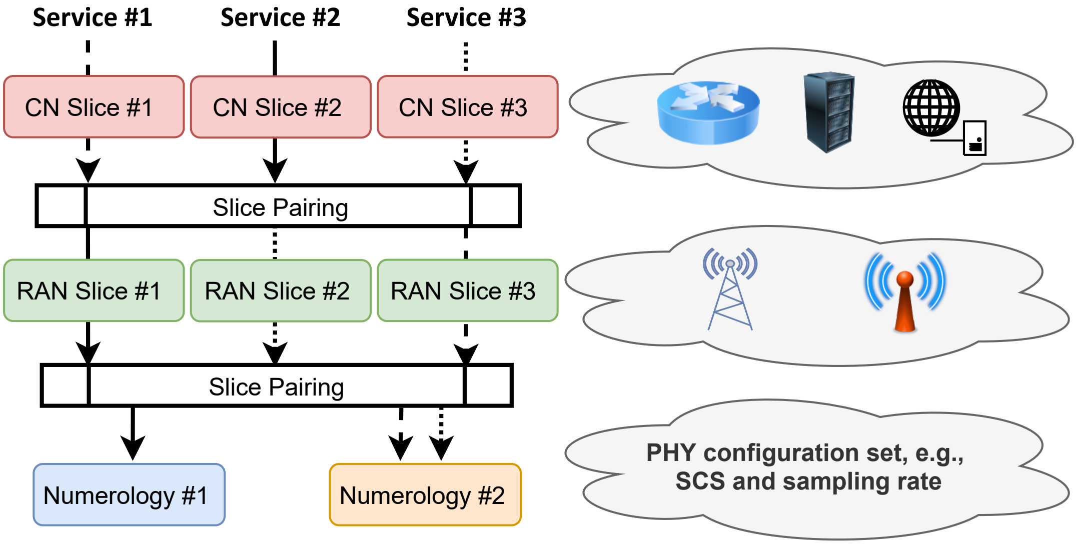
Service #1
Service #2
Service #3
CN Slice #1
CN Slice #2
CN Slice #3
Slice Pairing
RAN Slice #1
RAN Slice #2
RAN Slice #3
Slice Pairing
Numerology #1
Numerology #2
PHY configuration set, e.g., SCS and sampling rate

Figure 1.1: Illustration of vertical network slicing.

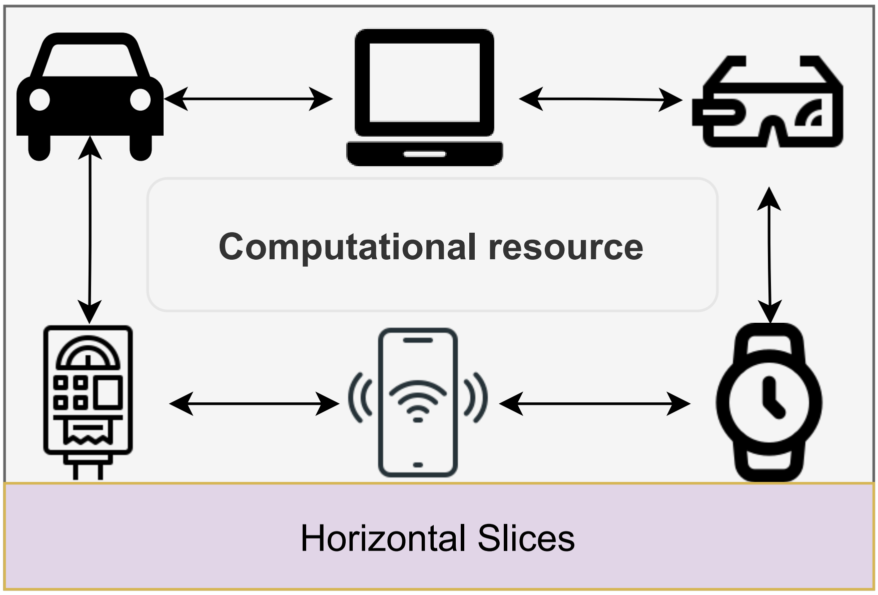
Computational resource
Horizontal Slices

Figure 1.2: Illustration of horizontal network slicing.

enables the sharing of radio resources, such as time and frequency, among different services/applications. While [8] further considers horizontal slicing, which targets sharing the computational capabilities among the devices in the same layer (*e.g.*, federated learning [11]), so that to enhance the user experience of low-end devices, as shown in Fig. 1.2. Note that ‘network slicing’ normally indicates vertical network slicing in academia and industry, which is also the scope of this thesis. For this reason, the term ’network slicing’ is used to indicate vertical network slicing in the rest of this thesis whenever no ambiguity arises.

1.1.1 Core Network Slicing

Core network, also known as the backbone network, is one of the most important parts of a wireless communication network to provide services to customers connected by access networks. It bridges the sub-networks and enables the information exchange among them. A core network in legacy wireless communication systems usually utilizes dedicated hardware to serve different verticals. However, such a static architecture cannot efficiently address modern networks’ increasing use cases. A programmable architecture and more scalable design are necessary for the core network to simultaneously provide various services over a common underlying physical infrastructure [12, 13].

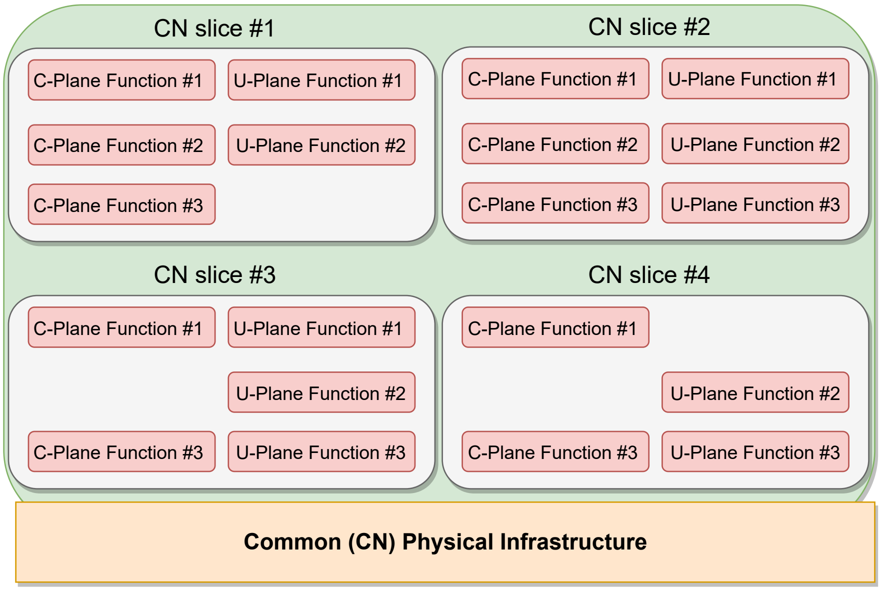
CN slice #1
C-Plane Function #1
U-Plane Function #1
C-Plane Function #2
U-Plane Function #2
C-Plane Function #3
CN slice #2
C-Plane Function #1
U-Plane Function #1
C-Plane Function #2
U-Plane Function #2
C-Plane Function #3
U-Plane Function #3
CN slice #3
C-Plane Function #1
U-Plane Function #1
U-Plane Function #2
C-Plane Function #3
U-Plane Function #3
CN slice #4
C-Plane Function #1
U-Plane Function #2
C-Plane Function #3
U-Plane Function #3
Common (CN) Physical Infrastructure

Figure 1.3: Core network slicing architecture with SDN and NFV.

As previously mentioned, NS is a way of networking on demand, which allows operators to cut out multiple virtual end-to-end networks on a unified infrastructure. From the core network perspective, a slice is composed of a collection of logical network functions that supports the communication service requirements of particular use case [14, 15], and each core network slice should be logically isolated. Software-defined network (SDN) and network function virtualization (NFV) are two dominant techniques for realizing network slicing in the core network [16–21]. In general, NFV virtualizes the network functionalities into software applications, built on which SDN is used to separately configure the control plane (C-plane) and the user plane (U-plane). The C-plane is moved from the network hardware and realized by software, which allows dynamic access and administration [22]. Thereby, a vertical featured by performance or service requirements can be matched to a tailored CN slice flexibly and dynamically. Fig. 1.3 illustrates an example of CN slicing architecture with SDN and NFV.

1.1.2 Radio Access Network Slicing

Radio access network provides the data/signalling delivery services between the user equipment (UE) and the core network. Similar to CN slicing, RAN slicing is realized by virtually defining different RAN slices, each containing a tailored radio access technology (RAT) that is designed for a specific use case or a particular application. In the context of RAN slicing, network operators are decoupled from physical infrastructure providers. By aggregating multiple RATs in a common infrastructure, RAN slicing enables the sharing and dynamic provisioning of the physical resource among different customer groups [23] (as shown in Fig. 1.4). Under this premise, the 3rd generation partner project (3GPP) has identified an architecture named multi-operator core network (MOCN) [24,25], where a shared RAN is connected to each multi-operators' core network. In greater detail, the realization of RAN slicing includes efforts in both the media access control (MAC) layer and the physical (PHY) layer.

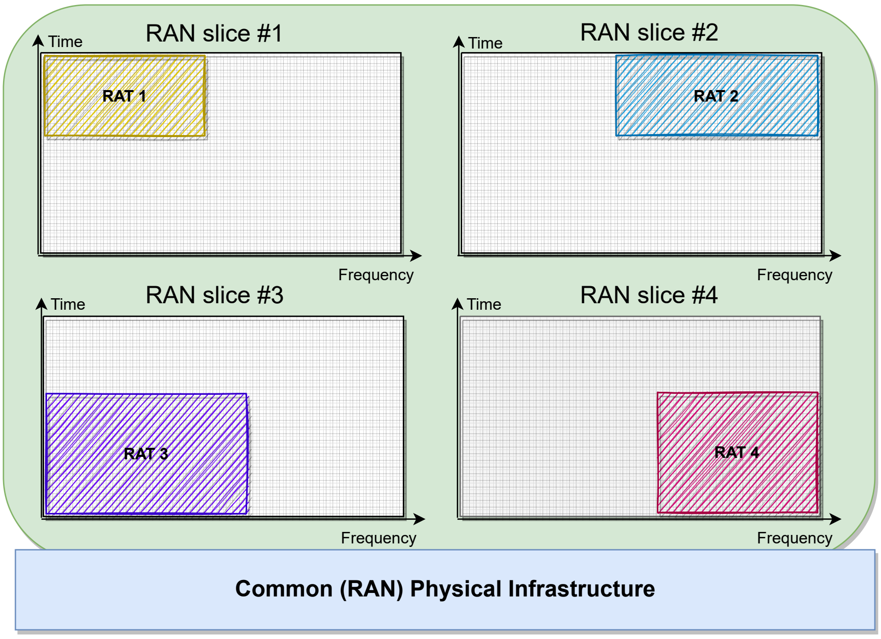

Figure 1.4: Radio access network slicing architecture.

From the MAC layer perspective, RAN slicing indicates the radio resource management among slices. For example, proper channel scheduling (or spectrum allocation) for all supported slices is needed to fulfil their QoS requirements (in terms data rate) [26]. Such a channel scheduling in RAN slicing has similar functionality as it in a legacy radio access network except that the scheduling objects change from users to slices. Apart from that, by means of packet scheduling, which decides the transmit sequence of the data packet, the latency requirement of both delay-tolerant and delay-sensitive services can be met. In addition, transmit power of slices is the key to managing both inner-cell and inter-cell interference, which requires carefully designed power control schemes.

1.1.3 Mixed-Numerology

From the PHY layer perspective, due to the extremely diverse requirements among services, the PHY configurations for different slices may be significantly different [4, 27]. These imparities could be in either baseband (BB), *e.g.*, frame structure and subcarrier spacing (SCS), and/or in radio frequency (RF) front-end, *e.g.*, processing bandwidth or sampling rate. For example, mMTC service might require a slice with small subcarrier spacing (and thus larger symbol duration) to support massive delay-tolerant devices and also enable its power-boosting gain in some extreme cases [28]. In contrast, vehicle-to-vehicle (V2V) communications have much more stringent latency and reliability requirements [2], which necessitates significantly smaller symbol duration compared with the mMTC scenario. For the high data rate eMBB communications, the subcarrier spacing and symbol duration cannot go to extreme values due to the channel doubly dispersion constraints. On the other hand, the limitation on cost, complexity and energy consumption of the communication devices may also affect the physical layer configurations. In particular, the RF bandwidth of the RF filter and digital to analog (D/A, or A/D) converter of a low-end MTC device could be significantly smaller than the full system bandwidth as compared to the standard UE or BS [29].

In the context of 3GPP standardization, a configuration set that includes some baseband parameters, such as SCS and cyclic prefix (CP), is denoted as a ‘numerology’ [28]. For example, 15 kHz SCS with normal CP and 60 kHz SCS with extended CP are classified as different numerologies. The wireless communication system that concurrently supports them is referred as a mixed-numerology (MN) system. However, in this thesis, the configuration set of ‘numerology’ is extended to include RF parameters such as sampling rate (or RF processing bandwidth). In the rest of this thesis, MN systems with diversified SCSs and sampling rates are denoted 'baseband-differed MN'(BB-differed MN) and 'radio frequency-differed MN'(RF-differed MN), respectively, to avoid confusion.

1.2 Motivation

The passing decades witnesses the rigid development of wireless communication systems. Each generation of mobile communications has brought significant changes to the world by applying a dominant technology: frequency division multiple access (FDMA) for the 1st generation (1G), time division multiple access (TDMA) for the 2nd generation (2G), code division multiple access (CDMA) for the 3rd generation (3G), and orthogonal frequency division multiple access (OFDMA) for the 4th generation (4G). The next generation wireless network is supposed to facilitate a fully mobile and connected community. Considering the high cost and deployment complexity, it is unfeasible to have separate radio designs for different services. By dividing the available resource into slices, NS is expected to provide each service/application with optimal individual design, making it the key enabler of 5G and beyond. Different services sharing the same physical infrastructure could significantly reduce the cost for constructing the network and simplify the resource allocation and interference management. Besides, new services can be directly added to the existing slicing network instead of deploying new ones.

A technical foundation of NS needs to be established for the coming decades that is likely beyond what we could imagine today. As the bedrock of wireless communication networks, the physical layer is indispensable for the future slicing mechanism. To support such a heterogeneous mixed-numerology (or multi-numerology) system with physical layer configuration imparity among slices on a common infrastructure, the transceiver architecture and widely used algorithms in the traditional single-service system may need to be significantly changed. One change of paramount importance is how to keep the low complexity and effective one-tap channel equalization and estimation. In a single-service orthogonal frequency division multiplexing (OFDM) system, it is known that such an equalizer is validated by the original circular convolution property of discrete Fourier transform (O-CCP-DFT), which diagonalizes the channel matrix and contributes to flat fading sub-channels [30]. Long-term evolution (LTE) is such a kind of system where all users share the same RF and BB configurations. However, the O-CCP-DFT in mixed-numerology systems may be invalidated because the mismatched sampling rate between transmitter and receiver could result in a misaligned discrete Fourier transform (DFT)/ inverse discrete Fourier transform (IDFT) processing pair.

Another key challenge associated with the mixed-numerology system is the signals multiplexing and isolation. In principle, slices can be multiplexed in any orthogonal access resources from either time or frequency domain, or be multiplexed with shared resources [31, 32]. Compared with the time division multiplexing (TDM), frequency division multiplexing (FDM) has several advantages such as better forward compatibility, ease of supporting services with different latency requirements, and energy saving by turning off the BS transceiver chain for some transmit time intervals (TTIs), etc [33]. In addition, FDM can support finer slices or scheduling granularity and thus achieve more flexible and spectrum-efficient RAN slicing. However, combining multiple slices with different physical layer configurations in FDM destroys the orthogonality between slices and results in inter-numerology-interference (INI) [34].

Considering the issues and challenges mentioned above, a framework model that takes the BB and RF differences into account is important for 5G and beyond multi-service systems in terms of parameter selection and frame structure design. In addition, with different physical layer configurations among slices, the widely used algorithms and signal processing procedures might be fundamentally affected, which promotes the necessity to verify the validity of current methods and calls for new ones.

1.3 Objectives

As previously mentioned, a clear understanding of mixed-numerology signals multiplexing and isolation in the physical layer is of importance to enable spectrum-efficient RAN slicing. To provide a solid foundation of network slicing mechanism, this thesis targets to systematically investigate the OFDM-based MN wireless communication systems in terms of system modeling and algorithm design (such as channel equalization/estimation and interference cancellation).

First and most important, a comprehensive mixed-numerology framework is missing in the literature. Therefore in this thesis, according to the BB and RF configurations imparities among numerologies, four scenarios are categorized and elaborated on the configuration relationships of different numerologies. Two-numerology system models considering the most generic scenario are established for both uplink and downlink transmissions. Besides, a low out of band emission (OoBE) waveform, *i.e.*, filtered-OFDM (F-OFDM), is implemented in the system for the sake of signal isolation and INI mitigation. Such a model includes all features of an MN system and can be directly converted to either a BB-differed model or an RF-differed model. As will be discussed in the literature review in Chapter 2, BB-differed MN systems have been thoroughly investigated from many aspects. Therefore, this thesis focuses on the RF-differed MN system. Under this premise, two theorems are proposed as the basis of algorithms design in the context of RF-differed mixed-numerologies, which generalize the original circular convolution property of DFT. A precoding algorithm is designed by utilizing the theorems to compensate the system degradation resulting from the signal distortion. In addition, INI cancellation algorithms are proposed based on a collaboration detection scheme, where joint numerologies signal models are implemented.

Another objective of this thesis is to verify the effectiveness of the existing channel estimation (CE) algorithms and to develop new ones in the presence of MN. Channel estimation is always one of the most important parts of receiver processing in wireless communication systems. Without an accurate channel estimation, all signal detection algorithms could be invalidated. Unfortunately, both signal distortion and INI caused by the configuration mismatch could result in the degraded performance of traditional CE methods. If the current channel estimation cannot be adapted accordingly, the performance of mixed-numerology systems would reach the bottleneck no matter how much effort is put into the other transmitter/receiver (Tx/Rx) algorithms. In this thesis, three CE methods, *i.e.*, least-square linear interpolation, least-square '*sinc*' interpolation, and minimum mean square error '*sinc*' interpolation are implemented and theoretically analyzed in the single-user and multi-user scenarios. The analysis reveals that the pilot-signal-to-noise-ratio (PNR), pilot distance, and position of pilot signals jointly affect the CE performance. The existence of interference-free subcarriers is demonstrated based on the derived closed-form expression of the INI. An interference-free pilot signal placement strategy is developed accordingly. Although the CE investigations are only carried on the uplink, the extension to downlink is straightforward.

The two problems associated with the RF-differed MN system, *i.e.*, signal distortion and INI, could negatively affect the power distribution of the received MN signals. System performance in terms of spectral efficiency may be seriously degraded. Consequently, it becomes outstandingly important to introduce an efficient subcarrier-level power allocation scheme in such kinds of systems to counter the performance degradation caused by the sampling rate mismatch. As such, this thesis attempts to extend the two-numerology model to contain 'M' different numerologies. Based on the model, closed-form expressions of desired signal, interference, and noise are derived. The distribution of signal-to-interference-plus-noise-ratio (SINR) is analyzed theoretically. An iterative convex approximation power allocation algorithm is proposed by applying the derived SINR. Results show that the power allocation algorithm contributes to remarkable spectral efficiency improvement.

In summary, the objectives of the thesis can be outlined as follows:

- Establish a comprehensive framework for MN systems considering both BB and RF configurations imparities and low OoBE waveforms;
- Examine the existing transceiver algorithms such as channel equalization and estimation, and develop new ones to mitigate the negative effects caused by the configuration mismatch among numerologies;
- Provide future trends and research directions as well as conclusions on the topic of mixed-numerology.

1.4 Research Contributions

The objectives mentioned above indicate that the thesis aims to build a complete paradigm of MN systems, based on which the system design in terms of parameter and waveform selection, and the frame structure and algorithms development can be carried out directly. The contribution of this thesis are summarized as follows to achieve these goals:

1. A comprehensive mixed-numerology framework is constructed based on practical 5G scenarios and use cases, and four scenarios are categorized by considering the configurations imparities in both BB and RF. The relationships among most of the key physical layer parameters, including subcarrier spacing, symbol duration, sampling rate, DFT size and waveforms, are derived for different scenarios. Based on the derivation, the generalized circular convolution properties of DFT are specified into two theorems by considering up-sampling and down-sampling, respectively. These theorems provide the theoretical foundation for the advanced interference analysis and cancellation algorithms in both uplink and downlink of the proposed system models.

2. Closed-form power pre-compensation algorithms are derived for overcoming the signal distortion for both uplink and downlink cases. In addition, based on the derived overall signal collaboration model, low complexity but

effective INI cancellation algorithms are proposed by either joint detection in the uplink or precoding in the downlink.

3. Two scenarios, *i.e.*, single-user (SU) scenario and multi-user (MU) scenario, are constructed to investigate the impact of the signal distortion and INI separately. Different combinations of estimation and interpolation methods, *i.e.*, least-square linear interpolation (denoted as LSLI), least-square '*sinc*' interpolation (denoted as LS-DFT), and minimum mean square error '*sinc*' interpolation (denoted as MMSE-DFT) are implemented in both scenarios with theoretical analyze. Pilot signal design principles (in terms of pre-compensation and pilot placement) are proposed and discussed based on the theoretical analysis. Numerical results are provided to verify the effectiveness of the derivations and proposed principles.

4. The two-numerology system model is extended to include 'M' numerologies, and a detailed digital domain signal processing chain is presented in the form of matrix notations. The power of the desired/interference signal and the noise is theoretically analyzed based on the system model, and the closed-form expression of SINR is derived. An iterative convex approximation power allocation algorithm is implemented to maximize the achievable system data rate. The performance of the algorithm is compared with other schemes.

1.5 Thesis Outline

The rest of this thesis is as follows. Chapter 2 starts with an overview of the current mobile networks. Then, the state-of-the-art (SOTA) techniques in related fields are discussed. After that, relevant technologies of mixed-numerology are provided.

Chapter 3 is produced on top of "Mixed-numerology Signals Transmission and Interference Cancellation for Radio Access Network Slicing " (the first journal publication in **List of Publications**) and focuses on the MN framework establishment. It starts with categorizing all MN scenarios considering both BB and RF configuration differences, followed by the relationships of all the corresponding system parameters. After that, the generalized circular convolution properties of DFT are specified into two theorems by considering up-sampling and down-sampling, respectively. Then, two-numerology systems modeling are presented for uplink and downlink, where a detailed digital domain signal processing chain is provided in matrix notations. Mathematical expressions of the channel and interference between the two numerologies are derived, based on which INI cancellation and power compensation algorithms are proposed. Finally, numerical results and conclusions are drawn.

Chapter 4 is produced on top of “Uplink Channel Estimation and Pilot Design for Radio-Frequency Differed Mixed-Numerology Systems” (the second journal publication in **List of Publications**). It presents the CE investigations in an RF-differed MN system. Two scenarios, *i.e.*, single-user scenario and multi-user scenario, are proposed in this chapter to investigate the negative effects of the signal distortion and the INI, respectively. It first constructs the system model for the single-user scenario. After that, CE performance analysis and pilot signal design based on this scenario are provided. Subsequently, the system modeling, CE performance analysis, and pilot design for multi-user scenario are provided. Numerical results and conclusions are given in the end.

Chapter 5 is produced on top of “Power Allocation in the Presence of Mixed-numerology” (the third journal publication in **List of Publications**), where the generalized RF-differed MN system model is constructed at first, followed by the mathematical derivations of the desired signal, interference, noise, and SINR. After that, the power allocation algorithm is introduced and verified by numerical results. Conclusions are drawn at the end of this chapter.

Finally, Chapter 6 concludes the thesis and discusses the future trends associated with the topic of mixed-numerology.

Chapter 2

Background and Literature Review

2.1 Overview of Multiple Access Techniques

Due to the scarcity of the spectrum, it is of extraordinary importance to utilize the spectrum resource efficiently. In general, modern wireless systems approach this goal via two paths [35]:

a) Applying multiple access (MA) techniques to increase the number of supported users in one BS;

b) Deploying cellular networks to increase the number of BSs within the unit area.

A cellular network is designed as a combination of many hexagonal cells that are geographically connected. Such networks provide the full coverage of the interested area and maximize the frequency resource utilization efficiency by reusing the same frequency band in nonadjacent cells. On the other hand, MA techniques enable different users to share frequency/time/space resources in the same cell without interfering each others. In general, MA techniques can be classified as orthogonal multiple access (OMA) techniques such as FDMA, TDMA, CDMA, and OFDMA, and non-orthogonal multiple access (NOMA) techniques such as power domain NOMA, code domain NOMA, and pattern division multiple access (PDMA) [36–39]. Considering the relevance to this thesis, only OMA techniques will be introduced in this section.

2.1.1 Frequency Division Multiple Access

Frequency division multiple access is realized by assigning each user with a specific subband in the frequency domain. Normally, a frequency domain duplexer is used to separate the uplink and the downlink. It is the oldest MA method [40] and was implemented in the 1st generation analog wireless networks such as advanced mobile phone system (AMPS) [41]. FDMA is conceptually simple to be implemented in terms of, *e.g.*, synchronization and equalization. However, it brings zero frequency diversity to the system because of the narrow and mutually independent subbands. In addition, FDMA requires a guardband between adjacent subbands to reduce interference among users, limiting the system capacity.

2.1.2 Time Division Multiple Access

In comparison, time division multiple access allows each user to transmit/receive over the whole system bandwidth but in different timeslots. It is a typical technique for the 2nd generation wireless networks and often combined with FDMA, *e.g.*, in the Global System for Mobile Communications (GSM) [40]. The large transmission bandwidth enables the TDMA users to fully exploit the frequency diversity, however, increases the complexity of the needed equalizer for inter-symbol-interference (ISI) mitigation. Besides, the discontinuous transmission in TDMA increases the difficulty of synchronization. Moreover, guard intervals are required between adjacent timeslots to allow, *e.g.*, transmitter ramp up, which constrains the capacity of the TDMA systems.

2.1.3 Code Division Multiple Access

Code division multiple access techniques were first developed for military purposes and then considered as the enabler of the 3rd generation wireless networks [35,42]. Different from the FDMA and TDMA, where either frequency or time resource is split to serve multiple users, CDMA distinguishes different users by their assigned spreading codes [43]. In general, a qualified spreading sequence (where spreading codes come from) should have good autocorrelation functions (ACFs) and a small crosscorrelation function to separate the signals in the receiver. Most frequently used spreading sequences include, *e.g.*, *m-sequence* [44], *Gold sequence* [45], and *Kasami sequence* [46]. Although CDMA systems are free from time and frequency resource limitations, the finite number of spreading codes determines that they cannot fulfil the modern society's ever-increasing capacity demand.

2.1.4 Space Division Multiple Access

Space division multiple access (SDMA) is a technique to distinguish different users through spatial segmentation. It was proposed to combat the co-channel interference (CCI) of the cellular systems by decoupling spatial signatures of the CCI and desired signal [47]. In mobile communications, SDMA is realized through the application of smart antenna/intelligent antenna [48, 49] to form different beams in different user directions. SDMA is perfectly compatible with other MA techniques, *e.g.*, CDMA [50], so that the system capacity can be further improved. Besides, it significantly eases the power control requirement in cellular networks.

Although with such obvious advantages, there were only superficial implementations of the SDMA due to the limited size of the antenna array. However, the exploitation of millimeter-wave (mmwave) in 5G makes it possible to compact large-scale antenna arrays in relatively small areas. This promotes the development of massive multiple-input-multiple-output (MIMO) techniques [51, 52] which takes full advantage of the SDMA.

2.1.5 Orthogonal Frequency Division Multiple Access

Orthogonal frequency division multiple access can be considered as an advanced FDMA technique. It was first proposed for wireless communications in [53] based on multicarrier FDMA. As been indicated by its name, OFDM is the key to realizing OFDMA by dividing the frequency resource into orthogonal subcarriers. These subcarriers are allowed to overlap with their neighbours without generating interference, which maximizes the spectral efficiency. Usually, OFDMA systems allocate a continuous group of subcarriers to each user for simple channel estimation/equalization and reduce the signalling overhead. In addition, by applying an adaptive scheduling method, *i.e*, assigning the most appropriate subcarriers to each user according to the channel state information (CSI), OFDMA achieves considerable multi-user diversity compared to the single-user OFDM [54]. Moreover, OFDMA can also be used in combination with other multiple access techniques: the resources are partitioned into time-frequency blocks in LTE for user assignment.

Due to the aforementioned superiority, OFDMA keeps its dominant position in 5G multiple access techniques. The investigated MN systems in this thesis are also based on OFDMA, and a detailed review of OFDM is provided in Section. 2.6.1.

2.2 Overview of Current Radio Access Networks

2.2.1 LTE and LTE-Advanced

It was just after the deployment of the first version wideband CDMA (WCDMA) technology, 3GPP has started working on the development of the next generation, *i.e.*, the Long Term Evolution or LTE [35]. LTE is an important milestone for mobile communication networks from 3G to 4G, where the evolution includes both the radio access network and core network. In particular, the evolved RAN adopts OFDMA as the multi access technique and provides limited support of MIMO (at most four antenna ports in the downlink). The first release of LTE specification (*Release 8*) prescribes a maximum 300 Mbits/s downlink data rate and 75 Mbits/s uplink data rate [55]. Note that the uplink transmission of LTE applies a DFT-single-carrier-OFDM (DFT-S-OFDM) modulation instead of OFDM for the sake of lowering signal peak-to-average-power-radio (PAPR) and relaxing the requirement on UE power amplifier (PA). In addition, a 5ms transmission latency in RAN is achieved considering no congestion problems. Although there were both time domain duplexing (TDD) and frequency domain duplexing (FDD) based LTE modes, they are pretty much the same except for the duplexing method. Therefore, LTE is the first unified mobile communication technique across the world.

The use of OFDMA in LTE significantly improves its spectral efficiency and flexibility for resource scheduling, which is inseparable from its unique PHY layer design. In the time domain, the basic time unit in LTE (based on FDD) is a 10ms radio frame, which is further divided into 10 subframes. Most LTE processing, such as scheduling, is based on the subframe. Each subframe consists of two slots, and each 0.5ms slot contains 6 or 7 CP-OFDM symbols depending on different application scenarios [56]. In the frequency domain, the LTE system bandwidth is divided into subcarriers (or subchannels), and a 15kHz SCS separates adjacent subcarriers. One subcarrier over an OFDM symbol duration is referred to as a resource element (RE) in the time-frequency domain, and 12 continuous subcarriers over a slot duration construct the basic resource scheduling unit, *i.e.* RB, in LTE systems.

Soon after the completion of *Release 8*, 3GPP launched new work items to enhance the LTE system performance and yielded *Release 10* for LTE-Advanced (LTE-A). To fulfill the spectral efficiency requirement specified by IMT-Advanced [57], LTE-A supports maximum 8 antenna pots in the downlink transmission and

4 in the uplink [58]. Together with a technique named carrier aggregation (CA), the theoretical peak data rate of LTE-A is improved to 1Gbits/s in the downlink and 500Mbits/s in the uplink. LTE-A was designed with backward compatibility of LTE and initiated the era of 4G. After that, many features were added to LTE-A to expend its functionality as well as to further improve the system performance, such as almost blank subframes (ABSs) [59], coordinated multi-point (CoMP) [60], and enhanced inter-cell interference coordination (eICIC) [61, 62]. However, the PHY layer configurations of LTE-A have not changed until the appearance of NB-IoT.

2.2.2 NB-IoT

Internet of things (IoT) describes the networks connecting physical objects with embedded sensors, radio frequency identification (RFID), or other technologies. It enables the data exchange among those physical objects and to other devices/systems [63, 64]. IoT aims to construct a highly distributed network by integrating everything in the world, which makes the world around us more intelligent and responsive. The main enabling of this promising paradigm includes identification and tracking technologies, wired and wireless sensor networks, enhanced communication protocols, etc. [65].

Thanks to the rapid development of these underlying technologies, IoT has been popular and developed with an irresistible momentum. It is estimated that there has been more than 10 billions IoT devices in the world by 2021, where around 10% of them are based on cellular networks [66]. In order to get access to the new market, mobile network operators together with communication equipment manufacturers promoted the standardization progress for cellular IoT techniques. A series of radio technology standards named NB-IoT were standardized by 3GPP in 2016 [56]. NB-IoT is designed to operate on the existing cellular networks, *e.g.*, Evolved Universal Mobile Telecommunications System Terrestrial Radio Access (E-UTRA) and GSM. There are several key performance indicators (KPIs) for NB-IoT, *e.g.*, improved coverage (up to 35km), support for a massive number of devices (50K/cell), ultra low cost (5 US dollars per device) and energy-efficient modules (10 years battery life) [67].

To utilize the spectrum resource efficiently and flexibly, NB-IoT devices could be assigned to three different operation modes as shown in Fig. 2.1. Stand-alone operation mode utilizes the spectrum currently allocated to GSM systems as well as some scattered spectrum for potential IoT deployment. In-band operation mode utilizes the resource block within LTE carriers. Guard-band operation mode utilizes the RBs in the LTE carriers' guard band [68]. The in-band and

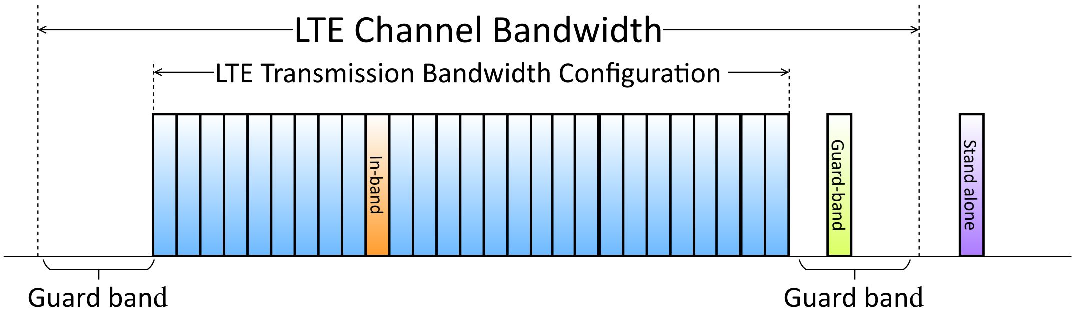

Figure 2.1: Operation modes of NB-IoT, where the blue blocks indicate LTE subcarriers, and the other colors indicate the subcarriers allocated to NB-IoT users in different operation modes.

guard-band operation modes enable the reuse of LTE base stations (BSs) by only updating their software. However, NB-IoT supports a 3.75 kHz SCS which is one-quarter of the normal LTE, and the low cost devices have a much lower sampling rate than LTE BS, the reuse of the LTE BS radio frequency and baseband processing chain may destroy the carrier orthogonality of the OFDM systems and cause narrowband interference (NBI) [69–72]. NB-IoT can be considered the first attempt for 3GPP to develop mixed-numerology systems. Since most NB-IoT devices are power limited, the interference in practical wireless systems may not be as serious as in theory. Nevertheless, situations change with more types of services included in 5G and beyond.

2.2.3 5G New Radio

A key difference between 5G new radio (NR) and LTE is that NR considers the support of various vertical services in addition to the traditional mobile broadband services at the beginning of design, as shown in Fig. 2.2. 5G oriented deployment scenarios include the following three types:

- Enhanced mobile broadband: the further enhancement of mobile broadband services provides users with a higher communication rate, more uniform and consistent user experience, and supports new services such as ultra-high-definition video (UHDV) [73] and immersive video [74].
- Ultra reliable low latency communication: vertical services such as vehicle-to-vehicle communications and industrial control put forward extremely high requirements for communication delay and reliability.
- Massive machine communication: massive IoT devices and diversified IoT services require the network to support the connection of massive devices and the frequent sending of myriad small data packets.

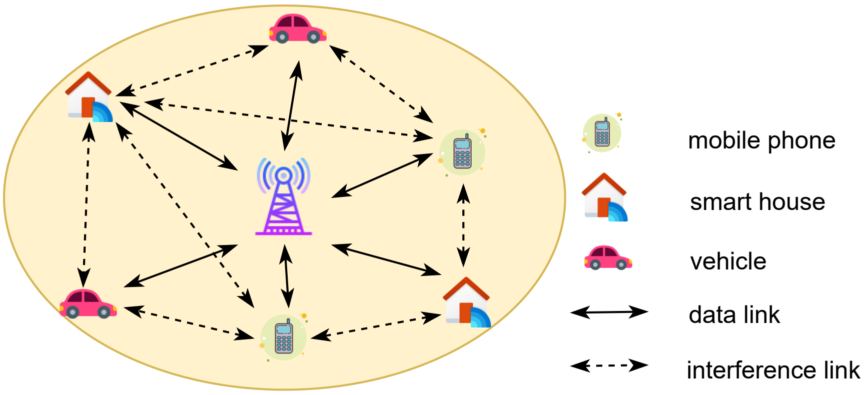

Figure 2.2: Typical operation scenario for a 5G wireless communication system.

Each service type has its characteristics and technical requirements. For example, eMBB services require sufficient system bandwidth and high spectral efficiency; mMTC services require the system to support multiplexing among a large number of machine-type devices; URLLC services need short TTI and fast hybrid automatic repeat request (HARQ) feedback to fulfill the latency requirements [75], and require highly reliable encoding/decoding and highly reliable transmission schemes to achieve the expected reliability [76]. The goal of NR is to use a unified air interface structure to meet all service requirements and to support the resource reuse of different services efficiently [77]. Although advanced transmission technologies such as MIMO and OFDM are used to increase spectral efficiency and data rate in LTE. It is still difficult to meet the differentiated performance requirements and KPIs of 5G diversified scenarios.

Millimeter-wave and Massive MIMO

With the rapid increase of mobile communication traffic, the spectrum deployed in 4G cannot meet the future market demand. Therefore, NR is designed to support the deployment within frequency range under 100GHz, including the traditional mobile communication band below 6GHz (denoted as sub-6G) and the high-frequency band up to millimeter-wave (denoted as above-6G) [78]. As mentioned in Section.2.1, a shorter wavelength of the millimeter-wave promotes the evolution of the large-scale antenna array, whose beamforming gain is able to compensate the severe path loss of the high-frequency communications and makes it possible to utilize the rich spectrum resources of the high-frequency band to satisfy eMBB services. As been standardized by 3GPP, the system bandwidth in millimeter-wave can be as large as 1GHz [79]. In addition, the extremely narrow beam provided by the large-scale antenna allows the implementation of the massive MIMO [52], which can multiply the spectral efficiency and the system capacity by fully exploiting the spatial diversity [51, 80].

Upgraded Wavforms

Different from the LTE, both downlink and uplink of NR support CP-OFDM waveforms. Due to the simple equalization and detection algorithm associated with CP-OFDM, it has more advantages than single carrier modulation, *e.g.*, DFT-S-OFDM. With the development of device technology, the uplink PAPR problem has been alleviated to a certain extent. On the other hand, the same modulation waveform for uplink and downlink is conducive to measuring and managing interference between uplink and downlink of TDD-based systems. Meanwhile, the NR uplink also supports the DFT-S-OFDM waveform in scenarios with limited uplink coverage.

Since the required ultra-high transmission rate in NR brings high computational complexity to the base station, implementing more advanced waveforms such as filter-bank multi-carrier (FBMC) [81], filtered OFDM [82], and windowed OFDM (W-OFDM) [83] is not mandatory according to the discussions in 3GPP. However, it is still an indispensable technique to realize the entire vision of 5G.

Flexible Frame Structure

The frame structure is the basis of air interface design. NR basically continues the LTE frame structure design concept, which is defined jointly in time and frequency dimensions. The NR frame structure has dignified flexibility in the time-frequency dimension to meet the needs of various scenarios, frequency bands and services.

The key parameters of NR frame structure based on CP-OFDM modulation include SCS and CP length. LTE supports a 15KHz subcarrier spacing, which is insufficient to meet the requirements specified for 5G. Thus, NR defines several SCS configurations in the frequency domain for different service types. For instance, URLLC services expect large SCS to shorten the data packet transmission time so that the latency requirements are satisfied, while for mMTC services, it is desired to use a smaller subcarrier interval to increase the time duration of data packet transmission and expand the coverage. From another perspective, a smaller SCS is required in sub-6G to avoid the excessive overhead of CP. At the same time, a larger subcarrier interval is preferred in above-6G to avoid serious inter subcarrier interference caused by Doppler frequency offset. In order to allow the multiplexing of different subcarrier intervals in one OFDM symbol, each SCS is designed to be a multiple, more specifically an integer power of 2 [28], of the others. Accordingly, the length of CP is scaled with the subcarrier spacing to achieve boundary alignment between OFDM symbols with different SCS.

2.3 Overview of Advanced Waveforms

As previously mentioned, a key challenge for designing mixed-numerology systems is to minimize the performance degradation caused by INI. In comparison with adding a guard band (GB) between slices, which reduces the spectrum utilization efficiency, a more practical and attractive way is to design new waveforms with lower out of band emissions [84]. A variety of advanced waveforms have been proposed for the next generation networks, among which subcarrier filtered multicarrier system, subband filtered multicarrier system are the two most widely used classes. The former includes FBMC [81], block-filtered OFDM (BF-OFDM) [85], and generalized frequency division multiplexing (GFDM) [86], while the latter includes universal filtered multi-carrier (UFMC) [87], F-OFDM [82] and W-OFDM [83]. A power spectral density (PSD) comparison of the aforementioned waveforms is illustrated in Fig. 2.3. It can be observed that advanced waveforms contribute to much lower OoBE compared to OFDM.

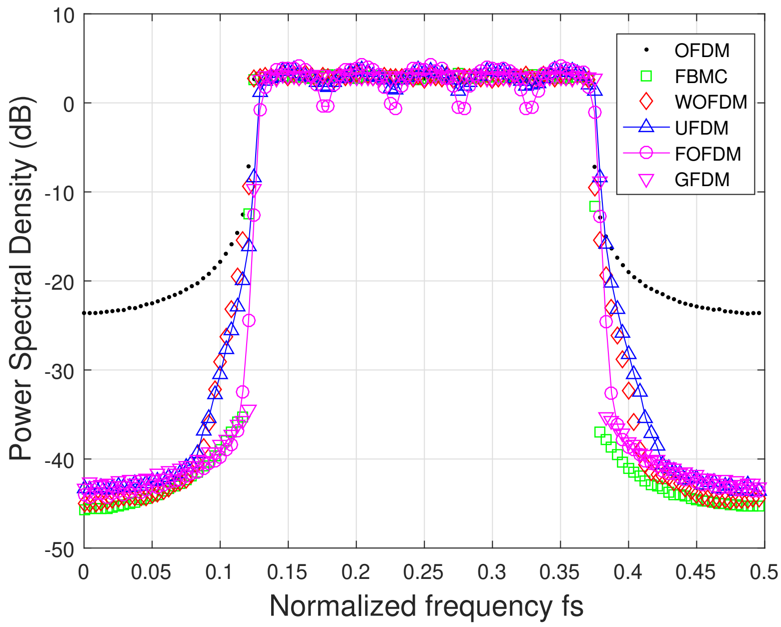

Figure 2.3: Power spectral density comparison of the candidate 5G waveforms.

These waveforms have their advantages and drawbacks, *e.g.*, FBMC applies subcarrier level pulse shaping to achieve the trade-off between time and frequency domain localization. This technique provides the best OoBE among the above waveforms. However, due to the interference between its real and imaginary branches, the channel estimation/equalization needs significantly higher computational complexity than OFDM. In addition, it is very hard to combine FBMC with MIMO systems [88]. Similar to FBMC, GFDM also utilizes subcarrier level pulse shaping but in a block-based manner so that inter-burst tails are avoided [89]. Nevertheless, block-based processing increases the decoding latency of the GFDM system. Hence it may not be an appropriate choice for low latency services. Moreover, FBMC and GFDM both require different transceiver structures from traditional OFDM systems, which further reduces the competitiveness of these two waveforms. Compared with FBMC and GFDM, F-OFDM and W-OFDM have drawn much more attention from both academia and industry because they keep the core structure of the traditional OFDM receiver. The filtering/windowing procedure between transmitter and receiver can be transparent to each other, which is aligned with the 3GPP recommendations about 5G waveform candidates [90, 91].

2.3.1 Windowed-OFDM

W-OFDM utilizes windowing, e.g., raised cosine window suggested by [92], to smooth the transmission between adjacent symbols and reduces the OoBE generated from the discontinuous transitions. As shown in Fig. 2.4, compared to the CP-OFDM, there is a roll-off portion in each side of the W-OFDM symbol, and the roll-off portions of neighbour symbols are overlapped in between. Although W-OFDM cannot reduce the OoBE as much as F-OFDM, it has negligible PAPR overhead compared with the filtering-type techniques [93]. In addition, W-OFDM provides high robustness against timing and carrier frequency offset in the asynchronous systems [94]. Due to the aforementioned advantages, W-OFDM has become one of the most discussed candidate waveforms for 5G.

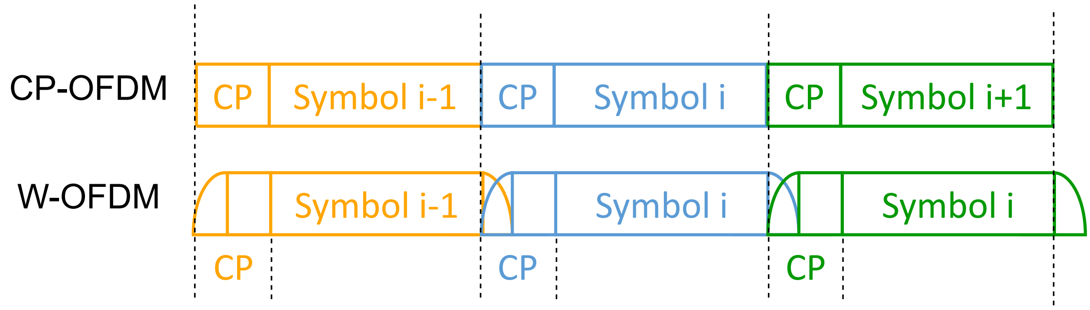

Figure 2.4: Comparison between CP-OFDM symbols and W-OFDM symbols, where the roll-off portion of adjacent W-OFDM symbols overlaps with each other.

Great efforts have been made to improve the performance of the W-OFDM system. For instance, a joint windowing scheme is proposed in [92] to eliminate adjacent channel interference (ACI) and reduce OoBE. In [95], a time-asymmetric windowing scheme is proposed to eliminate the ISI that is introduced due to the insufficient CP length.

2.3.2 Filtered-OFDM

F-OFDM implements subband filtering to suppress the spectrum leakage. Specifically, a band-pass filter, e.g., windowed sinc filter, is applied in each slice's assigned subband (or bandwidth part according to the 3GPP definition) to confine the generated OoBE. Although the filtering process causes signal power spreading to its neighbours and results in ISI (as shown in Fig. 2.5), a well designed filter could help reducing the ISI to a negligible level compared to INI. With proper subband filters, the strict synchronization requirement in conventional OFDM systems could be relaxed [82, 96], and the reserved guard band is minimized [97]. In addition, F-OFDM shows a good frequency localization property, especially in high modulation order, while offering a reduced sensitivity to subband separation [98]. In this thesis, F-OFDM is considered (except for Chapter. 4) to achieve better signal isolation due to its excellent trade-off between performance and complexity [97], as well as the flexibility it can provide for the subband configurations [99]. However, the results can be extended by using other waveforms.

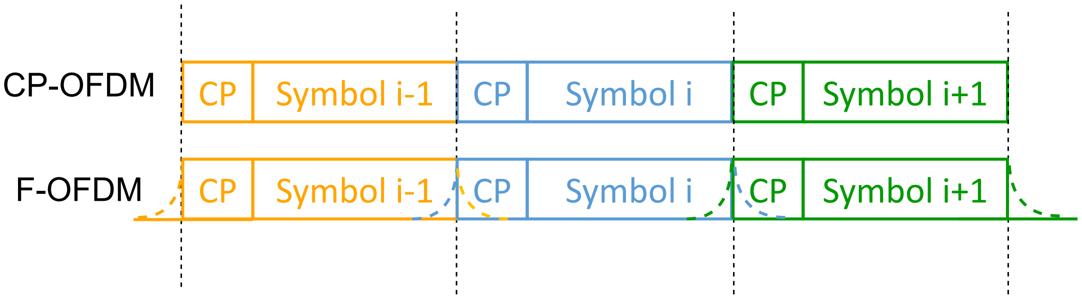

Figure 2.5: Comparison between CP-OFDM symbols and F-OFDM symbols, where well designed filters could help reducing the ISI between adjacent F-OFDM symbols to a negligible level.

2.4 Overview of Channel Estimation Methods

Time variance and frequency selectivity are important features of wireless communication channels, which necessitates the channel estimation so that the signal can be recovered in the receiver. The most commonly used channel estimation technique in OFDM systems is the pilot based channel estimation, where prior known pilot signals are mixed with the transmit data signals in the Tx and extracted in the Rx to estimate the channel information in pilot locations. In general, the pilot aided channel estimations are either LS based or MMSE based. The MMSE based estimations is able to achieve optimal MSE by using the knowledge of channel statistics (which is practically unavailable), but have very high computational complex due to the need of matrix inversion operation. [100] and [101] propose relaxed MMSE estimations by replacing the channel correlation matrix by either a power normalization identity matrix or a diagonal matrix with exponential delaying elements. In comparison, the LS based estimations are computational less complex and do not require the knowledge of channel statistics. However, it cannot provide acceptable MSE performance compared to the MMSE based ones especially in noise/interference-limited cases. To improve the performance of LS estimation, a variety of denoising strategies have been developed [102–104], where a threshold is used to prune the channel impose response coefficients and helps to distinguish the channel taps from the noise taps. Such a threshold can be devised in time domain or any other transform domain such as frequency domain and wavelet domain.

On the other hand, an interpolation method is needed so that the channel response in non-pilot locations can be achieved. A typical approach is to apply linear interpolation to obtain the channel impulse/frequency response between adjacent pilot signals, but will introduce non-negligible interpolation error. The author of [105] proposed a DFT-based channel estimation, where an additional DFT processing is introduced to obtain the frequency response of a LS estimated channel. The DFT-based method improves the channel estimation performance by suppressing time domain noise, however, may lead to MSE floor due to incorrect channel information such as channel delay spread. Hence, Y. Kang et al. proposed a modified DFT channel estimation, which is able to improve the performance by deciding significant channel taps adaptively without requiring any channel statistical information [106]. Recently, a deep learning based channel estimation method is proposed in [107], where the time–frequency response of a fast fading channel is represented as a 2D image, and the unknown channel response are achieved by learning the channel information at the pilot locations.

2.5 State-of-the-Art in Mixed-Numerology Systems

Despite the fact that the first 5G technology was commercialized in 2019, it is in a primary state, and the details of aforementioned techniques are still under intensive study. Tremendous effort is necessary for completing the entire vision of 5G and beyond networks. In this section, a literature review covering state-of-the-art investigations on different types of mixed-numerology systems is presented.

2.5.1 Baseband-Differed Mixed-Numerology

In the literature, researches about BB-differed mixed-numerology mainly focus on three aspects, *i.e.*, INI cancellation, PAPR reduction, and resource allocation. In [34], for example, authors build a framework for the BB-differed MN system to support multiple types of slices where each has individual optimized subcarrier spacing, and an interference cancellation algorithm was presented for downlink transmission. The authors in [108] perform a thorough investigation of INI with CP-OFDM waveform, where critical factors that affect the power of the interference are analyzed, and INI mitigation techniques are discussed. The authors of [109] proposed a multi-rate (MR) signal processing method for the BB-differed MN system, which can greatly reduce the computational complexity. However, inter-subband-interference (ISubBI) might be introduced and degrade the system performance. In addition, INI analysis and mitigation solutions with different system assumptions are provided in the literature, *e.g.*, [110], [111], [112], and [83] assume F-OFDM, flexible configured OFDM (FC-OFDM), FBMC, and W-OFDM waveforms, respectively, while the investigations in [113] and [114] consider uplink and downlink massive MIMO, respectively.

On the other hand, a novel *common CP* insertion method is proposed in [115] to restructure the INI pattern into an ordered manner. Considering such a *common CP*, a spectrum-efficient approach of guard band implementation technique is proposed in [116]. By exploiting the inherent characteristics of the INI distribution among subcarriers of the adjacent numerologies, the proposed guardband allocation method reduces up to 50% of the wasted spectrum. Different from the previous works, [117] presents an INI recognition approach for the NR downlink transmission based on the convolutional neural network (CNN).

The high PAPR associated with CP-OFDM is a non-negligible problem for NR uplink services, and the co-existing of multiple numerologies further complicates this problem. The authors in [118] present an analysis of the PAPR probability distribution function in the presence of mixed-numerologies, where system parameters including numerology, bandwidth and power level of each subband are considered together with the level-crossing theory [119]. In [120], a signal distortion technique termed as noise-shaped iterative clipping and filtering (NS-ICF) is developed to reduce the PAPR in MN systems while maintaining an acceptable INI level. Huang et al., in [121] propose a circularly pulse-shaped OFDM (CPS-OFDM) waveform with the consideration of user-specific precoder flexibility. The carefully designed prototype shaping vector in CPS-OFDM lowers both its out-of-subband-emission (OSBE) and PAPR. In the meanwhile, CPS-OFDM can be realized with linearithmic-order complexity via the characteristic-matrix-domain implementation method. Other PAPR reduction mechanisms such as fast-convolution (FC) based processing and numerology selection/scheduling are presented in [122] and [123], respectively.

In terms of the resource allocation schemes in MN systems, Demir et al. in [124] develop an approach to adaptively adjust the guards in both time and frequency domain by considering a cross-layer (PHY and MAC) scheduling technique, which shows a decent performance to improve the spectral efficiency in MN systems. In [125], INI-aware scheduling methods are proposed for the purpose of enhancing the reliability in the multi-numerology systems, by which no additional spectral usage, computational complexity, and latency will be caused. A joint power and resource block allocation method is proposed in [126] to minimize the total transmit power while considering imperfect channel state information. Similarly, the authors in [127] propose a combined subcarrier and power allocation scheme to maximize the spectral efficiency. However, the investigated system is based on NOMA and towards the 6-th generation (6G) wireless networks.

2.5.2 Radio Frequency-Differed Mixed-Numerology

As for the RF configuration imparity, in-band and guard-band NB-IoT is a special and practical case for the mixed-numerology study, and it has been adopted as a feature of the LTE-Advanced [68]. Low cost NB-IoT devices operating at a much lower sampling rate (*e.g.*, 240 kHz) are multiplexed with the normal LTE UEs (with sampling rate 30.72 MHz) on the same infrastructure. The authors in [128] present the interference analysis and a channel equalization algorithm for the uplink NB-IoT, while in [129] the uplink coexistence of NB-IoT and LTE is investigated from a physical layer perspective. As for 5G, the simultaneously operating of mMTC and eMBB services constructs a typical RF-differed MN scenario. The former accommodates the intensively distributed services and is likely to have much lower RF processing bandwidth than the latter to maintain low cost and power consumption. Since the standardization of mMTC is deprioritized to the second echelon in 3GPP, the researches on this scenario are not as popular as that for the eMBB and URLLC. However, as one of the most important service types, it can be imagined that the coexistence of mMTC and eMBB will be a common case in future networks. Therefore, it becomes particularly important to clearly understand the potential problem that may come up with this situation. However, a general and comprehensive study on this direction is still missing in the literature. The CE estimation investigations of MN systems are in the initial stage. Related work such as [130] is based on the DBSR scenario, and fundamental analysis for the channel estimation is not included. There is no clue why and how the performance degradation may happen, not to mention the design of new algorithms. Regard to the power allocation scheme in MN systems, the only research is carried out by Mao et al. in [110]. However, this work is based on BB-differed-MN. As such, an efficient power allocation scheme for RF-differed-MN is still missing in the literature.

2.6 Relevant Techniques

The previous section provides a brief overview of different mixed-numerology systems. Meanwhile, a clear and precise understanding of related background techniques is vital for revealing the insights of this thesis. Therefore, in the following subsections, reviews of several background techniques are presented to explain, for example, what is the original circular convolution property of discrete Fourier transform, and how up-sampling/down-sampling happens in the investigated MN systems.

2.6.1 Realization of OFDM

As previously mentioned, OFDM is a multi-carrier technique where subcarriers overlap with their neighbours in an orthogonal manner. Fig. 2.6 illustrates the comparison between the FDM and OFDM in terms of the subcarriers division. It is obvious that OFDM exploits the spectrum much more efficiently than FDM.

OFDM was proposed in 1966 at Bell Labs, and a DFT-based method was proposed in 1971 to implement the OFDM cost-efficiently [131]. However, its applications were not deployed in the industry until the fast Fourier transform (FFT) was proposed in 1980 [132]. In 1985, Leonard J. Cimini of Bell Labs

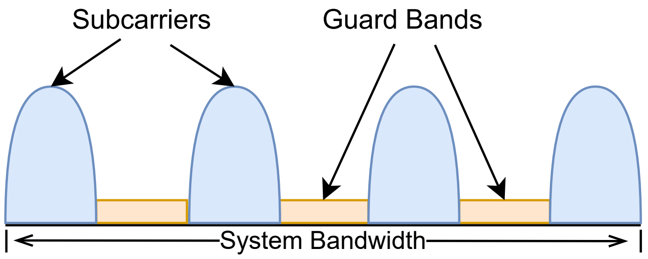

(a) FDM subcarriers division

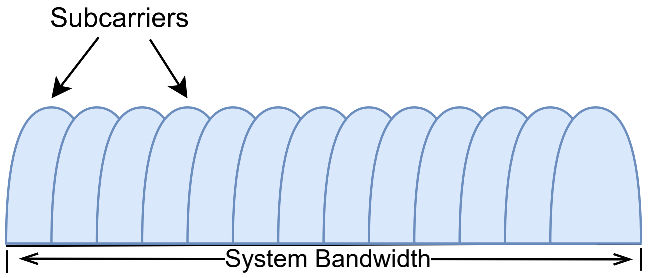

(b) OFDM subcarriers division

Figure 2.6: Spectrum divisions of FDM and OFDM.

proposed the first OFDM-based cellular communication system [133]. After that, with the accelerating developments of hardware and digital signal processing (DSP) techniques, the realization of OFDM becomes affordable even for mobile devices, which makes it chosen as the enabler of LTE.

OFDM modulation and demodulation

In theory, the realization of OFDM starts with the serial-to-parallel (S/P) conversion of the input data stream, which multiplies the symbol duration of the signal and makes it considerably more robust to the multi-path effect of the wireless channels. Then, the parallel data streams are modulated to complex symbols, *i.e.*, based on, for example, phase shift keying (PSK) or quadrature amplitude modulation (QAM), and fed into an IDFT (or IFFT) processor. Assuming the k-th complex data symbol is denoted by d_k $(0 \leq k \leq N-1)$, where N is the number of subcarriers. The n-th output of the IDFT can be written as:

$$x_n = \frac{1}{\sqrt{N}} \sum_{k=0}^{N-1} d_k e^{\frac{j2\pi}{N}kn}, \quad 0 \leq n \leq N-1. \tag{2.1}$$

An OFDM symbol $\mathbf{s} = [x_0, x_1, \cdots, x_{N-1}]$ is then generated by passing the output of the IDFT through a parallel-to-serial (P/S) converter. Normally, a cyclic prefix, which is the duplication of the last L values of $\mathbf{s}$, is appended to the front of the OFDM symbol, as shown in Fig. 2.7 , so that the final OFDM

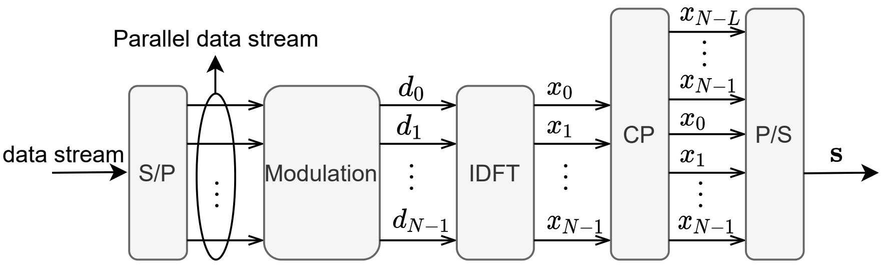
Parallel data stream
data stream
S/P
Modulation
d_0
d_1
d_{N-1}
IDFT
x_0
x_1
x_{N-1}
CP
x_{N-L}
x_{N-1}
x_0
x_1
x_{N-1}
P/S
$\mathbf{s}$

Figure 2.7: A simplified process to generate OFDM symbols in the transmitter.

symbol is written as $\mathbf{s} = [x_{N-L}, \cdots, x_{N-1}, x_0, x_1, \cdots, x_{N-1}]$. As long as L is no less than the maximum channel delay spread, the extended OFDM signal would be free of ISI and inter-channel-interference (ICI). Similarly, an inverse process is carried out in the receiver to recover the data. As shown in Fig. 2.8, $\mathbf{r} = [y_{N-L}, \cdots, y_{N-1}, y_0, y_1, \cdots, y_{N-1}]$ refers to the received symbol vector. After S/P and CP removing, the received signal passes through a DFT processor, where the k-th output is obtained as:

$$d'_k = \frac{1}{\sqrt{N}} \sum_{n=0}^{N-1} y_n e^{\frac{-j2\pi}{N}kn}, \quad 0 \leq k \leq N-1. \tag{2.2}$$

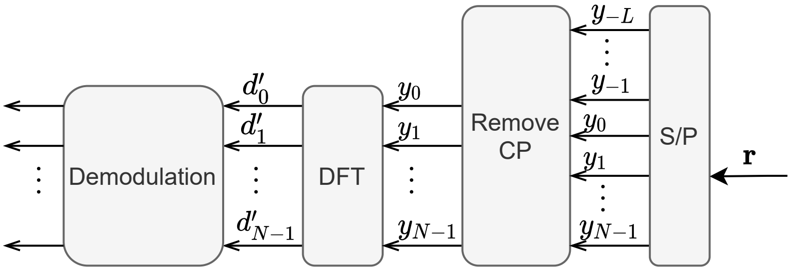
Demodulation
d'_0
d'_1
d'_{N-1}
DFT
y_0
y_1
y_{N-1}
Remove CP
y_{-L}
y_{-1}
y_0
y_1
y_{N-1}
S/P
$\mathbf{r}$

Figure 2.8: OFDM signal demodulation in the receiver.

If $\mathbf{h} = [h_0, h_1, \cdots, h_{L_c-1}]$ is denoted as the channel impulse response vector with L_c being the channel length, and $\mathcal{H}$ is the Toeplitz matrix with $[\mathbf{h}, \mathbf{0}_{1\times(N+L-L_c)}]^T$ and $[h_0, \mathbf{0}_{1\times(N+L-1)}]$ being its first column and first row, respectively. The entire OFDM modulation and demodulation can be expressed in the following matrix notations:

$$\mathbf{d}' = \mathbf{F}^H \mathbf{R} \mathcal{H} \mathbf{C} \mathbf{F} \mathbf{d}, \tag{2.3}$$

where $\mathbf{d} = [d_0, d_1, \cdots, d_{N-1}]^T$ and $\mathbf{d}' = [d'_0, d'_1, \cdots, d'_{N-1}]^T$; $\mathbf{C} = [\mathbf{0}_{L\times(N-L)}, \mathbf{I}_L; \mathbf{I}_N]$ and $\mathbf{R} = [\mathbf{0}_{N\times L}, \mathbf{I}_N]$ are CP insertion and removal matrices, respectively; $\mathbf{F}^H$ and $\mathbf{F}$ are N points DFT and IDFT matrices, respectively. The entries of $\mathbf{F}^H$ and $\mathbf{F}$

are:

$$\mathbf{F}(n,k) = \frac{1}{\sqrt{N}} e^{\frac{-j2\pi(n-1)(k-1)}{N}}, \tag{2.4}$$

and

$$\mathbf{F}^H(n,k) = \frac{1}{\sqrt{N}} e^{\frac{j2\pi(n-1)(k-1)}{N}}, \tag{2.5}$$

for the n-th row and k-th column, where $1 \leq n, k \leq N$.

O-CCP-DFT

Benefiting from the CP insertion and removal processing, the Toeplitz matrix $\mathcal{H}$ is transformed to a circulant matrix (assume $L \geq L_c$), as shown in Eq. (2.6). As such, the linear convolution between the transmit signals and the channel impulse responses is converted to a circular convolution. Based on the **Theorem 4.8.2** in [30], the paired DFT processing of a circulant matrix $\mathcal{H}$ produces a diagonal matrix, *i.e.*, $\mathbf{F}^H \mathcal{H} \mathbf{F} = diag(\lambda_1, \cdots, \lambda_N)$ where $(\lambda_1, \cdots, \lambda_N)$ are the DFT of $\mathcal{H}$'s first column. Therefore, the channel matrix is diagonalized, which significantly reduces the receiver complexity for channel equalization. This property is named the **Original-CCP-DFT** to distinguish with the ones proposed in this thesis.

$$\mathbf{R}\mathcal{H}\mathbf{C} = \begin{pmatrix}
h_0 & 0 & 0 & & \vdots & h_2 & h_1 \\
h_1 & h_0 & 0 & & h_{L_c-1} & \vdots & h_2 \\
h_2 & h_1 & h_0 & & 0 & h_{L_c-1} & \vdots \\
\vdots & \vdots & \vdots & & 0 & 0 & h_{L_c-1} \\
h_{L_c-1} & h_{L_c-2} & h_{L_c-3} & & 0 & 0 & 0 \\
0 & h_{L_c-1} & h_{L_c-2} & \cdots\ \cdots & 0 & 0 & 0 \\
0 & 0 & h_{L_c-1} & & 0 & 0 & 0 \\
\vdots & \vdots & \vdots & & \vdots & \vdots & \vdots \\
0 & 0 & 0 & & h_0 & 0 & 0 \\
0 & 0 & 0 & & h_1 & h_0 & 0 \\
0 & 0 & 0 & & h_2 & h_1 & h_0
\end{pmatrix}. \tag{2.6}$$

2.6.2 Sampling

Digital signal processing is one of the cornerstone of modern communication systems. It provides the wireless communication system with stronger anti-noise and anti-interference properties, and enables the flexible application of various signal processing algorithms [134]. Considering analog signal is a type of time-continuous real-world signals, digital signal refers to the discrete signal obtained by sampling, quantizing and encoding the analog signal. Digital-to-analog converter (DAC) and analog-to-digital converter (ADC) are two essential components to realize signal conversions between analog and digital. In general, sampling is performed by the ADC in the Rx to discretize the continuous signal in the time domain. As shown in Fig. 2.9(a), the time-continuous signal $\mathbf{r}(t)$ with $t \in (0, T)$ is converted to the discrete signal $\mathbf{r}[n]$ after the sampling in ADC. Considering f_s as the sampling rate and $\Delta T = \frac{1}{f_s}$ as the sample duration, $\mathbf{r}[n]$ can be written as $\mathbf{r}[n] = \mathbf{r}(n\Delta T)$ with the integer $n \in [0, \lfloor T f_s \rfloor]$. Assigning $T = T_c$, *i.e.*, one OFDM symbol period, confines n to be an integer within $[0, N-1]$. On the contrary, DAC reconstructs the continuous signal from the digital signal in the Tx with $\dot{f}_s$ as the reference frequency, as shown in Fig. 2.10(a). Ideally, the signal can be perfectly reconstructed as long as the Nyquist sampling theorem is satisfied. However, considering the hardware complexity, many DACs in real world perform *zero-order hold* interpolation function [135] to construct the continuous signal. As such, the constructed continuous signal $\bar{\mathbf{s}}(t)$ holds a constant amplitude during each sample period, as shown in Fig. 2.10(b).

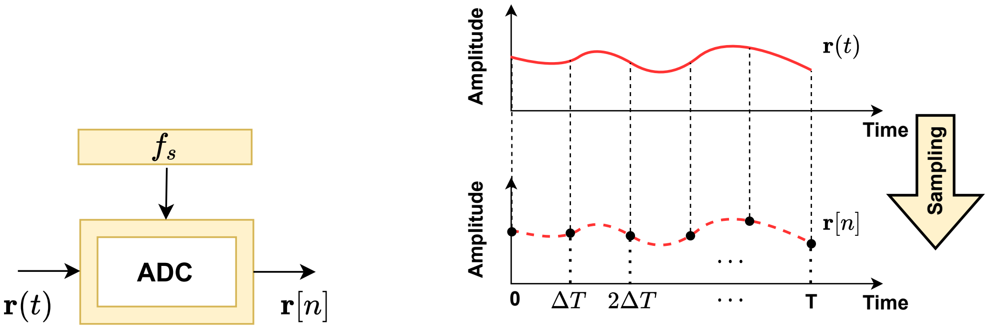

(a) ADC

(b) Sampling

Figure 2.9: A simplified process for signal converts from analog to digital with f_s being the sampling rate.

Recalling the OFDM signal achieved in Eq. (2.1), $\bar{\mathbf{s}}(t)$ during one OFDM symbol period is than expressed as:

$$\bar{\mathbf{s}}(t) = \mathbf{s}[\lfloor \frac{t}{\Delta\dot{T}} \rfloor] = \frac{1}{\sqrt{N}} \sum_{k=0}^{N-1} d_k e^{\frac{j2\pi}{N}k\lfloor\frac{t}{\Delta\dot{T}}\rfloor}, \quad 0 \le t \le T_c, \tag{2.7}$$

where $\Delta\dot{T} = 1/\dot{f}_s$. To focus on the sampling process, the propagation channel is ignored for now, *i.e.*, $\mathbf{r}(t) = \bar{\mathbf{s}}(t)$. Considering the transmitter DAC and receiver ADC holds the same sampling rate, *i.e.*, $f_s = \dot{f}_s$ and $\Delta T = \Delta\dot{T}$, the discrete signal generated in the Tx can be perfectly recovered as $\mathbf{r}[n] = \bar{\mathbf{s}}(n\Delta T) = \mathbf{s}[n]$ even the system is not well synchronized, as shown in Fig. 2.11.

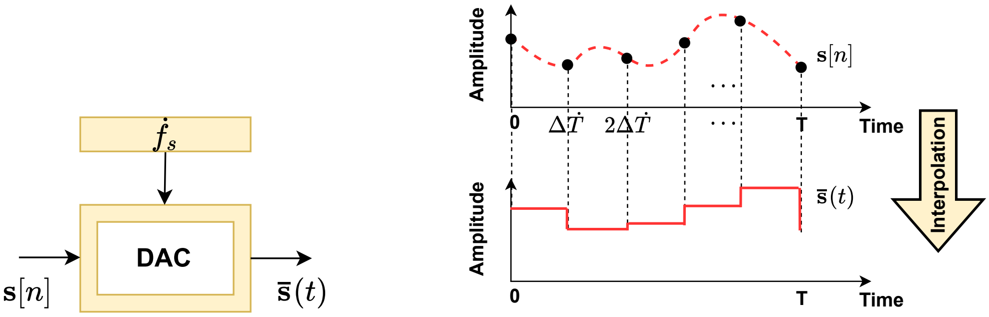
$\dot{f}_s$
DAC
$\mathbf{s}[n]$
$\bar{\mathbf{s}}(t)$
Amplitude
0
$\Delta\dot{T}$
$2\Delta\dot{T}$
$\cdots$
T
Time
$\mathbf{s}[n]$
Interpolation
Amplitude
$\bar{\mathbf{s}}(t)$
0
T
Time

(a) DAC (b) Interpolation

Figure 2.10: A *zero-order hold* process for signal converts from digital to analog with $\dot{f}_s$ being the sampling rate.

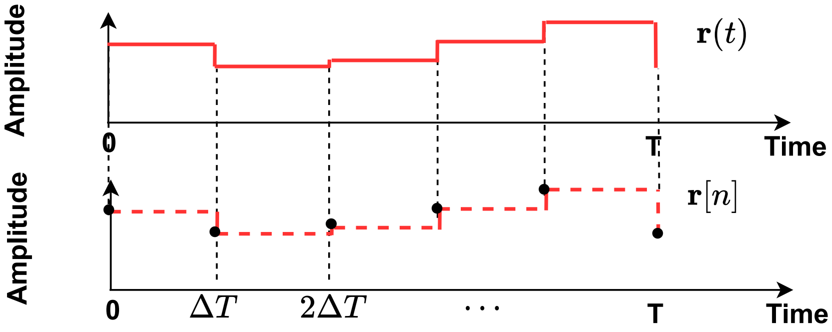
Amplitude
$\mathbf{r}(t)$
0
T
Time
Amplitude
$\mathbf{r}[n]$
0
ΔT
$2\Delta T$
$\cdots$
T
Time

Figure 2.11: The recover of $\mathbf{s}[n]$ via normal sampling process.

Up-sampling

Up-sampling is an interpolation process, and it is always implemented to reduce the complexity of filters or to decrease the noise. Normally, up-sampling is realized by inserting zeros between adjacent samples, and passing the expanded signal through a low-pass filter to create "in-between" samples (and to eliminate the image signal) [136, 137]. As shown in Fig. 2.12, the up-sampled signal can be written as $\mathbf{r}[m] = \mathbf{r}(m\Delta T')$, where m is an integer within $[0, \lfloor Q_u T f_s \rfloor]$. $\Delta T' = \Delta T / Q_u$ refers to the updated sample duration and Q_u is the up-sampling rate. Again, assigning $T = T_c$ confines the range of m to be $[0, Q_u N - 1]$.

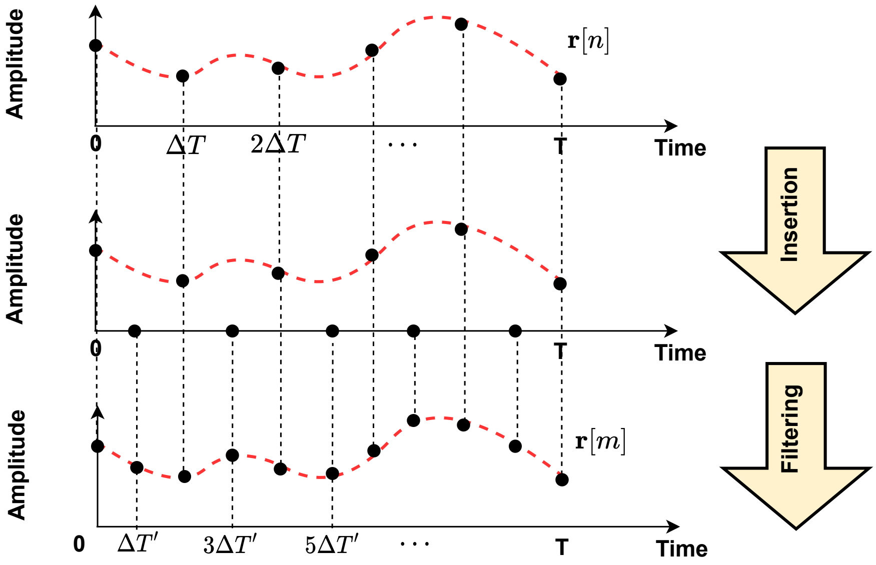

Figure 2.12: Normal up-sampling process with $Q_u = 2$.

However, in the presence of mixed-numerologies (more specifically RF-differed MN), the up-sampling may occur unpredictably because of the sampling rate difference between the transmitter and the receiver. It is likely that there is no matched low-pass filter in such kind of unintentional up-sampling. In addition, considering the DAC in the transmitter is based on *zero-order hold* interpolation, the up-sampling of $\mathbf{r}(t)$ results in $\mathbf{r}[m] = \bar{\mathbf{s}}(m\Delta T') = \bar{\mathbf{s}}[\lfloor m/Q_u \rfloor]$. For m changing from 0 to $Q_u N$, $\bar{\mathbf{s}}[\lfloor m/Q_u \rfloor]$ is expended as:

$$\bar{\mathbf{s}}[\lfloor m/Q_u \rfloor] = [\underbrace{\mathbf{s}[0], \cdots, \mathbf{s}[0]}_{Q_u}, \cdots, \underbrace{\mathbf{s}[N], \cdots, \mathbf{s}[N]}_{Q_u}], \tag{2.8}$$

which contains a multiple of same samples within each Q_u steps. A simplified procedure of such an unintentional up-sampling is illustrated in Fig. 2.13. Therefore, the up-sampling in this thesis is equivalent to multiply the signal

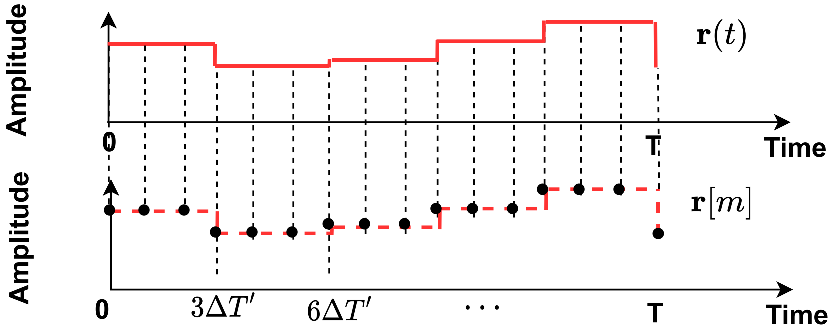

Figure 2.13: Unintentional up-sampling of $\mathbf{r}(t)$. The sample duration before and after up-sampling is ΔT and $\Delta T'$, respectively, and the up-sampling rate is $Q_u = 3$.

by the following up-sampling matrix $\mathbf{U}$:

$$\mathbf{U} = \begin{pmatrix} \mathbf{1}_u & \mathbf{0} & \cdots & \mathbf{0} \\ \mathbf{0} & \mathbf{1}_u & \cdots & \mathbf{0} \\ \vdots & \vdots & \ddots & \vdots \\ \mathbf{0} & \mathbf{0} & \cdots & \mathbf{1}_u \end{pmatrix}, \tag{2.9}$$

where $\mathbf{1}_u = [1, 1, \cdots, 1]^T_{1\times Q_u}$ and $\mathbf{0}$ refers to a zero vector with the same size as $\mathbf{1}_u$.

Down-sampling

The process to decimate a sample sequence by an integer factor Q_d, *i.e.*, keep only every Q_d-th sample, is referred as the down-sampling [136, 137]. In a normal down-sampling process, an anti-aliasing filter is required before the decimation so that the Nyquist sampling theorem is satisfied for the down-sampled signal. However, similar to that of the up-sampling, the down-sampling in the presence of RF-differed MN is unintentionally happened in the receiver. Therefore, the thesis assumes there is no anti-aliasing filter associated with the down-sampling process. As shown in Fig. 2.14, down-sampling the signal $\mathbf{r}(t)$ yielding $\mathbf{r}[l] = \mathbf{r}(l\Delta T'')$, where $l \in [0, \lfloor Tf_s/Q_d \rfloor]$ is an integer. $\Delta T'' = Q_d \Delta T$ refers to the increased sample duration, and Q_d is the down-sampling rate. Let $T = T_c$, the down-sampled signal can be written as:

$$\mathbf{r}[l] = \bar{\mathbf{s}}(l\Delta T'') = \bar{\mathbf{s}}[Q_d l] = [\mathbf{s}[0], \mathbf{s}[Q_d], \mathbf{s}[2Q_d], \cdots, \mathbf{s}[N-1]], \tag{2.10}$$

which contains each Q_d samples of $\bar{\mathbf{s}}[n]$. The digital realization of down-sampling is performed by multiplying the signal with the following down-sampling matrix

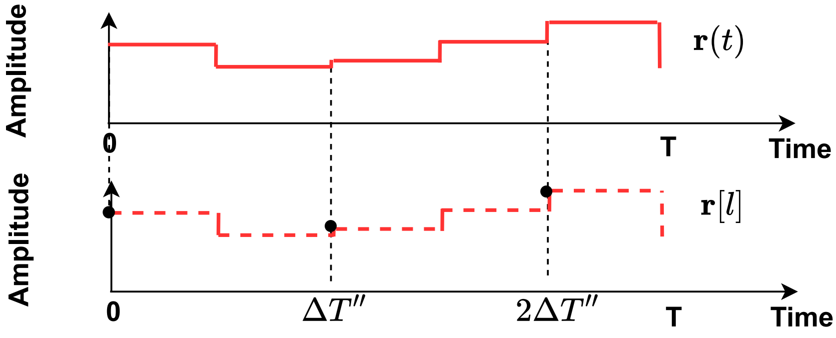

Figure 2.14: Unintentional down-sampling of $\mathbf{r}(t)$. The sample duration after down-sampling is $\Delta T''$ with down-sampling rate being $Q_d = 2$.

$\mathbf{D}$:

$$\mathbf{D} = \begin{pmatrix} \mathbf{1}_d & \mathbf{0} & \cdots & \mathbf{0} \\ \mathbf{0} & \mathbf{1}_d & \cdots & \mathbf{0} \\ \vdots & \vdots & \ddots & \vdots \\ \mathbf{0} & \mathbf{0} & \cdots & \mathbf{1}_d \end{pmatrix}, \tag{2.11}$$

where $\mathbf{1}_d = [1, 0, 0, \cdots, 0]_{1 \times Q_d}$, and $\mathbf{0}$ refers to a zero vector with the same size of $\mathbf{1}_d$.

Chapter 3

Mixed-Numerology Framework, Signals Transmission, and Interference Cancellation

3.1 Introduction

During the last few decades, the evolution of mobile communications has considerably driven the technical development in other fields [3]. In order to maintain the tightly coupled relationship between the mobile communication evolution and the socio-technical trends, the 5th generation wireless communication network is designed by taking into account the demand from vertical industries. As a result, three communication scenarios are proposed for different types of services with extremely diverse requirements [3], *i.e.*, enhanced mobile broadband, massive machine type communications, ultra-reliable and low latency communications. Among the three types of services, eMBB is the extend of the traditional broadband service, URLLC caters for the applications/services where extremely high reliability and low end-to-end delays are required (*e.g.*, vehicle to vehicle communication, remote medical treatment); while mMTC is for delay-tolerant devices with a connection density of up to 10^6 devices/km^2 [138].

As a solution to support such a multi-service coexistence system, network slicing is expected to play an important role in 5G and beyond, wherein the whole network is partitioned into slices and each of them is customised to meet the needs of specific user cases. With network slicing, different services need to share the same physical infrastructure. Hence, it could significantly reduce the cost for constructing the network and simplify the resource allocation and interference management to a considerable degree. Currently, most of the researches on network slicing focus on core network and media access control layer. From the CN point of view, NFV and SDN are the two dominant techniques under investigation; while research in the MAC layer mainly lies on resource allocation and isolation of wireless services [139].

On the other hand, as the foundation of wireless communication networks, the physical layer is an indispensable part of the future slicing mechanism. In a typical state of the art system, *e.g.*, LTE, all users are well synchronized in terms of baseband SCS and radio frequency sampling rate configurations to simplify the system design. However, to comply with the diverse requirements in 5G, slices are required to have different physical layer configurations [140]. For example, a large SCS (hence small symbol duration) is needed to meet the stringent latency requirements of the vehicle-to-vehicle communication. In contrast, small SCS (hence long symbol duration) is preferred for the delay-tolerant mMTC devices [34]. Mixed-numerology systems are formed with these slices operating on the common physical infrastructure, and unexpected signal attenuation and interference might be introduced to the system. Thus, the widely used signal detection algorithms, system analysis methods and traditional transceiver architectures may be invalid and should be re-designed.

As for the RF-differed MN system, it enables the coexistence of broadband and narrowband services, and thus maximizes the flexibility of costumed bandwidth design. In the 5G network, the simultaneously operating of mMTC and eMBB services constructs a typical RF-differed MN scenario, where the former one accommodates for the intensively distributed services, and is likely to have much lower RF processing bandwidth than the later one for the purpose to maintain low cost and power consumption. As two of the most important service types, it can be imagined that the coexistence of mMTC and eMBB will be a common case in the future network. Therefore, it becomes particularly important to clearly understand the potential problem that may come up with this situation. There is an exemplary case of RF-differed MN system scenario in the existing wireless communication system, *i.e.*, NB-IoT [68]. Constrained by the hardware complexity and signal processing capabilities, the low-end NB-IoT devices may have much smaller RF processing bandwidth as compared to the standard user equipment or based station.

Preliminary work has been done in [129] to investigate the uplink coexistence of NB-IoT and LTE from the physical layer perspective. However, a general and comprehensive study about the RF-differed MN system scenario is still missing in the literature. More importantly, none of the existing MN investigations takes both BB and RF configuration imparities into account. In order to accommodate for such a brand new mechanism, a full-featured framework that takes different physical layer configuration impieties into account is of importance and necessity in future networks. The contributions and novelties of this chapter are summarized as follows:

- The generalized circular convolution properties of DFT are specified into two theorems by considering up-sampling and down-sampling, respectively. These theorems provide the theoretical foundation for the advanced interference analysis and cancellation algorithms in both uplink and downlink of the proposed system model.
- A comprehensive MN framework is built based on practical 5G scenarios and use cases, within which four scenarios are categorized by considering the configurations imparities in both BB and RF. The uplink and downlink system models for the most generic scenario, *i.e.*, DBDR, are derived.
- The relationships among most of the key physical layer parameters are systematically derived, including subcarrier spacing, symbol duration, sampling rate, DFT size and waveforms for different scenarios, which constitutes the numerology framework for the proposed systems. Algorithms and system design are investigated based on such a framework.
- The closed-form power pre-compensation algorithms are derived for overcoming the signal distortion for both uplink and downlink cases. In addition, based on the derived overall signal collaboration model, low complexity but effective INI cancellation algorithms for SBDR cases are proposed by either joint detection in the uplink or precoding in the downlink.

Notations: $\{\cdot\}^H$ and $\{\cdot\}^T$ stand for the Hermitian conjugate and transpose operation, respectively. $\mathcal{E}\{\mathbf{A}\}$ and $\text{diag}\{\mathbf{A}\}$ denote the expectation of matrix $\mathbf{A}$ and a diagonal matrix formed by taking the diagonal elements of $\mathbf{A}$, respectively. $\text{diag}\{\mathbf{a}\}$ denotes forming a diagonal matrix using the vector $\mathbf{a}$. $\mathbf{I}_M$ and $M \times N$ zero matrix, respectively. In addition, $\mathbf{F}_N$ is used to express the N-point power normalized inverse DFT matrix with its i-th row and k-th column being $\frac{1}{\sqrt{N}}e^{j2\pi ik/N}$. The operator $*$ refers to linear convolution. $\text{mod}(a,b)$ means modulo operation and $|\mathbf{A}|^n$ refers to the n-th power of absolute values of all elements in matrix $\mathbf{A}$. To reuse the symbols, $\{\bar{\cdot}\}$ and $\{\hat{\cdot}\}$ are used to represent the symbols that are related to the uplink and downlink transmissions, respectively. In addition, the commonly used symbols and their meanings are listed in Table 3.1 for ease of reference. Note that symbol subscripts to denote different numerologies are omitted in the table due to the limited space. However, explicit symbols' meanings can be found in the chapter, *e.g.*, Δf_1 means the subcarrier spacing of slice1. All superscripts have also been excluded in Table 3.1 for the same reason.

Table 3.1: List of Important Symbols

Symbol	*Meaning*	*Symbol*	*Meaning*
Δf	Subcarrier spacing	L	The length of transmit symbol
S	RF processing bandwidth or Sampling rate	η	The value of shifted phase
B	System bandwidth	$\mathbf{\Phi}/\mathbf{\Psi}$	Phase shift matrices
M	Number of subcarriers in a slice band	$\mathbf{U}_Q/\mathbf{D}_Q$	Up-sampling and down-sampling matrices
Q	Sampling mismatch rate	$\mathbf{h}/\mathbf{H}$	Channel impulse response and frequency response
O	Subcarrier spacing mismatch rate	$\mathcal{H}$	Toeplitz channel matrix
ΔT	Symbol duration	$\mathbf{g}/\mathbf{G}$	Filter impulse response and frequency response
N	DFT size	$\mathcal{G}$	Toeplitz filter matrix
L_{CP}	The length of CP	$\mathbf{C}/\mathbf{R}$	CP insertion and removal matrices

* Subscripts that are used to denote different numerologies are omitted to keep the readability. For the same reason, all superscripts are excluded.

3.2 Mixed-Numerology Framework Construction

Considering that the frequency resource is split into subbands and each subband is assigned to one RAN slice. Each RAN slice could be shared by multiple users that have the same communication requirements such as data rate and latency. This implies that the users allocated to one slice do not have to be of the same type but with similar BB configurations. For example, smart phone and virtual reality have similar communication requirements. Hence, they can be assigned to the same slice and their differences are invisible at the physical layer. However, communication scenarios with significantly different requirements, *e.g.*, eMBB and V2V, should be categorized into different slices.

On the other hand, due to the hardware realization and expenses, devices in the same slice could have different RF configurations. In current wireless communication systems such as LTE, BSs are always expensive, equipped with many RF chains and processing units, and able to tune to different numerologies. However, for the next generation wireless networks, it is not feasible for a BS to contain RF chains for every single numerology that may connect to it. In addition, with the increasing deployment of Picocells and Femtocells [141, 142], the use of low-cost and reasonable simple BSs gradually becomes the mainstream, especially for mmWave scenarios. As a consequence, in this thesis, it is assumed that each BS has one single RF chain with fixed bandwidth to process signals of all slices, while each slice could be processed by specific RF chains at each UE that may have different RF configurations. However, the baseband processing at the BS could be different among slices.

With the assumptions mentioned above, it is worth remarking that **there is not a one-to-one-correspondence between 'slice' and 'numerology', devices in one slice could have different numerologies in terms of RF configuration**. In other words, a transmitter and a receiver with different sampling rates or RF processing bandwidths construct an MN system (more specifically, RF-differed MN system) even they are assigned to one slice. As has been discussed, one of the key challenges for the proposed mixed-numerology system is the mitigation/cancellation of INI. It is worth mentioning that a slice can be interfered by more than one neighbouring slice above and/or below its allocated subband. Hence, a three-slice (and more) model, *e.g.*, slice1-slice2-slice3, could be considered to present a general case for the interference analysis. However, because the interference generated from each slice is linearly superposed in each victim subband, the model can be decoupled as three simple ones (proof of the generality is provided in Appendix. A), *i.e.*, slice1-slice2, slice2-slice3 and slice1-slice3. In this chapter, without loss of generality, two slices are considered where each contains one UE for simplifying the derivation and easy understanding.

3.2.1 Scenarios Categorization

According to the configuration differences at BB and RF, MN systems can be categorised into four scenarios. To be specific, the four scenarios are defined in details as follows:

SBSR (Numerologies have the same BB and the same RF configurations)

The subcarrier spacing values in the two numerologies satisfy $\Delta f_1 = \Delta f_2$ and the RF processing bandwidths of the two UEs are equal to the whole system bandwidth, *i.e.*, $S_1 = S_2 = B$. According to the OFDM modulation principle, the two numerologies can be orthogonally multiplexed without generating any interference. Typical configured LTE/LTE-A is such a kind of single-service or single-numerology system, where all services have the same configurations.

DBSR (Numerologies have different BB but the same RF configurations)

This scenario refers to the BB-differed MN, where UEs assigned to the two access resource slices have the same RF processing bandwidth, which is also the same as the system bandwidth, *i.e.*, $S_1 = S_2 = B$. However, the baseband configurations for the two numerologies are different, *i.e.*, $\Delta f_1 \neq \Delta f_2$. For example, considering that the two slices are used for eMBB and V2V communications, respectively. Due to the short latency requirement, the symbol duration for the V2V communications slice may be significantly smaller than the eMBB service. However, the two UEs may have the same RF configurations.

SBDR (Numerologies have the same BB but different RF configurations)

This scenario refers to the RF-differed MN, where UEs assigned on the two slices have different RF configurations and at least one of them is smaller than the BS sampling rate. Whereas the two slices share the same BB configuration, *e.g.*, $S_1 \neq S_2$, and $\Delta f_1 = \Delta f_2$. A representative example of the scenario is the NB-IoT. Compared with the LTE system configurations of 30.72 MHz sampling rate[1] at both LTE UE and BS, the RF processing bandwidth in NB-IoT UE is significantly smaller. The benefits of such design are also significant, as it enables the NB-IoT device to bear only 15% of complexity compared with the legacy LTE UE and contributes to a significant saving of cost and power consumption.

DBDR (Numerologies have different BB and different RF configurations)

In this scenario, $S_1 \neq S_2$ and $\Delta f_1 \neq \Delta f_2$. DBDR is the most complex scenario by considering both RF and BB configuration difference. However, it is also the most generic and practical one since it can maximize the potential of MN by catering for the optimal individual service requirements from both RF and BB perspectives. In the DBDR scenario, INI could be generated from two sources, i.e., either SCS or sampling rate difference, and it could have the worst performance among the four scenarios.

---

[1] Note that such values are only used as examples, the symbols in equations are all normalized and do not correspond to any specific value.

The new communication architecture of the MN could significantly affect the existing system design and the algorithms that have been widely used in the single-service system. For example, channel circular convolution property, channel equalization and estimation, and synchronization algorithms may not be applicable in MN systems. Considering that the system models and analyses in DBDR scenario can be easily converted to the other scenarios. It is essential to construct a comprehensive framework for the most generic physical MN scenario as the foundation of system performance analysis and algorithm design.

3.2.2 System Configurations

The configuration relationships between numerologies are investigated before building a complete system model. Specifically, there are at least four key parameters, namely, RF sampling rate, baseband subcarrier spacing (or symbol duration), DFT size (or baseband sampling rate) and waveforms, which may fundamentally affect the system design and performance. In the next, $\{\cdot\}_{B1}$, $\{\cdot\}_{B2}$, $\{\cdot\}_{U1}$ and $\{\cdot\}_{U2}$ are used to denote the BS parameters for slice1, BS parameters for slice2, UE 1 parameters for slice1 and UE 2 parameters for slice2, respectively.

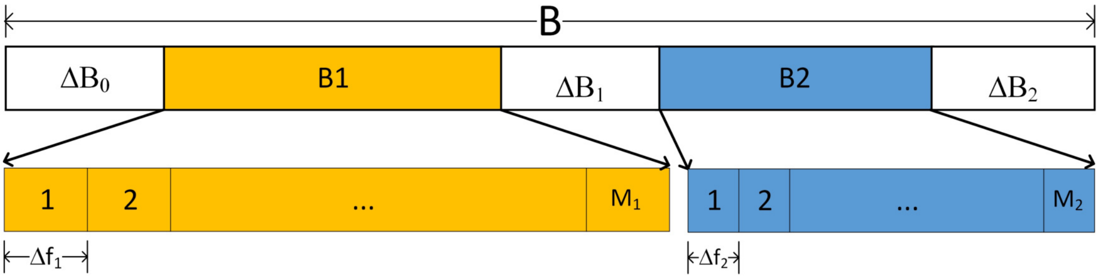

Figure 3.1: Spectrum allocation of the two slices within the system bandwidth: $B_1 = M_1\Delta f_1$ for slice1 and $B_2 = M_2\Delta f_2$ for slice2.

Without loss of generality, it is assumed that the system bandwidth B is normalized, *i.e.*, $B = 1$. As shown in Fig. 3.1, the bandwidth of slice1 and slice2 are B_1 and B_2, respectively, and ΔB_1 is the guard band in between. Define M_1 and M_2 as the number of subcarriers in the first and second numerologies, respectively. Besides, ΔB_0 and ΔB_2 are the band on the left and right of slice1 and slice2, respectively.

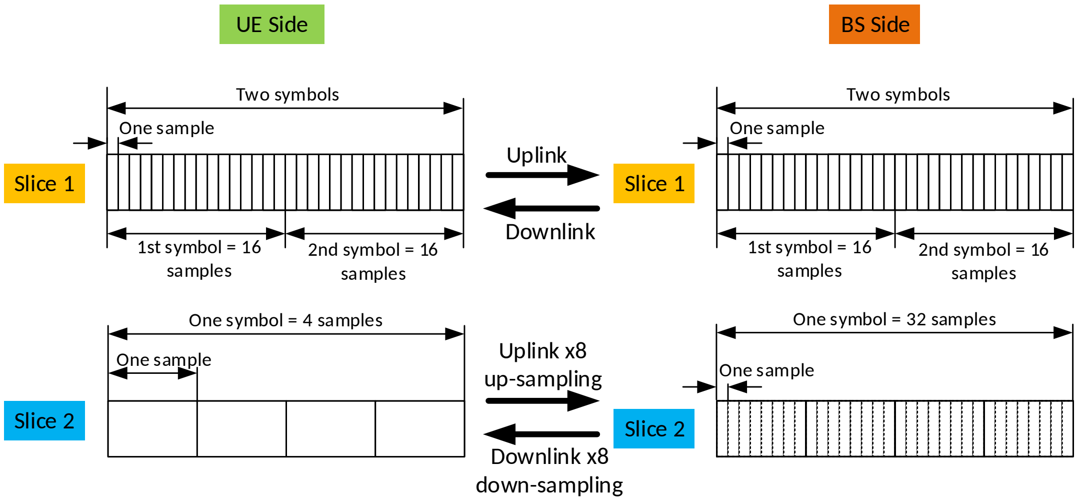
UE Side
BS Side
Two symbols
One sample
Slice 1
1st symbol = 16 samples
2nd symbol = 16 samples
Uplink
Downlink
One symbol = 4 samples
One sample
Slice 2
Uplink x8 up-sampling
Downlink x8 down-sampling
One symbol = 32 samples

Figure 3.2: Frame structure example of DBDR system with two slices: $\Delta T_2 = 2\Delta T_1$ (*i.e.*, $O = 2$ and $\Delta f_1 = 2\Delta f_2$). At UE side, DFT size $N_{U1} = 16$, $N_{U2} = 4$; RF sampling rate $S_{U1} = 8S_{U2}$, (*i.e.*, $Q = 8$). At the BS side, DFT size $N_{B1} = 16$, $N_{B2} = 32$; RF sampling rate $S_{B1} = S_{B2}$ (Note that the two slices are frequency domain multiplexed).

RF imparity

In principle, the RF bandwidth or sampling rates in different numerologies can be arbitrary. However, in practice, it is always beneficial to design a system such that the sampling rate at BS is integer number times that at any UE. For example, in Fig. 3.2, the sampling rate at the BS is 8 times larger as the sampling rate at UE 2. Without loss of generality, it is assumed the BS has the same RF configuration as UE 1, and UE 2 is a cost and energy limited device (*e.g.*, IoT device) with $Q \in \mathbb{Z} \geq 1$ times lower sampling rate[2]. The normalized sampling rates can be expressed as

$$S_{B1} = S_{B2} = S_{U1} = B, \quad S_{U2} = \frac{B}{Q} \, . \tag{3.1}$$

Baseband imparity

Similarly to the RF configuration, it is beneficial to design a MN system with an integer least common multiplier (LCM) symbol duration T_{LCM} for all slices [34], *e.g.*, as shown in Fig. 3.2, where slice1 and slice2 symbol duration and subcarrier spacing satisfy the relationship $\Delta T_2 = 2\Delta T_1$ (and $\Delta f_1 = 2\Delta f_2$). In practice, this design principle has been adopted as a basis for the current 5G air interface standardization. For example, assuming the subcarrier spacing for eMBB is 15 kHz, the subcarrier spacing for IoT devices could be selected from the list of 15/8, 15/4, 15/2 kHz, etc. Therefore, it is assumed that the subcarrier spacing in slice1 is $O \in \mathbb{Z} \geq 1$ times wider than the one in slice2, *i.e.*

---

[2] Here it is assumed that $Q \in \mathbb{Z}$, which will facilitate the RF and baseband processing and it aligns with the 3GPP standardization [143].

$$\Delta f_1 = O\Delta f_2 \; ; \quad \Delta T_2 = O\Delta T_1 \; . \tag{3.2}$$

From equations Eq. (3.1) and Eq. (3.2), it can be seen that UE 2 has a lower sampling rate, but a larger symbol duration. *i.e.*, both $Q \geq 1$ and $O \geq 1$.

DFT/IDFT size and symbol duration in samples

DFT/IDFT size in OFDM based systems depends on the sampling rate and subcarrier spacing. In a MN system, this value could be different among slices and also between transmitter and receiver for the same slice due to the RF and/or BB imparities. With the assumptions in this chapter, it can be achieved that $N_{B1} = S_{B1}/\Delta f_1$ and $N_{B2} = S_{B2}/\Delta f_2$. In addition, by giving Eq. (3.1) and that $B_1 = M_1\Delta f_1$ and $B_2 = M_2\Delta f_2$ (as shown in Fig. 3.1), the DFT sizes for the two slices at the BS are:

$$N_{B1} = \frac{M_1}{B_1}; \; N_{B2} = \frac{M_2}{B_2}. \tag{3.3}$$

Taking into account the configuration relationships between UE and BS, the DFT sizes of the two UEs could be calculated as:

$$N_{U1} = N_{B1}; \; N_{U2} = \frac{N_{B2}}{Q} \; . \tag{3.4}$$

As has been assumed that the BS has a single RF chain to process both slices (*i.e.*, the sampling rate S is valid for both slice1 and slice2), while has separate BB chain for slice1 and slice2, *i.e.* has different subcarrier spacing Δf_1 and Δf_2.

It should be noted that in the LTE system, a certain transmission bandwidth is partitioned into equal segments according to the unique subcarrier spacing. *e.g.*, with 5% bandwidth as the guardband in both sides, a typical 20 MHz transmission bandwidth could be divided into 100 physical resource blocks (PRBs) with each contains 12 LTE subcarriers. Hence, the frequency resource could be allocated to different users in the unit of PRB. However, in the mixed-numerology systems, due to the different BB configurations among slices, there is not a unified frequency resource allocation granularity as that of the LTE system. Taking the model in this chapter as an example, while allocating the bandwidth to the two slices, B_1 and B_2 should be carefully selected to ensure that they are integer multiple times of their corresponding subcarrier spacing. In addition, N_{B1}, N_{B2}, N_{U1} and N_{U2} can take the values of the integer number power of 2 to facilitate FFT operation. Eq. (3.4) reveals that UE 1 has the same DFT size as the BS to make the system free of self-interference. However, for slice2, due to the RF bandwidth differences between the transmitter and receiver, the DFT/IDFT sizes at BS and UE are different. Specifically, UE 2 can take Q-time smaller DFT than that of the BS.

Let us assume that the CP lengths for slice1 and slice2 are $L_{CP,1}$ and $L_{CP,2}$ in the unit of their corresponding UE samples, respectively. With the BS and UE sampling rates relationship in Eq. (3.1), the CP length for slice2 can be equivalently expressed as $QL_{CP,2}$ BS samples. By using Eq. (3.2), the symbol duration for the two slices including CP overhead (in the unit of BS samples) can be written as

$$L_1 = N_{B1} + L_{CP,1} \ ; \quad L_2 = N_{B2} + QL_{CP,2} \ . \tag{3.5}$$

Note that Eq. (3.5) is different from Eq. (3.2) where the absolute symbol duration is used. In Eq. (3.5), the symbol duration is expressed as the number of BS samples to facilitate the baseband processing and derivations.

Subband filtering waveforms

Due to the multi-numerology between slices and high out of band emission of the OFDM system, the performance of the proposed system may be significantly limited by INI, especially the subcarriers located at the edges of the subbands. To reduce the OoBE and mitigate INI, F-OFDM is considered as an example waveform in this chapter.

Let us denote the subband filter impulse response for the two resource slices at the BS as

$$\begin{aligned} \mathbf{g}_{T1} &= \boldsymbol{\Psi}_1 \mathbf{g}_{T1,p} \in \mathbb{C}^{N_{B1}\times 1} \\ \mathbf{g}_{T2} &= \boldsymbol{\Psi}_2 \mathbf{g}_{T2,p} \in \mathbb{C}^{N_{B2}\times 1} \ , \end{aligned} \tag{3.6}$$

where $\mathbf{g}_{T1,p}$ and $\mathbf{g}_{T2,p}$ are the prototype filter for slice1 and 2, respectively[3]. The passband of $\mathbf{g}_{T1,p}$ and $\mathbf{g}_{T2,p}$ are $[0, B_1]$ and $[0, B_2]$, respectively. $\boldsymbol{\Psi}_1$ and $\boldsymbol{\Psi}_2$ are diagonal matrices to shift the two prototypes filters to the targeting subbands where the two slices are assigned. The i-th diagonal elements of $\boldsymbol{\Psi}_1 \in \mathbb{C}^{N_{B1}\times N_{B1}}$

---

[3] A typical setup for filter length is half DFT size in the F-OFDM system [82]. However, we can always pad zeros at the rear of the filters.

and $\mathbf{\Psi}_2 \in \mathbb{C}^{N_{B2}\times N_{B2}}$ are

$$\Psi_1(i) = e^{j\cdot 2\pi i\eta_1/N_{B_1}} \;\; ; \;\; \Psi_2(i) = e^{j\cdot 2\pi i\eta_2/N_{B_2}} \;\; , \tag{3.7}$$

where $\eta_1 = \Delta B_0 N_{B1}$ and $\eta_2 = (\Delta B_0 + \Delta B_1 + B_1)N_{B2}$ are the shifted phase to move the signals to the corresponding frequency subbands. Thus the passband of the two slices' filters $\mathbf{g}_{T1}$ and $\mathbf{g}_{T2}$ are $[\Delta B_0, \Delta B_0 + B_1]$ and $[\Delta B_0 + \Delta B_1 + B_1, \Delta B_0 + \Delta B_1 + B_1 + B_2]$, respectively.

At the UE side, UE 1 can also perform the subband filtering to further reduce INI. However, for UE 2, baseband filtering is not feasible due to the small baseband processing bandwidth. Instead, an RF filter can equivalently take the role of mitigating the interference.

3.3 Generalized Circular Convolution Properties

One of the paramount advantages of the OFDM system is that it enables low complexity interference free one-tap channel equalization. The rationale is that the original circular convolution property (O-CCP) of DFT [30], where the same size IDFT and DFT pair operating at transmitter and receiver respectively, can diagonalize the channel matrix. This property has been widely adopted in single-service OFDM systems, including 3GPP LTE, IEEE 802.11, etc. However, in the multi-service system, the IDFT and DFT size may be different at the transmitter and receiver, which could invalidate O-CCP. Hence, the generalized circular convolution property (G-CCP) is proposed to cater for such new scenarios, which has much more extensive applicability than the original property.

Before deriving G-CCP, let us briefly recall the O-CCP of the DFT processing. According to the **Theorem 4.8.2** in [30], if we define a circular matrix $\mathcal{H} \in \mathbb{C}^{N\times N}$ with its first column being $\mathbf{h} = [h_1, h_2, \cdots, h_N]^T$, and a power normalized IDFT matrix $\mathbf{F}_N \in \mathbb{C}^{N\times N}$. Then we can have $\mathbf{F}_N^H \mathcal{H} \mathbf{F}_N = diag(\lambda_1, \cdots, \lambda_n)$, where $(\lambda_1, \cdots, \lambda_n)$ are the eigenvalues of matrix $\mathcal{H}$. Hence, the circular matrix is diagonalized with paired DFT processing. For the purpose to extend the original property to a generalized form, un-paired DFT processing is considered, which is different from the paired ones in two aspects: 1) the DFT and IDFT sizes are different; 2) the phase between the DFT and IDFT is not aligned. Here, the term 'phase' is used to denote the state of DFT/IDFT matrix after circulant-shift. For example, the phase of the original DFT matrix is 0. To set its phase to π is equivalent to shift the original matrix circularly by half of the DFT size.

To incorporate these two aspects, $\mathbf{F}_M \in \mathbb{C}^{M\times M}$ is defined as another power normalized IDFT matrix with $M = N/Q$, and $\mathbf{\Phi}_\eta$ is an N-dimensional phase shifting diagonal matrix with its i-th ($i = 0, 1, \cdots, N-1$) diagonal elements being

$$\Phi_\eta(i) = e^{j\cdot 2\pi i\eta/N} \ , \ \ \eta \in \mathbb{R} \tag{3.8}$$

where η indicates the value of the shifted phase. By multiplying $\mathbf{\Phi}_\eta$ and the DFT/IDFT matrix, the phase of the DFT/IDFT matrix is shifted by η. In addition, consider the different matrix size of $\mathcal{H}$ and $\mathbf{F}_M$, an up-sampling matrix $\mathbf{U}_Q \in \mathbb{R}^{N\times M}$ by a factor of Q is introduced to enable the multiplication between them. Specifically, $\mathbf{U}_Q$ can be formed as:

$$\mathbf{U}_Q = \begin{pmatrix} \mathbf{1}_u & 0 & \cdots & 0 \\ 0 & \mathbf{1}_u & \cdots & 0 \\ \vdots & \vdots & \ddots & \vdots \\ 0 & 0 & \cdots & \mathbf{1}_u \end{pmatrix}, \tag{3.9}$$

where $\mathbf{1}_u = [1, 1, \cdots, 1]^T_{1\times Q}$. It should be noted that N and M can be any value in specific cases as long as $N/M = Q$. Then, we can have the generalized circular convolution property with up-sampling (G-CCP-US) as:

Theorem 1 (G-CCP-US): Let us define $\mathbf{H}_U = \mathbf{F}_N^H \mathcal{H} \mathbf{\Phi}_\eta \mathbf{U}_Q \mathbf{F}_M$, then we have

$$\mathbf{H}_U = \mathbf{F}_N^H \mathcal{H} \mathbf{\Phi}_\eta \mathbf{U}_Q \mathbf{F}_M = \frac{1}{\sqrt{Q}} \mathbf{H}_O \mathbf{\Theta} \mathbf{\Lambda}, \tag{3.10}$$

where

$$\mathbf{H}_O = \sqrt{N}\mathrm{diag}(\mathbf{F}_N^H \mathbf{h}) \ , \tag{3.11}$$

and

$$\mathbf{\Theta} = [\mathbf{I}_{N,1}; \mathbf{I}_{N,2}]. \tag{3.12}$$

$\mathbf{H}_O$ is the matrix form of the N-point DFT of $\mathbf{h}$. $\mathbf{I}_{N,1}$ and $\mathbf{I}_{N,2}$ are obtained by taking the last u and the first $(N-u)$ rows of identity matrix $\mathbf{I}_N$, where $u = \mathrm{mod}(\eta, N)$. $\mathbf{\Lambda}$ is an $(N \times M)$-dimension matrix given by $\mathbf{\Lambda} = [diag(\boldsymbol{v}_0), diag(\boldsymbol{v}_1), \cdots, diag(\boldsymbol{v}_{Q-1})]^T$, with $\boldsymbol{v}_l$ being Q-length vector and its i-th ($0 \le i \le M-1$) element is obtained as follows

$$\upsilon_l(i) = \frac{1 - e^{j\cdot\frac{2\pi i(Q+lM)}{N}}}{1 - e^{j\cdot\frac{2\pi i(1+lM)}{N}}} \ . \tag{3.13}$$

Moreover, the power of $\upsilon_l(i)$ can be written as

$$|\upsilon_l(i)|^2 = \left[\frac{\sin(\frac{\pi i(Q+lM)}{N})}{\sin(\frac{\pi i(1+lM)}{N})}\right]^2 \ . \tag{3.14}$$

Proof. See Appendix B. □

From the G-CCP-US proposed in Theorem 1 shown in Eq. (3.10), we can find that the matrix $\mathcal{H}$ cannot be diagonalized by the un-paired DFT/IDFT processing and $\mathbf{H}_U$ is with the form where block matrices stacked below each other. In general, if we assume that $mod(\mu, M) = 0$, such block matrices are all diagonal matrices. However, when the constraint $mod(\mu, M) = 0$ cannot hold, each block matrix in $\mathbf{H}_U$ is shifted according to the value of $mod(\mu, M)$. Moreover, the elements of $\mathbf{H}_U$ are weighted by $\mathbf{\Lambda}$ in a point-wise sense. Although $\mathbf{H}_U$ has a stacked form, it can be transformed into a diagonal matrix with some matrix exchange operations, as shown in Eq. (3.16) and Eq. (3.17). This is also the reason why the proposed theorem is called generalized circular convolution property. When the up-sampling rate $Q = 1$ and phase shifter $\eta = 0$, Theorem 1 reduces to the O-CCP [30].

One of the applications of G-CCP-US is in telecommunication. Consider a complete multicarrier communication system where the transmitter sampling rate is $1/Q$ that of the receiver's, and $\mathcal{H}$ is the channel matrix and $\mathbf{\Phi}_\eta$ is applied to shift the signal to the allocated subcarriers. By defining $\mathbf{a}_M \in \mathbb{C}^{M\times 1}$ as the transmit signal that is assigned to M consecutive subcarriers (indicated by $m \in [\eta, \eta+1, \cdots, \eta+M-1]$), the received signal can be written as:

$$\mathbf{y}_U = \mathbf{F}_N^H \mathcal{H} \mathbf{\Phi}_\eta \mathbf{U}_Q \mathbf{F}_M = \frac{1}{\sqrt{Q}} \mathbf{H}_O \mathbf{\Theta} \mathbf{\Lambda} \mathbf{a}_M \ , \tag{3.15}$$

By using simple matrix exchange operation, Eq. (3.15) can be equivalently written as the following form:

$$\mathbf{y}_U = \tilde{\mathbf{H}}_U \tilde{\mathbf{a}}_M \ , \tag{3.16}$$

where $\tilde{\mathbf{H}}_U = \frac{1}{\sqrt{Q}} \mathbf{H}_O \tilde{\mathbf{\Lambda}}$ and

$$\tilde{\mathbf{\Lambda}} = \mathrm{diag}(\mathbf{\Theta}[\boldsymbol{\upsilon}_0, \boldsymbol{\upsilon}_1, \cdots, \boldsymbol{\upsilon}_{Q-1}]^T) \ . \tag{3.17}$$

$\tilde{\mathbf{a}}_M = \mathbf{\Theta}[\mathbf{a}_M,\mathbf{a}_M,\cdots,\mathbf{a}_M]^T \in \mathbb{C}^{N\times 1}$ is a (elements location exchanged) repetition version of $\mathbf{a}_M$ by a factor of Q. From Eq. (3.16), we can find that $\mathbf{H}_U$ is transformed to a diagonal matrix $\tilde{\mathbf{H}}_U$ with the matrix exchange operation. Thus, by considering *any* consecutive M rows from $\mathbf{y}_U$, the transmitted signals can be detected by using one-tap channel equalization without generating interference. However, according to Eq. (3.14), the elements power of $\tilde{\mathbf{\Lambda}}$ could be different and the signal distortion among subcarriers will be generated. On the other hand, it shows that the power of $\mathbf{a}_M$ is expanded across the whole bandwidth (*i.e.*, by vector $\tilde{\mathbf{a}}_M$). It implies that interference will be generated by such a system to the whole bandwidth, and thus a subband filter could be adopted to reduce the OoBE and interference to other users.

Next, let us consider the generalized circular convolution property with the down-sampling operation (G-CCP-DS). Assume $\mathcal{H}$, $\mathbf{F}_N$, $\mathbf{\Theta}$, $\mathbf{\Phi}_\eta$, $\mathbf{F}_M$ and $\mathbf{H}_O$ have the same meaning as in Theorem 1. In addition, define $\mathbf{D}_Q \in \mathbb{R}^{M\times N}$ as the down-sampling matrix by a factor of Q, which can be formed as:

$$\mathbf{D}_Q = \begin{pmatrix} \mathbf{1}_d & 0 & \cdots & 0 \\ 0 & \mathbf{1}_d & \cdots & 0 \\ \vdots & \vdots & \ddots & \vdots \\ 0 & 0 & \cdots & \mathbf{1}_d \end{pmatrix}, \tag{3.18}$$

and $\mathbf{1}_d = [1, 0, 0, \cdots, 0]_{1\times Q}$. Similarly, the size of $\mathbf{D}_Q$ could vary in different cases. We can have the following Theorem:

Theorem 2 (G-CCP-DS) Define $\mathbf{H}_D = \mathbf{F}_M^H \mathbf{D}_Q \mathbf{\Phi}_\eta \mathcal{H} \mathbf{F}_N$, then we have the following generalized down-sampling circular convolution property

$$\mathbf{H}_D = \mathbf{F}_M^H \mathbf{D}_Q \mathbf{\Phi}_\eta \mathcal{H} \mathbf{F}_N = \frac{1}{\sqrt{Q}} \check{\mathbf{\Lambda}} \mathbf{H}_O \ , \tag{3.19}$$

where $\check{\mathbf{\Lambda}} = [\mathbf{I}_M, \mathbf{I}_M, \cdots, \mathbf{I}_M]\mathbf{\Theta}$ is a repetition version of identity matrix $\mathbf{I}_M$ by a factor of Q (elements location exchanged).

Proof. See Appendix C. ☐

Theorem 2 implies that G-CCP-DS is very similar to G-CCP-US except that its elements are not weighted, *i.e.*, no signal distortion. Similarly, to apply the Theorem 2 in telecommunication systems, it is assumed that in a complete multicarrier communication system where the transmitter sampling rate is Q times as that of the receiver's, and $\mathbf{a}_N \in \mathbf{C}^{N\times 1}$ is the transmit signal vector, $\mathcal{H}$ is the channel matrix and $\mathbf{\Phi}_\eta$ is applied to shift the signal to the allocated subcarriers. Thus, the received signal can be written as:

$$\mathbf{y}_D = \mathbf{F}_M^H \mathbf{D}_Q \boldsymbol{\Phi}_\eta \mathcal{H} \mathbf{F}_N \mathbf{a}_N = \frac{1}{\sqrt{Q}} \check{\boldsymbol{\Lambda}} \mathbf{H}_O \mathbf{a}_N \ , \tag{3.20}$$

By using simple matrix exchange operation, Eq. (3.20) can be equivalently expressed as the following multiplication

$$\mathbf{y}_D = \frac{1}{\sqrt{Q}} \sum_{l=0}^{Q-1} \mathbf{H}_D(l) \tilde{\mathbf{a}}_N(l) \ , \tag{3.21}$$

where $\mathbf{H}_D(l) \in \mathbb{C}^{M\times M}$ is a **diagonal** matrix by taking the $(lM+1)$-th to $(l+1)M$-th diagonal elements of $\mathbf{H}_D = \mathrm{diag}(\boldsymbol{\Theta}\mathbf{h})$ as its diagonal elements. $\tilde{\mathbf{a}}_N(l)$ is the l-th sub-vector of $\tilde{\mathbf{a}}_N = \boldsymbol{\Theta}\mathbf{a}_N$ by taking its $(lM+1)$-th to $(l+1)M$-th elements. From Eq. (3.21), we can find that even with the DFT/IDFT pair mismatch at the left and right of the circular matrix $\mathcal{H}$, the circular convolution property still holds in a generic sense. However, due to the receiver bandwidth reduction, the transmitter signals are aliased at the receiver. When *any* consecutive M non-zero element in $\mathbf{a}_N$ are sent, the received signal is degraded as $\mathbf{y}_D = \mathbf{H}_O(l)\mathbf{a}_N(l)$ and one-tap interference free channel equalizer can be applied. Again, when $Q = 1$ and $\eta = 0$, Eq. (3.19) reduces to the O-CCP.

G-CCP-US and G-CCP-DS in Theorem 1 and 2, respectively, build a foundation for the MN system with the transmitter and receiver sampling rate (and system bandwidth) mismatch. In the sequel, based on Theorem 1 and 2, the system model, equalizer, and interference cancellation algorithms are derived for the most generic scenario (*i.e.*, DBDR), by considering both BB and RF configuration differences between slices. In addition, detailed performance analyses with novel insights are presented.

3.4 Uplink Mixed-Numerology System

3.4.1 DBDR System Model

Assume the transmit signals vector for slice1 and 2 are $\mathbf{a}_1 \in \mathbb{C}^{M_1\times 1}$ and $\mathbf{a}_2 \in \mathbb{C}^{M_2\times 1}$, respectively. Following the traditional CP-OFDM procedure of IDFT and CP insertion, as shown in Fig. 3.3, the signals at two UEs can be written in matrix form as:

$$\bar{\mathbf{b}}_1 = \mathbf{C}_1 \boldsymbol{\Psi}_1 \tilde{\mathbf{F}}_{N_{U1}} \mathbf{a}_1 \ ; \quad \bar{\mathbf{b}}_2 = \bar{\mathbf{C}}_2 \mathbf{F}_{N_{U2}} \mathbf{a}_2 \ , \tag{3.22}$$

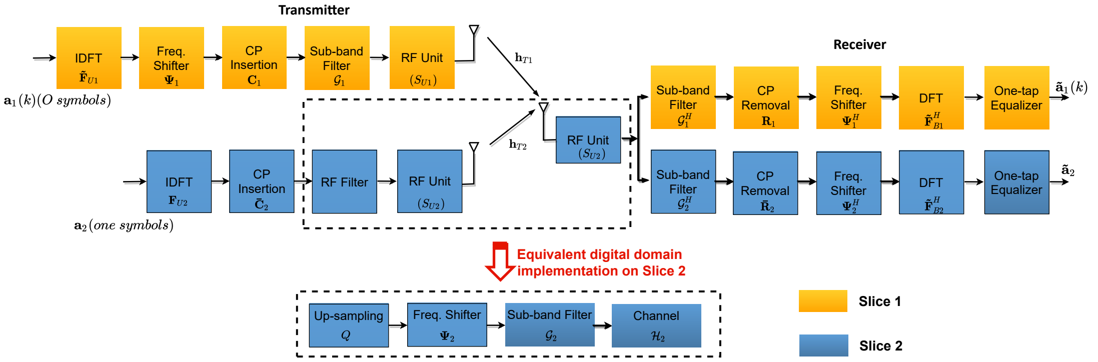
Transmitter
IDFT $\tilde{\mathbf{F}}_{U1}$
Freq. Shifter $\mathbf{\Psi}_1$
CP Insertion $\mathbf{C}_1$
Sub-band Filter $\mathcal{G}_1$
RF Unit (S_{U1})
$\mathbf{h}_{T1}$
$\mathbf{a}_1(k)(O\ symbols)$
IDFT $\mathbf{F}_{U2}$
CP Insertion $\bar{\mathbf{C}}_2$
RF Filter
RF Unit (S_{U2})
$\mathbf{h}_{T2}$
$\mathbf{a}_2(one\ symbols)$
Receiver
RF Unit (S_{U2})
Sub-band Filter $\mathcal{G}_1^H$
CP Removal $\mathbf{R}_1$
Freq. Shifter $\mathbf{\Psi}_1^H$
DFT $\tilde{\mathbf{F}}_{B1}^H$
One-tap Equalizer
$\tilde{\mathbf{a}}_1(k)$
Sub-band Filter $\mathcal{G}_2^H$
CP Removal $\bar{\mathbf{R}}_2$
Freq. Shifter $\mathbf{\Psi}_2^H$
DFT $\tilde{\mathbf{F}}_{B2}^H$
One-tap Equalizer
$\tilde{\mathbf{a}}_2$
Equivalent digital domain implementation on Slice 2
Up-sampling Q
Freq. Shifter $\mathbf{\Psi}_2$
Sub-band Filter $\mathcal{G}_2$
Channel $\mathcal{H}_2$
Slice 1
Slice 2

Figure 3.3: Transmitter and receiver block diagram of DBDR MN system for uplink transmission. (Note that the downlink transmission case is similar, thus, is omitted in this thesis.)

where $\tilde{\mathbf{F}}_{N_{U1}} \in \mathbb{C}^{N_{U1}\times M_1}$ is the first M_1 columns of the N_{U1}-point normalized IDFT matrix. The function of $\mathbf{\Psi}_1$ is to shift the signals to the corresponding frequency spectrum to where the slice is assigned. Note that the frequency shift at UE 2 is actually performed by the RF component, which will be explained later.

The CP insertion matrices for the two UEs are $\mathbf{C}_1 = [\mathbf{0}_{L_{CP,1}\times(N_{U1}-L_{CP,1})}, \mathbf{I}_{L_{CP,1}}; \mathbf{I}_{N_{U1}}]$, and $\bar{\mathbf{C}}_2 = [\mathbf{0}_{L_{CP,2}\times(N_{U2}-L_{CP,2})}, \mathbf{I}_{L_{CP,2}}; \mathbf{I}_{N_{U2}}]$, respectively. Note that the semicolons in CP expressions denote the column combination operation. $L_{CP,1}$ and $L_{CP,2}$ are the CP length in *UE samples*. One should note that the sample duration of UE 2 is Q times longer than that of UE 1 (as shown in Fig. 3.2).

As shown in Fig. 3.3, with a low OoBE subband filtering (*i.e.*, F-OFDM), we can write the output of the subband filter for the two slices as

$$\bar{\mathbf{c}}_1 = \mathcal{G}_1\bar{\mathbf{b}}_\mathbf{1} + \boldsymbol{\xi}_1 \quad \text{and} \quad \bar{\mathbf{c}}_2 = \mathcal{G}_2\tilde{\mathbf{\Psi}}_2\mathbf{U}_Q\bar{\mathbf{b}}_\mathbf{2} + \boldsymbol{\xi}_2\ , \tag{3.23}$$

where $\mathcal{G}_i \in \mathbb{C}^{L_i\times L_i}$ is the matrix form of subband filtering operation. It is a Toeplitz matrix with its first column and first row being $[\mathbf{g}_{Ti}; \mathbf{0}_{(L_i-N_{Bi})\times 1}]$ and $[g_{Ti}(1), \mathbf{0}_{1\times(L_i-1)}]$, respectively. $\tilde{\mathbf{\Psi}}_2 \in \mathbb{C}^{L_2\times L_2}$ is the equivalent frequency shifter at UE 2, and its i-th diagonal element is $e^{j\cdot 2\pi(i-QL_{CP,2}-1)\eta_2/N_{B2}}$. $\boldsymbol{\xi}_1$ and $\boldsymbol{\xi}_2$ are the ISI generated from the filter tails in the F-OFDM system. With proper filter and system frame structure design, ISI is negligible and thus will be omitted in this chapter to focus on INI, *i.e.*, $\boldsymbol{\xi}_1 = \boldsymbol{\xi}_2 = \mathbf{0}$. However, the detailed analysis of ISI for UFMC based DBSR system can be found in [34]. As shown in Fig. 3.3, $\mathcal{G}_2\tilde{\mathbf{\Psi}}_2\mathbf{U}_Q\bar{\mathbf{b}}_\mathbf{2}$ denotes equivalent digital domain implementation, where the digital subband filter $\mathcal{G}_2$ replaces RF filter with equivalent filter response in the digital domain.

According to Eq. (3.5), the symbol duration of the slice2 is O times as long as that of slice1. To completely express the system model and analyze the interference, it is necessary to consider at least O symbols in the first slice (*e.g.*, in Fig. 3.2, $O = 2$.). Let us denote $\bar{\mathbf{c}}_{o1}$ as a vector formed by contiguous O symbols in slice1, *i.e.* $\bar{\mathbf{c}}_{o1} = [\bar{\mathbf{c}}_1(0),\bar{\mathbf{c}}_1(1),\cdots,\bar{\mathbf{c}}_1(O-1)]^T$.

Let us define multi-path fading channel impulse responses of the two UEs to the BS as $\mathbf{h}_{T1}$ and $\mathbf{h}_{T2}$, respectively, and the channel gain $\mathcal{E}[\mathbf{h}_{T1}^H\mathbf{h}_{T1}] = \rho_1^2$ and $\mathcal{E}[\mathbf{h}_{T2}^H\mathbf{h}_{T2}] = \rho_2^2$. In addition, $\bar{\mathcal{H}}_i$ (for $i = 1, 2$) is the equivalent Toeplitz channel matrix. Then the received signal at the BS can be written as

$$\bar{\mathbf{x}} = \mathbf{h}_{T1} * \bar{\mathbf{c}}_{o1} + \mathbf{h}_{T2} * \bar{\mathbf{c}}_2 + \bar{\mathbf{w}} = \bar{\mathcal{H}}_1\bar{\mathbf{c}}_{o1} + \bar{\mathcal{H}}_2\bar{\mathbf{c}}_2 + \bar{\mathbf{w}} \ , \tag{3.24}$$

where $*$ denotes the convolution operation and $\bar{\mathbf{w}}$ is the noise vector with its element following the distribution $\bar{w}(i) \sim \mathcal{CN}(0, \sigma^2)$.

At the BS receiver, due to different baseband configurations and symbol duration, the processing of the received two slice signals also varies. Specifically, $\bar{\mathbf{x}}$ contains O symbols for slice1 and only 1 symbol for slice2. To detect the signal on the first slice, the received signal will be split into O non-overlapping L_1 length symbols (as shown in Fig. 3.2), and each of them can be processed following the normal receiver procedure of filtered OFDM. Let us define $\bar{\mathbf{x}}_k$ as the $(kL_1 + 1)$-th to $(k + 1)L_1$-th element of $\bar{\mathbf{x}}$. Then the signal (before channel equalization) of the k-th symbol of the first UE can be written as

$$\bar{\mathbf{y}}_{1,k} = \tilde{\mathbf{F}}_{N_{B1}}^H \mathbf{\Psi}_1^H \mathbf{R}_1 \mathcal{G}_1^H \bar{\mathbf{x}}_k \ , \text{for} \quad k = 0, \cdots, O-1 \ , \tag{3.25}$$

where $\mathbf{R}_1$ and $\mathcal{G}_1^H$ are the CP removal and matched filter matrices[4] with corresponding dimension, respectively.

For the second slice assigned to the second UE, the length of $\bar{\mathbf{x}}$ is the same as UE 2's symbol. After the subband filtering, CP removal, and DFT, the signal of the second slice before channel equalization can be written as

$$\bar{\mathbf{y}}_2 = \tilde{\mathbf{F}}_{N_{B2}}^H \mathbf{\Psi}_2^H \bar{\mathbf{R}}_2 \mathcal{G}_2^H \bar{\mathbf{x}} \ , \tag{3.26}$$

where $\bar{\mathbf{R}}_2 = [\mathbf{0}_{N_{B2}\times QL_{CP,2}}, \mathbf{I}_{N_{B2}}]$ is the matrix for CP removal. Note that the CP length (in samples) at the BS is Q times the size as that of the UE due to the sampling rate mismatch. $\tilde{\mathbf{F}}_{N_{B2}}^H \in \mathbb{C}^{M_2\times N_{B2}}$ is a sub-matrix of normalized N_{B2}-point DFT matrix $\mathbf{F}_{N_{B2}}^H$ by taking its first M_2 rows.

---

[4] One should note that arbitrary subband filters can be adopted at the receiver beside the matched filter. Especially to align the 3GPP standardization that waveform should be transparent [143]. However, without loss generality, matched filters are used here to make the expression compact and the extension is straightforward.

3.4.2 One-tap Channel Equalization

By using the generalized circular convolution property in Theorem 1, it is proved in Appendix. D that the slice1 and 2 signals can be expressed as

$$\bar{\mathbf{y}}_{1,k} = \mathbf{H}_{eff,1}\mathbf{a}_1(k) + \bar{\mathbf{v}}_{1,k} + \bar{\mathbf{w}}_{1,k} \ , \quad k = 0, \cdots, O-1 \tag{3.27}$$

and

$$\bar{\mathbf{y}}_2 = \mathbf{H}_{eff,2}\mathbf{\Lambda}_0\mathbf{a}_2 + \bar{\mathbf{v}}_2 + \bar{\mathbf{w}}_2 \ , \tag{3.28}$$

where the *diagonal* phase shifting matrix $\mathbf{\Lambda}_0 = \mathrm{diag}(\boldsymbol{\upsilon}_0)$. The *diagonal* matrices

$$\mathbf{H}_{eff,1} = \frac{1}{\sqrt{Q}}\mathbf{H}_1\mathbf{G}_1^H\mathbf{G}_1 \ \text{ and } \ \mathbf{H}_{eff,2} = \frac{1}{\sqrt{Q}}\mathbf{H}_2\mathbf{G}_2^H\mathbf{G}_2 \tag{3.29}$$

are the effective channels by taking the subband filters into account. $\mathbf{H}_1 = \sqrt{N_{B1}}\mathrm{diag}[\tilde{\mathbf{F}}_{N_{B1}}^H\mathbf{\Psi}_1^H\mathbf{h}_1]$ and $\mathbf{H}_2 = \sqrt{N_{B2}}\mathrm{diag}[\tilde{\mathbf{F}}_{N_{B2}}^H\mathbf{\Psi}_2^H\mathbf{h}_2]$ are the frequency channel responses at the respective subcarriers. $\mathbf{G}_1 = \sqrt{N_{B1}}\mathrm{diag}[\tilde{\mathbf{F}}_{N_{B1}}^H\mathbf{g}_{T1,p}]$ and $\mathbf{G}_2 = \sqrt{N_{B2}}\mathrm{diag}[\tilde{\mathbf{F}}_{N_{B2}}^H\mathbf{g}_{T2,p}]$ are the frequency filter responses at the respective subcarriers.

$\bar{\mathbf{v}}_{1,k} = \tilde{\mathbf{F}}_{N_{B1}}^H\mathbf{\Psi}_1^H\mathbf{R}_1\mathcal{G}_1^H\bar{\mathcal{H}}_{2,k}\bar{\mathbf{c}}_2$ is INI on the k-th symbol of slice1 from slice 2, where $\bar{\mathcal{H}}_{2,k}$ is a sub-matrix of $\bar{\mathcal{H}}_2$ obtained by taking its (kL_1+1)-th to $(k+1)L_1$-th rows. On the other hand, $\bar{\mathbf{v}}_2 = \tilde{\mathbf{F}}_{N_{B2}}^H\mathbf{\Psi}_2^H\bar{\mathbf{R}}_2\mathcal{G}_2^H\bar{\mathcal{H}}_1\bar{\mathbf{c}}_1$ is INI from slice1 to slice2. $\bar{\mathbf{w}}_{1,k} = \tilde{\mathbf{F}}_{N_{B1}}^H\mathbf{\Psi}_1^H\mathbf{R}_1\mathcal{G}_1^H\bar{\mathbf{w}}_k$ and $\bar{\mathbf{w}}_2 = \tilde{\mathbf{F}}_{N_{B2}}^H\mathbf{\Psi}_2^H\bar{\mathbf{R}}_2\mathcal{G}_2^H\bar{\mathbf{w}}$ are the noise after DFT and receiver filtering process at slices 1 and 2, respectively.

3.4.3 Signal Distortion Analysis and Proposed Power Compensation Algorithm

By using $\mathcal{E}\{\mathbf{H}_1\mathbf{H}_1^H\} = \rho_1^2\mathbf{I}_{M1}$ and $\mathcal{E}\{\mathbf{H}_2\mathbf{H}_2^H\} = \rho_2^2\mathbf{I}_{M2}$, it is easy to obtain the desired signal power gain at each subcarrier as

$$\bar{\boldsymbol{\alpha}}_1 = \mathcal{E}\{\mathrm{diag}|\mathbf{H}_{eff,1}|^2\} = \frac{\rho_1^2}{Q}\mathrm{diag}|\mathbf{G}_1^H\mathbf{G}_1|^2 \tag{3.30}$$

and

$$\bar{\boldsymbol{\alpha}}_2 = \mathcal{E}\{\mathrm{diag}|\mathbf{H}_{eff,2}\mathbf{\Lambda}_0|^2\} = \frac{\rho_2^2}{Q}\mathrm{diag}|\mathbf{G}_2^H\mathbf{G}_2\mathbf{\Lambda}_0|^2 \ . \tag{3.31}$$

Thanks to the generalized circular convolution property in Theorem 1, equations Eq. (3.27) and Eq. (3.28) reveal that one-tap channel equalization is still applicable in the DBDR scenario without generating extra ICI. However, unlike the OFDM system, the subband filtering operation at F-OFDM system and sampling rate mismatch may introduce the signal distortion among the subcarriers in both slices. Taking slice2 as an example, the filter gain $|\mathbf{G}_2^H\mathbf{G}_2\boldsymbol{\Lambda}_0|^2$ at each subcarrier may be different, and typically, the power at the edge subcarriers is smaller than the ones in the middle as a side effect of INI rejection, as shown in Fig. 3.4a. In addition, a phase shift Λ_0 at slice2 may further introduce the power distribution imbalance among the subcarriers. According to equation Eq. (3.14), the power at each subcarrier is shown in Fig. 3.4b with different Q. Larger mismatch factor Q leads to slightly larger frequency selectivity. The combined effect of both filter and phase shift is shown in red in Fig. 3.4b.

The noise power at the two slices can be expressed as

$$\bar{\boldsymbol{\beta}}_1 = \mathcal{E}\{\text{diag}(\bar{\mathbf{w}}_{1,k}\bar{\mathbf{w}}_{1,k}^H)\} = \frac{\sigma^2}{Q}\text{diag}|\mathbf{G}_1^H\mathbf{G}_1| \tag{3.32}$$

and

$$\bar{\boldsymbol{\beta}}_2 = \mathcal{E}\{\text{diag}(\bar{\mathbf{w}}_2\bar{\mathbf{w}}_2^H)\} = \frac{\sigma^2}{Q}\text{diag}|\mathbf{G}_2^H\mathbf{G}_2| \ . \tag{3.33}$$

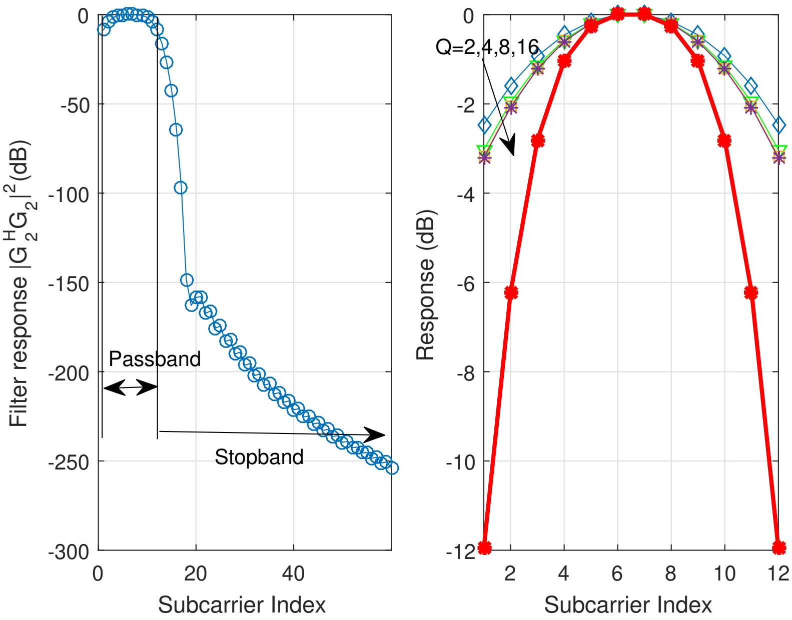

Figure 3.4: Filter and phase shift frequency responses versus subcarrier index ($M_2 = 12$): a) Filter frequency response $\text{diag}|\mathbf{G}_2^H\mathbf{G}_2|^2$ (F-OFDM system [82]); b), Phase shift $\text{diag}|\boldsymbol{\Lambda}_0|^2$ response with $Q = 2, 4, 8, 16$, and joint response $\text{diag}|\mathbf{G}_2^H\mathbf{G}_2\boldsymbol{\Lambda}_0|^2$ (in red, where we consider $Q = 16$.).

According to Eq. (3.30), Eq. (3.31), Eq. (3.32) and Eq. (3.33), filtering causes both desired signal and noise selectivity, which mitigates the overall selectivity in terms of the signal to noise ratio (SNR). The selectivity among the subcarriers could be very significant and leads to inefficient power allocation since some subcarriers receive more gain than the others, as shown in Fig. 3.4. To further improve the performance via equal output $\bar{\mathbf{SNR}}_i$ at the receiver, power pre-compensation algorithms are proposed at the transmitter side to pre-cancel the gain differences. Specifically, the unified precoding matrices can be expressed as

$$\begin{aligned}\bar{\mathbf{E}}_1 &= \vartheta\Big[\sqrt{\frac{M_1}{\mathrm{trace}[(\mathbf{G}_1\mathbf{G}_1^H)^{-1}]}}|\mathbf{G}_1|^{-1} - \mathbf{I}_{M_1}\Big] + \mathbf{I}_{M_1}\\ \bar{\mathbf{E}}_2 &= \vartheta\Big[\sqrt{\frac{M_2}{\mathrm{trace}[(\mathbf{G}_2\mathbf{G}_2^H\mathbf{\Lambda}_0\mathbf{\Lambda}_0^H)^{-1}]}}|\mathbf{G}_2\mathbf{\Lambda}_0|^{-1} - \mathbf{I}_{M_2}\Big] + \mathbf{I}_{M_2},\end{aligned} \tag{3.34}$$

where $\vartheta = 1$ and $\vartheta = 0$ refer to with and without power compensation, respectively. Hence, $\bar{\mathbf{E}}_1\mathbf{a}_1$ and $\bar{\mathbf{E}}_2\mathbf{a}_2$ are transmitted instead of $\mathbf{a}_1$ and $\mathbf{a}_2$.

3.4.4 INI Analysis and Cancellation for SBDR Scenario

With the symbol duration difference in the DBDR scenario, it is complex to analyze INI, and hence, the DBDR INI analysis will be omitted here. Besides, INI expressions for DBSR is derived in detail in [34]. In this subsection, the DBDR system is degraded to the SBDR system by taking $O = 1$. An example of the SBDR system is the NB-IoT, where the same subcarrier spacing and symbol duration are used for both LTE and IoT slices. However, IoT may use significantly smaller RF bandwidth than the normal LTE system to save cost/complexity/energy consumption. Next, INI expressions are derived and a collaboration based INI cancellation algorithm is proposed at the BS side to guide the system design.

By taking $O = 1$, the symbol duration and DFT size of the two slices are the same, *i.e.*, $\Delta T_1 = \Delta T_2$ and $N_{B1} = N_{B2}$. Besides, $\bar{\mathbf{c}}_{o1} = \bar{\mathbf{c}}_1$, $\bar{\mathbf{v}}_{1,k} = \bar{\mathbf{v}}_1$, $\bar{\mathbf{w}}_{1,k} = \bar{\mathbf{w}}_1$ for $k = 0, 1, \cdots, Q-1$. By using the generalized circular convolution property of Theorem 1, INI terms can be rewritten as

$$\bar{\mathbf{v}}_1 = \frac{1}{\sqrt{Q}}\tilde{\mathbf{H}}_2\mathbf{G}_1^H\mathbf{G}_{2\to 1}\mathbf{\Lambda}_I\bar{\mathbf{E}}_2\mathbf{a}_2\ , \tag{3.35}$$

$$\bar{\mathbf{v}}_2 = \mathbf{0}\ , \tag{3.36}$$

where $\tilde{\mathbf{H}}_2 = \sqrt{N_{B1}}\text{diag}[\tilde{\mathbf{F}}_{N_{B1}}^H \mathbf{\Psi}_1^H \mathbf{h}_2]$ is the frequency channel response of $\mathbf{h}_2$ at the first slice's passband. $\mathbf{G}_{2\to1} = \sqrt{N_{B1}}\text{diag}[\tilde{\mathbf{F}}_{N_{B1}}^H \mathbf{\Psi}_1^H \mathbf{g}_{T2}]$ is the frequency domain response of the *second* slice's filter $\mathbf{g}_{T2}$ at the *first* slice's frequency band. $\mathbf{\Lambda}_I \in \mathbb{C}^{M_1\times M_2}$ is the exchange matrix by taking the $(\eta_1 + 1)$-th to the $(\eta_1 + M_1)$-th columns and rows of $\mathbf{\Theta\Lambda}$.

Equations Eq. (3.35) and Eq. (3.36) show that slice2 is free of the interference from slice1. The reason is simple, the signal at slice1 is transmitted and processed with matched sampling rate at the BS, which enforces the orthogonality among slices. However, slice2 with mismatched sampling rate at transmitter and receiver will generate INI to slice1. By noting the fact that each row in $\mathbf{\Lambda}_I$ has only one non-zero element, the interference is also expressed as a multiplication between the channel, filter response and signal $\mathbf{a}_2$. According to Fig. 3.4 a, the interference level will be significantly reduced since $\mathbf{G}_{2\to1}$ is located in the filter stopband.

The interference power at the subcarriers of slice2 can be derived as

$$\boldsymbol{\gamma}_1 = \text{diag}\{\mathcal{E}[\bar{\mathbf{v}}_1\bar{\mathbf{v}}_1^H]\} = \frac{\rho_2^2}{Q}|\mathbf{G}_1^H\mathbf{G}_{2\to1}|^2\tilde{\mathbf{\Lambda}}_I \; . \tag{3.37}$$

One should note that $\tilde{\mathbf{\Lambda}}_I = \mathbf{\Lambda}_I\bar{\mathbf{E}}_2\bar{\mathbf{E}}_2^H\mathbf{\Lambda}_I^H$ is an M_1-dimensional diagonal matrix. The interference level depends on the guardband between the two slices. Larger ΔB_1 can mitigate INI power $\boldsymbol{\gamma}_1$ since it pushes $\mathbf{G}_{2\to1}$ far away from the filter passband, as shown in Fig. 3.4a. By using equations Eq. (3.30), Eq. (3.31), Eq. (3.32), Eq. (3.33) and Eq. (3.37), we can write the channel ergodic output SINR at the two slices as

$$\begin{aligned} \bar{\mathbf{SINR}}_1 &= \frac{\rho_1^2|\mathbf{G}_1\mathbf{G}_1^H\bar{\mathbf{E}}_1|^2}{\rho_2^2|\mathbf{G}_1^H\mathbf{G}_{2\to1}|^2\tilde{\mathbf{\Lambda}}_I + \sigma^2|\mathbf{G}_1\mathbf{G}_1^H|} \\ \bar{\mathbf{SINR}}_2 &= \bar{\mathbf{SNR}}_2 = \frac{\rho_2^2}{\sigma^2}|\mathbf{G}_2^H\mathbf{G}_2\bar{\mathbf{E}}_2|^2 \; . \end{aligned} \tag{3.38}$$

With limited guardband between slice1 and 2, the interference $\boldsymbol{\gamma}_1$, especially at the edge of the slice's band, could be significant. With the given framework on the system model in Eq. (3.27), Eq. (3.28), Eq. (3.35), and Eq. (3.36), we can easily propose a low complexity but effective INI cancellation algorithm at the BS. Specifically, we can detect the interference free symbols at slice2 as the first step, for the interfered signal in slice1, we can subtract the interference $\bar{\mathbf{v}}_1$ Eq. (3.35) from the received signal $\bar{\mathbf{y}}_1$ in Eq. (3.27), *i.e.*,

$$\bar{\bar{\mathbf{y}}}_1 = \bar{\mathbf{y}}_1 - \bar{\mathbf{v}}_1 \; . \tag{3.39}$$

It is worth to mention that each subcarrier (*e.g.*, each element in $\bar{\bar{\mathbf{y}}}_1$) is only affected by one subcarrier in slice2 (*e.g.*, one element of $\mathbf{a}_2$), since only one element in each row of $\mathbf{\Lambda}_I$ is non-zero. Based on this property, one can propose more complex and advanced INI cancellation algorithms. Besides, although there are other interference cancellation methods for the mixed-numerology system, they are either based on overlapping multiplexing model, *e.g.*, [32] or with different assumptions of numerology configurations with this thesis, *e.g.*, [83]. Hence, the performance of the interference cancellation method in this chapter is not comparable with the ones in other researches.

3.5 Downlink Mixed-Numerology System

3.5.1 DBDR System Model, Equalization, and Power Compensation Algorithm

Due to the non-reciprocity of the uplink and downlink transmission in the physical layer MN system, it is necessary to separately derive the downlink system model, equalizer, interference analysis and interference cancellation algorithm.

At the transmitter side (*i.e.*, BS), the signal in the i-th service/slice after IDFT, CP insertion and subband filtering can be written in matrix form as:

$$\hat{\mathbf{c}}_1 = \mathcal{G}_1^H \mathbf{C}_1 \mathbf{\Psi}_1 \tilde{\mathbf{F}}_{N_{B1}} \mathbf{a}_1 \ ; \quad \hat{\mathbf{c}}_2 = \mathcal{G}_2^H \hat{\mathbf{C}}_2 \mathbf{\Psi}_2 \tilde{\mathbf{F}}_{N_{B2}} \mathbf{a}_2 \ , \tag{3.40}$$

where $\hat{\mathbf{C}}_2 = [\mathbf{0}_{QL_{CP,2} \times (N_{B2} - QL_{CP,2})}, \mathbf{I}_{QL_{CP,2}}; \mathbf{I}_{N_{B2}}] \in \mathbb{R}^{L_2 \times N_{B2}}$ is the CP insertion matrix.

Similar to the uplink transmission, we have to consider O consecutive symbols as $\hat{\mathbf{c}}_{o1} = [\hat{\mathbf{c}}_1(0), \hat{\mathbf{c}}_1(1), \cdots, \hat{\mathbf{c}}_1(O-1)]^T$. The signal in one LCM symbol [34] before transmission over the channel can be written as

$$\hat{\mathbf{x}} = \hat{\mathbf{c}}_{o1} + \hat{\mathbf{c}}_2 \ . \tag{3.41}$$

At the receiver, two UEs follow different receiver processing due to different baseband and RF configurations. Specifically, at UE 1, the received signal $\mathbf{y}_1$ is split into O non-overlapping symbols, and each segment has L_1 samples. Let us define $\hat{\mathbf{x}}_k$ as the (kL_1+1)-th to $(k+1)L_1$-th element of $\hat{\mathbf{x}}$. Then the signal (before channel equalization) of the k-th symbol for $k = 0, 1, \cdots, O-1$ of the first UE can be written as

$$\hat{\mathbf{y}}_{1,k} = \tilde{\mathbf{F}}_{N_{U1}}^H \mathbf{\Psi}_1^H \mathbf{R}_1 \mathcal{G}_1 (\hat{\mathcal{H}}_1 \hat{\mathbf{x}}_k + \hat{\mathbf{w}}_{1,k}) \ , \tag{3.42}$$

where $\mathbf{R}_1$, $\mathcal{G}_1$ and $\hat{\mathcal{H}}_1$ are the CP removal, matched filter and channel matrices, respectively, $\hat{\mathbf{w}}_{1,k}$ is the noise vector with its element being zero-mean and σ^2 variance Gaussian variables.

The second UE assigned within the second slice has a lower RF sampling rate; the signal will be down-sampled by a factor of Q, phase shifted, and follows a filtered OFDM processing [128]. The signal of the second UE (before channel equalization) can be written as:

$$\hat{\mathbf{y}}_2 = \mathbf{F}_{N_{U2}}^H \mathbf{\Psi}_2^H \hat{\mathbf{R}}_2 \mathbf{D}_Q \mathcal{G}_2 (\hat{\mathcal{H}}_2 \hat{\mathbf{x}} + \hat{\mathbf{w}}_2) \ , \tag{3.43}$$

where $\mathbf{D}_Q$ is the down-sampling matrix by a factor of Q, as defined in Theorem 2. $\hat{\mathbf{R}}_2$ is the CP removal matrix with the correct dimension. $\hat{\mathbf{w}}_2$ is the noise vector with its element being zero-mean and σ^2/Q variance Gaussian variables[5].

Using the circular convolution property in Theorem 2 and following derivations in the uplink transmission, we can rewrite Eq. (3.42) as:

$$\hat{\mathbf{y}}_{1,k} = \mathbf{H}_{eff,1} \mathbf{a}_1(k) + \hat{\mathbf{v}}_{1,k} + \tilde{\mathbf{w}}_{1,k} \ , \tag{3.44}$$

where $\mathbf{a}_1(k)$ is the k-th symbol of $\mathbf{a}_1$ in slice1. $\hat{\mathbf{v}}_{1,k} = \tilde{\mathbf{F}}_{N_{U1}}^H \mathbf{\Psi}_1^H \mathbf{R}_1 \mathcal{G}_1 \hat{\mathcal{H}}_{2,k} \hat{\mathbf{c}}_2$ and $\tilde{\mathbf{w}}_{1,k} = \tilde{\mathbf{F}}_{N_{U1}}^H \mathbf{\Psi}_1^H \mathbf{R}_1 \mathcal{G}_1 \hat{\mathcal{H}}_1 \hat{\mathbf{w}}_{1,k}$ are the interference from the second slice and noise after DFT operation, respectively. $\hat{\mathcal{H}}_{2,k}$ is a sub-matrix of $\hat{\mathcal{H}}_2$ obtained by taking its (kL_1+1)-th to $(k+1)L_1$-th rows. The noise power has the same expression as the uplink *i.e.*, $\hat{\boldsymbol{\beta}}_1 = \bar{\boldsymbol{\beta}}_1$. The first term $\mathbf{H}_{eff,1}\mathbf{a}_1(k)$ is the desired signal and it can be seen that the signal can be written as a multiplication with the filter and channel frequency response. Thus, one-tap channel equalization can be performed.

For the second UE, by using Theorem 2 in Eq. (3.19) and similar to the UE 1, we can rewrite equation Eq. (3.43) as:

$$\hat{\mathbf{y}}_2 = \mathbf{H}_{eff,2} \mathbf{a}_2 + \hat{\mathbf{v}}_2 + \tilde{\mathbf{w}}_2 \ , \tag{3.45}$$

where $\hat{\mathbf{v}}_2 = \mathbf{F}_{N_{U2}}^H \mathbf{\Psi}_2^H \hat{\mathbf{R}}_2 \mathbf{D}_Q \mathcal{G}_2 \bar{\mathcal{H}}_1 \hat{\mathbf{c}}_1$ and $\tilde{\mathbf{w}}_2 = \mathbf{F}_{N_{U2}}^H \mathbf{\Psi}_2^H \hat{\mathbf{R}}_2 \mathbf{\Psi} \mathbf{D}_Q \mathcal{G}_2 \hat{\mathbf{w}}_2$ are interference from the first slice and noise after DFT operation, respectively. The noise power has the same expression as the uplink, *i.e.*, $\hat{\boldsymbol{\beta}}_2 = \bar{\boldsymbol{\beta}}_2$.

Similar to the uplink case, the power pre-equalization at the transmitter can be proposed to improve the performance of the two slices. Specifically, $\hat{\mathbf{E}}_1\mathbf{a}_1(k)$

---

[5] Note that due to the reduced processing bandwidth, the equivalent noise power is also reduced accordingly.

and $\hat{\mathbf{E}}_2\mathbf{a}_2$ can be transmitted at the slices 1 and 2 respectively, where

$$\hat{\mathbf{E}}_i = \vartheta\Big[\sqrt{\frac{M_i}{\mathrm{trace}[(\mathbf{G}_i\mathbf{G}_i^H)^{-1}]}}|\mathbf{G}_i|^{-1} - \mathbf{I}_{M_i}\Big] + \mathbf{I}_{M_i} \tag{3.46}$$

for $i = 1$ or 2. $\vartheta = 1$ when the proposed power compensation scheme is considered, otherwise $\vartheta = 0$. Hence, $\tilde{\mathbf{E}}_i\mathbf{a}_i$ instead of $\mathbf{a}_i$ will be transmitted.

3.5.2 SBDR INI Analysis and Cancellation

Following the uplink case, the downlink DBDR system is degraded into the SBDR system. By taking $O = 1$, we have $\hat{\mathbf{c}}_{o1} = \hat{\mathbf{c}}_1$, $\hat{\mathbf{v}}_1(i) = \hat{\mathbf{v}}_1$, and $N_{B1} = N_{B2}$. Also considering the power compensation matrix $\hat{\mathbf{E}}_i$ at the transmitter, and using the generalized circular convolution property in Theorem 2, INI terms can be rewritten as

$$\hat{\mathbf{v}}_1 = \mathbf{0}\ ;\ \ \hat{\mathbf{v}}_2 = \frac{1}{\sqrt{Q}}\tilde{\check{\boldsymbol{\Lambda}}}\tilde{\mathbf{H}}_2\mathbf{G}_2^H\mathbf{G}_{1\to 2}\hat{\mathbf{E}}_1\mathbf{a}_1\ , \tag{3.47}$$

where $\mathbf{G}_{1\to 2} = \sqrt{N_{B2}}\mathrm{diag}[\tilde{\mathbf{F}}_{N_{B2}}^H\boldsymbol{\Psi}_2^H\mathbf{g}_{T1}]$ is the frequency domain response of the *first* slice's filter at the *second* slice's band. $\tilde{\check{\boldsymbol{\Lambda}}}$ is a sub-matrix obtained by taking the η_2-th to $(\eta_2 + M_2)$-th columns of $\check{\boldsymbol{\Lambda}}$.

Unlike uplink transmission, where slice2 is interference free, equation Eq. (3.47) shows that slice1 is free of the interference from slice2 in the downlink transmission. However, slice2 has mismatched sampling rates at transmitter and receiver, will receive INI from slice1. The interference power at the subcarriers on slice2 can be derived as

$$\hat{\boldsymbol{\gamma}}_2 = \frac{\rho_2^2}{Q}\mathrm{diag}|\tilde{\check{\boldsymbol{\Lambda}}}\mathbf{G}_2^H\mathbf{G}_{1\to 2}\hat{\mathbf{E}}_1|^2\ . \tag{3.48}$$

Furthermore, the SINR at two slices can be expressed in vector form as

$$\begin{aligned}
\hat{\mathbf{SINR}}_1 &= \frac{\rho_1^2}{\sigma^2}|\mathbf{G}_1^H\mathbf{G}_1\hat{\mathbf{E}}_1|^2\ ,\\
\hat{\mathbf{SINR}}_2 &= \frac{\rho_2^2|\mathbf{G}_2\mathbf{G}_2^H\hat{\mathbf{E}}_2|^2}{\rho_2^2\mathrm{diag}|\tilde{\check{\boldsymbol{\Lambda}}}\mathbf{G}_2^H\mathbf{G}_{1\to 2}\hat{\mathbf{E}}_1|^2 + \sigma^2|\mathbf{G}_2\mathbf{G}_2^H|}\ .
\end{aligned} \tag{3.49}$$

With the established signal models in equations Eq. (3.44), Eq. (3.45) and Eq. (3.47), we can propose a low complexity precoding algorithm at the BS to cancel INI on slice2. Specifically, a precoding matrix $\mathbf{P}_{pre}$ is introduced to the collaboration signal model by considering both slice1 and slice2 signals as follows

$$\hat{\mathbf{y}}_{all} = \begin{pmatrix} \mathbf{H}_1 & \mathbf{0} \\ \mathbf{0} & \mathbf{H}_2 \end{pmatrix} \cdot \underbrace{\begin{pmatrix} \hat{\mathbf{Z}}_{11} & \mathbf{0} \\ \hat{\mathbf{Z}}_{21} & \hat{\mathbf{Z}}_{22} \end{pmatrix}}_{\hat{\mathbf{Z}}} \mathbf{P}_{pre} \begin{pmatrix} \hat{\mathbf{E}}_1 \mathbf{a}_1 \\ \hat{\mathbf{E}}_2 \mathbf{a}_2 \end{pmatrix} + \begin{pmatrix} \mathbf{w}_1 \\ \mathbf{w}_2 \end{pmatrix} , \tag{3.50}$$

where $\hat{\mathbf{Z}}_{11} = \mathbf{I}_{M_1}$, $\hat{\mathbf{Z}}_{21} = \tilde{\hat{\mathbf{\Lambda}}}\mathbf{G}_2^H \mathbf{G}_{1\to 2}$, $\hat{\mathbf{Z}}_{22} = \mathbf{I}_{M_2}$. Note that here it is assumed that $\mathbf{H}_2 = \tilde{\mathbf{H}}_2$ due to the fact that the interference is only generated within a very small adjacent bandwidth [34], thus, we can assume it is within the coherent bandwidth. Therefore, we can precancel INI based on the channel independent mixture matrix $\hat{\mathbf{Z}}$ only by the following zero-forcing (ZF) criterion

$$\mathbf{P}_{pre} = (\hat{\mathbf{Z}})^{-1} . \tag{3.51}$$

Nevertheless, one can design a global optimal $\mathbf{P}_{pre}$ by taking both channel and mixture matrix into consideration, but at the cost of increased computation and system overhead.

3.6 Numerical Results

In this section, the effectiveness of the established MN system models, the proposed power compensation algorithms and INI cancellation algorithms for both uplink and downlink transmissions are verified. Both OFDM and F-OFDM waveforms are considered for comparison purposes. F-OFDM waveform with a matched filter at the receiver is considered for all simulations with windowed Sinc filter, and the filter length equals to half of the DFT size [82]. The first and the second UEs are allocated with 20% and 5% of the full bandwidth, *i.e.*, $B_1 = 0.2$ and $B_2 = 0.05$, respectively. Each slice contains 20 subcarriers. Thus, the subcarrier spacing for the two services satisfies $\Delta f_1 = 4\Delta f_2$. In addition, it is assumed the RF up/down-sampling factor in UE 2 is 20, *i.e.*, the sampling rate at UE 2 is only 5% of the one used at the BS. The CP overhead is 10% for both slices and for both waveforms. For the special case SBDR, the two slices have the same symbol duration and subcarrier spacing, and it is assumed both slices occupy 5% of the full bandwidth. Considering the nature of the use cases, the modulation scheme for slices 1 and 2 are 16-QAM (quadrature amplitude modulation) and QPSK (quadrature phase shift keying), respectively. LTE extended pedestrian A (EPA) channel is used unless otherwise specified. The minimum mean square error (MMSE) based one-tap channel equalizer is adopted for all cases. For the numerical results in this section, each point was achieved by at least 10000 simulation realizations. Note that waveform, slice number and algorithm combinations are used as figure legend to make it more compact, *e.g.*, F-OFDM$_1$+ (3.34) means the performance at slice1 with the proposed power pre-compensation algorithm in equation Eq. (3.34) based on the F-OFDM waveform.

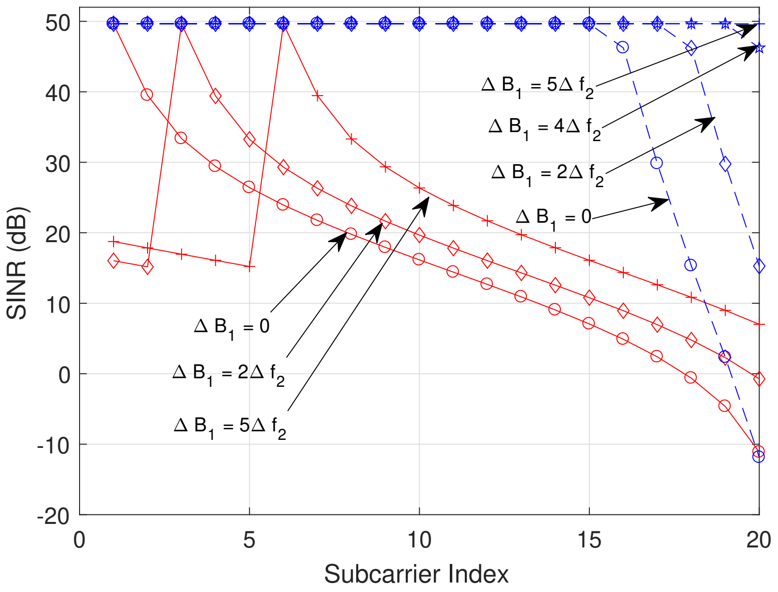

Figure 3.5: SINR versus subcarrier index with different guard band ΔB_1 for both F-OFDM and OFDM waveforms for uplink transmission (Red lines are for OFDM and blue dashed lines are for F-OFDM).

Firstly, the interference in the SBDR system caused by RF numerology mismatches is investigate. Fig. 3.5 shows the output signal SINR versus the subcarrier index for slice 1 in uplink transmission, with different values of guardband ΔB_1 between slices, for both F-OFDM and OFDM systems. it is assumed the symbol input SNR is 50 dB to make the system interference limited. The power compensation algorithm in Eq. (3.34) is applied, but INI cancellation algorithm in Eq. (3.39) is not considered to show the interference distribution among subcarriers. It can be seen that the two waveforms have totally different SINR distributions. Specifically, with a given guardband, F-OFDM (shown with blue dashed lines) based system shows significantly higher SINR than its counterpart (*i.e.*, OFDM, shown with red lines). This verifies that the F-OFDM system can mitigate INI by the subband filtering. It is interesting to notice that there is a valley and a peak in each red curve. The former indicates that at least one subcarrier of slice1 suffers from the most severe INI compared to the other subcarriers; while the latter implies the existence of a INI-free subcarrier (more detailed analysis about INI-free subcarriers can be found in Chapter 4).

In addition, it can be observed that the interference in the OFDM based MN system moved to the right with guardband ΔB_1 increasing, which is because of the exchange matrix $\boldsymbol{\Theta}$ as analyzed in Theorem 1. However, the interference in the F-OFDM system is much smaller and SINR reduces sharply with ΔB_1 decreasing. It can also be observed that having 4 or 5 subcarriers as guardband between the two slices is sufficient to achieve negligible performance loss in terms of output SINR. One should also note that significant SINR reduction can be observed at the larger subcarrier index region, which is because this region is closer to the second slice's frequency band, and it receives much more interference than in the low subcarrier index.

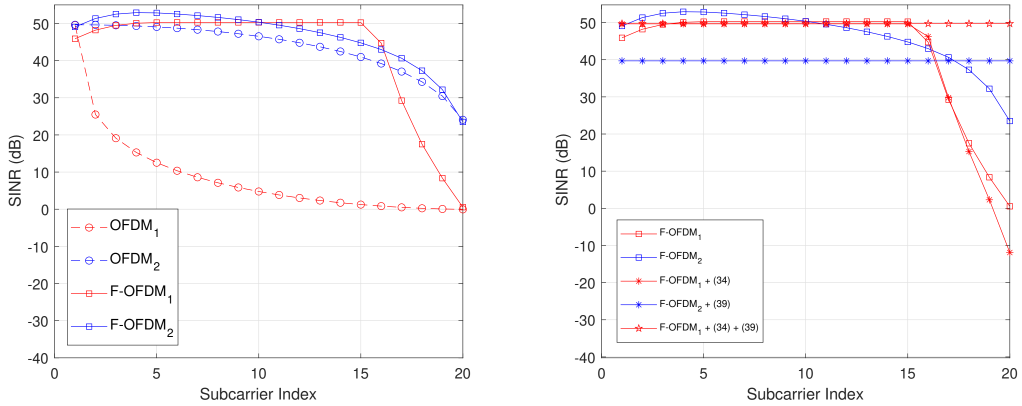

(a) F-OFDM versus OFDM without proposed algorithms

(b) F-OFDM with proposed algorithms

Figure 3.6: SINR versus subcarrier index with and without proposed algorithms for both F-OFDM and OFDM waveforms in uplink transmission (Red lines are for slice1 and blue lines are for slice2).

By taking both power compensation and INI cancellation schemes into consideration, Fig. 3.6 depicts the output SINR against the subcarrier index. The guardband is assumed to be $\Delta B_1 = 0$ to show the effectiveness of the proposed INI cancellation algorithm. For the purpose to improve the readability, two subfigures depict the SINR performance, where Fig. 3.6(a) illustrates the SINR of F-OFDM and OFDM waveforms without any of the proposed algorithms being applied, and Fig. 3.6(b) shows the performance improvements of the proposed algorithms. It can be seen from Fig. 3.6 that the power compensation for slice2 (and all F-OFDM based algorithm) is critical to remove the filter gain signal distortion. With the proposed power compensation expression Eq. (3.34), the SINR values among subcarriers become even.

However, it is also interesting to notice that the power compensation algorithm shows negligible improvement to the slice1 signal. This is because that for the slice2 signal in uplink transmission, the unevenly distributed signal power results from the combination of the phase shift matrix $\mathbf{\Lambda}_0$ and filter response $\mathbf{G}_2$ and $\mathbf{G}_2^H$, while only the filter responses $\mathbf{G}_1$ and $\mathbf{G}_1^H$ contribute to slice1's signal power distribution. It can be seen from Fig. 3.4 that the combined effect of the phase shift matrix and filter gain is stronger than the filter gain only effect. Therefore, after compensation, the performance improvement for the former case is higher than the later. On the other hand, in the uplink the slice1 signal suffers from interference, which further decreases the effectiveness of the power compensation algorithm. Considering the increased complexity due to the compensation algorithms, it might be a good choice to only implement the effective one in the system, *i.e.*, $\bar{\mathbf{E}}_2$ for slice2. The algorithm's performance in the downlink transmission can be explained following the same rationale. In addition, we can see from Fig. 3.6 that the proposed low complexity INI cancellation algorithm in Eq. (3.39) is effective since the SINR performance is significantly improved even without any guardband protection.

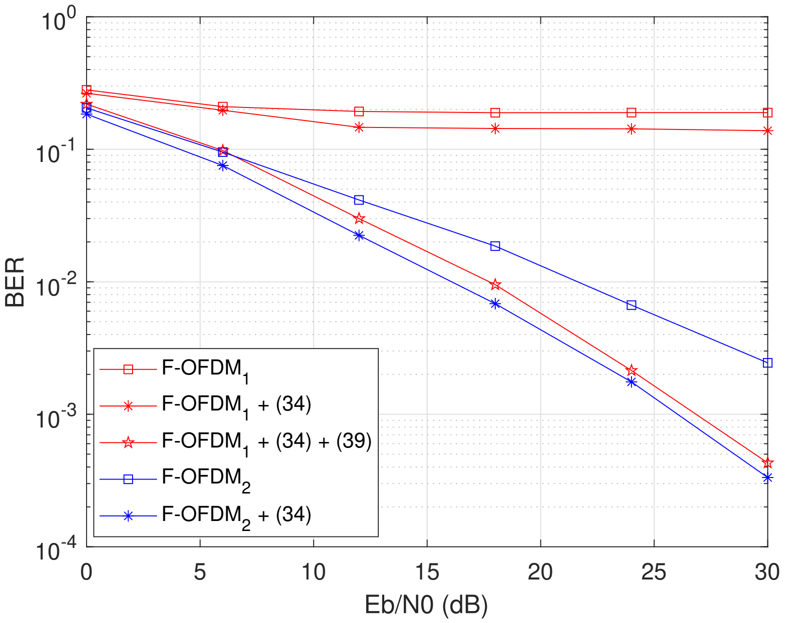

Figure 3.7: BER versus E_b/N_o with and without proposed algorithms for SBDR scenario in uplink transmission (Red lines are for slice1 and blue lines are for slice2).

The bit error rate (BER) performance in both slices for the SBDR scenario is shown in Fig. 3.7. The guardband between the slices is 0. Similar to the SINR performance, the curves show the effectiveness of the established system models and one-tap channel equalizer. In addition, the proposed power compensation and INI cancellation schemes can significantly improve the slice2 signal's BER performance.

For the downlink case, the SINR distribution among the subcarriers is investigated in slice2 for both OFDM and F-OFDM based SBDR MN system in Fig. 3.8. Similarly, the SINR performances under different configurations are illustrated in two subfigures for better readability. One should note that slice1 is free of interference, as shown in Eq. (3.47). Clearly, the OFDM based system cannot work properly due to the serious INI from slice1, which verifies Theorem 2 since the signal in slice1 expands to the whole baseband and the interference power is equal to the desired signal power. In addition, the signal distortion can be compensated from Eq. (3.46). Nevertheless, compared with the uplink case, signal distortion in the downlink is less severe. Finally, INI cancellation algorithm in Eq. (3.51) shows effectiveness since nearly the same SINR can be achieved as that in the interference free case.

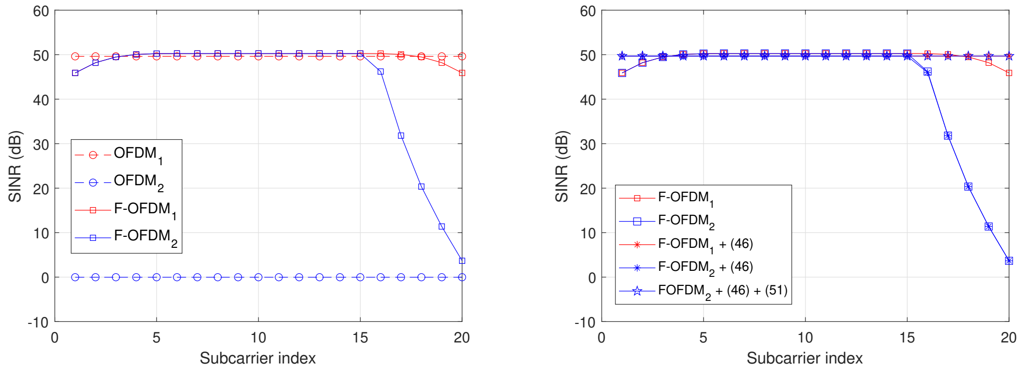

(a) F-OFDM versus OFDM without proposed algorithms

(b) F-OFDM with proposed algorithms

Figure 3.8: SINR versus subcarrier index with and without proposed algorithms for both F-OFDM and OFDM waveforms in downlink transmission (Red lines are for slice1 and blue lines are for slice2).

The SINR at slice2 with different guardband ΔB_1 is shown in Fig. 3.9 for the OFDM and F-OFDM based SBDR system. Similar to the uplink case, the minimum SINR in the F-OFDM system improves dramatically as ΔB_1 increases. Furthermore, having 4 or 5 subcarriers as guardband can achieve sufficiently high SINR. In terms of the BER performance, Fig. 3.10 shows the performance for the SBDR scenario based on the F-OFDM system in the downlink transmission. The guardband between the slices is 0. It can be seen that the proposed interference cancellation algorithm significantly improves the system performance in terms of BER.

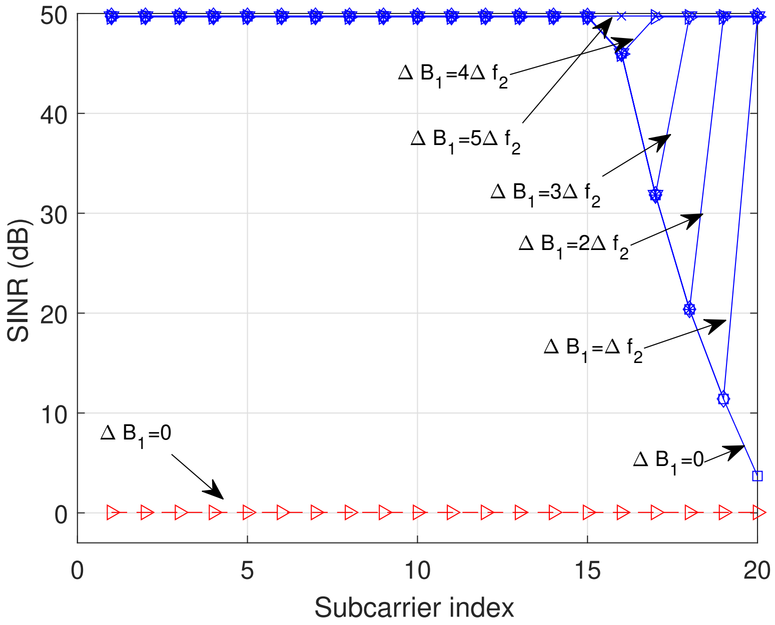

Figure 3.9: SINR versus subcarrier index in downlink transmission with different guardband (Red: OFDM, Blue: Proposed).

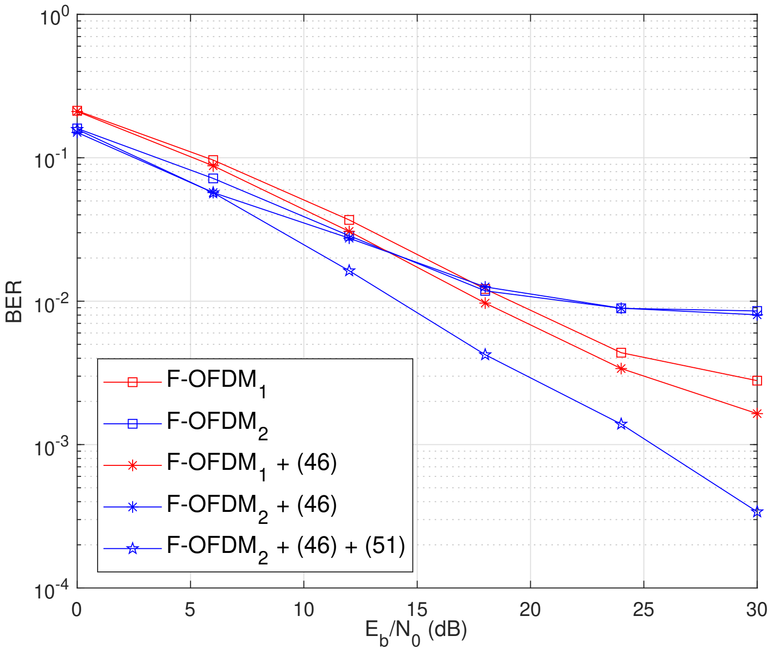

Figure 3.10: BER versus E_b/N_o with and without proposed algorithms for SBDR scenario in downlink transmission (Red lines are for slice1 and blue lines are for slice2).

3.7 Conclusions

This chapter establishes a framework for MN systems from the physical layer perspective. The numerology relationships among slices were defined mathematically by considering both RF and BB configuration imparities, according to which one can simply set up the parameter configurations for a desired multi-numerology system. Two theorems of generalized circular convolution properties were proposed, which build a theoretic foundation for signal isolation, collaboration and detection in such kind of systems. They also imply that the implementation of the low complexity one-tap channel equalization is feasible. Based on the derivations in this chapter, it is found that the interference generated from BB and RF imparities is linearly superposed in the receiver. Simulations were performed to verify the effectiveness of the proposed system model and algorithms. It is shown that in the F-OFDM based multi-numerology systems, 4-5 subcarriers' guardband between slices can reduce INI to a negligible level. Also, the proposed INI cancellation algorithms can significantly improve the SINR performance even without any guardband protection. The work presented in this chapter provides guidance for multi-numerology system design in terms of parameter and waveform selection, as well as the frame structure and algorithms design. Moreover, it presents a solution as to how the RAN slicing can be underpinned in the physical layer in a spectrum efficient way.

Chapter 4

Mixed-Numerology Channel Estimation and Pilot Design

4.1 Introduction

Chapter 3 presents a comprehensive framework for the mixed-numerology systems by considering both the baseband and radio frequency configuration imparities. Based on such a framework, this chapter focuses on channel estimation investigations for mixed-numerology systems.

In a single-numerology (SN) OFDM system such as LTE, the channel matrix could be diagonalized based on the original circular convolution property of DFT , which generates flat fading sub-channels and enables the low-complexity one-tap channel estimation/equalization [30]. Nevertheless, as has been investigated in Chapter 3, either SCS or sampling rate mismatch among numerologies could invalidate the O-CCP-DFT by destroying the OFDM system's orthogonality. The widely used algorithms and signal processing procedures, such as synchronization and channel equalization, could thus be significantly affected. In fact, channel estimation is always one of the most important parts of receiver processing in wireless communication systems. Without an accurate channel estimation, all signal detection algorithms could be invalidated. Unfortunately, both signal distortion and INI caused by the configuration mismatch could result in the degraded performance of traditional CE methods. If the current channel estimation cannot be adapted accordingly, the performance of mixed-numerology systems would reach the bottleneck no matter how much effort is put into the other transmitter/receiver algorithms. To the best of the author's knowledge, the study on channel estimation methods in mixed-numerology systems is in the initial stage. Related work such as [130] is based on the DBSR scenario, and fundamental analysis for the channel estimation is not included. There is no clue why and how the performance degradation may happen, not to mention the design of new algorithms.

Since DBSR scenario, i.e., BB-differed MN where only based SCS is different among numerologies, has been thoroughly investigated in the literature, the focus of this chapter is on the SBDR scenario or RF-differed MN system where only RF sampling rate is considered to differentiate numerologies. In addition, Chapter 3 implies that users of different numerologies in the SBDR scenario suffer from signal distortion as well as INI[1] in the uplink communications, while users in the downlink only suffer from the interference. As such, this chapter focuses on uplink (worse case) channel estimation study for an SBDR mixed-numerology system in terms of performance and the pilot signal design. Without loss of generality, a comb-type pilot pattern is considered, which provides better performance than the block-type pilot pattern in the presence of fast fading channels [144]. In addition, least-square (LS) and MMSE estimation methods are applied to estimate the channel gain of pilot subcarriers. The former holds a decent computational complexity but suffers from the error floor when noise is non-negligible. At the same time, the latter provides the minimum estimation mean square error (MSE); however, it requires knowledge of the channel and has very high complexity [145]. Besides, linear interpolation (LI) and DFT based '*sinc*' interpolation is applied to estimate the channel gain of non-pilot subcarriers. Compared to the linear interpolation realized directly in the frequency domain, the '*sinc*' interpolation is realized by zero-padding the estimated pilot channel in the time domain, and it brings about zero interpolation error [105, 146]. The main contributions of this chapter are summarized as follows:

- The differences between RF-differed numerologies are illustrated in the symbol level, and their relationships are represented mathematically. It provides us with a clear view of how the different RF configurations affect the signal structure;

- Two scenarios, *i.e.*, single-user scenario and multi-user scenario, are constructed to investigate the impact of the signal distortion and INI separately. Different combinations of estimation and interpolation methods, *i.e.*, least-square linear interpolation (denoted as LSLI), least-square '*sinc*' interpolation (denoted as LS-DFT), and minimum mean square error '*sinc*' interpolation (denoted as MMSE-DFT) are implemented in both scenarios with theoretical analyze.

---

[1] It should be noted that the INI in this chapter is caused by the RF configuration mismatch between numerologies, which is different from the INI in the DBSR scenario

- Pilot signal design principles (in terms of pre-compensation and pilot placement) are proposed and discussed based on the theoretical analysis. Numerical results are provided to verify the effectiveness of the derivations and proposed principles.

The rest of this chapter is organized as follows. In Section II, the signal structure of the SBDR mixed-numerology system is demonstrated. The system modeling, CE performance analysis, and pilot signal design for the SU and MU scenarios are given in Section III and Section IV. In Section V, numerical results are presented. Finally, Section VI concludes this chapter.

Notations: The uppercase and lowercase bold letters, *e.g.*, $\mathbf{A}$ and $\mathbf{a}$, denote matrices and vectors, respectively. $\{\cdot\}^H$, $\{\cdot\}^T$, and $\{\cdot\}^\dagger$ represent the Hermitian conjugate, transpose operation and pseudo inverse, respectively. $\mathcal{E}\{\mathbf{A}\}$ and $||\mathbf{A}||_F^2$ are used to express the expectation and Frobenius matrix norm of $\mathbf{A}$, respectively. $\text{diag}\{\mathbf{A}\}$ means a vector formed by taking the diagonal elements of matrix $\mathbf{A}$, and $\text{diag}\{\mathbf{a}\}$ forms a diagonal matrix by taking each element of vector $\mathbf{a}$. $\lfloor\cdot\rfloor$ refers to the round down operation and $\text{mod}(\cdot)$ is the modulo operation. $\mathbf{I}_N$ and $\mathbf{0}_{N\times M}$ denote an N-dimension identity matrix and an $N \times M$ zero matrix, respectively.

4.2 Preliminary: Signal Structure

This chapter focuses on the SBDR scenario, *i.e.*, different numerologies have the same BB configurations and different RF configurations. Hence, the investigated system contains users of different RF processing bandwidth or sampling rate. The symbol structure of the signals can intuitively reflect the sampling rates. To this end, before introducing the system models, the symbol structure of different numerologies is depicted in this section.

Without loss of generality, two numerologies are considered in this chapter[2], and two subscripts are used to distinguish their parameters, *i.e.*, $\{\cdot\}_L$ for the low sampling rate numerology and $\{\cdot\}_H$ for the high sampling rate numerology. To have a clear view of how the mismatched sampling rates affect the system and simplify the derivations, it is considered that only one UE for each numerology[3]. The sampling rate of the UE with numerology 1 and numerology 2, *i.e.*, UE 1 and

---

[2] For the case with more than 2 numerologies, the interference will be mutually generated among different numerologies, which results in a more complex scenario. However, because the interference generated from each numerology is linearly superposed, such a system can be investigated by considering any two numerologies at a time. Therefore, the complex model is decoupled as a couple of basic models discussed in this chapter.

[3] Again, more UEs will increase the system complexity, but will not affect the underlying principle of the investigated system.

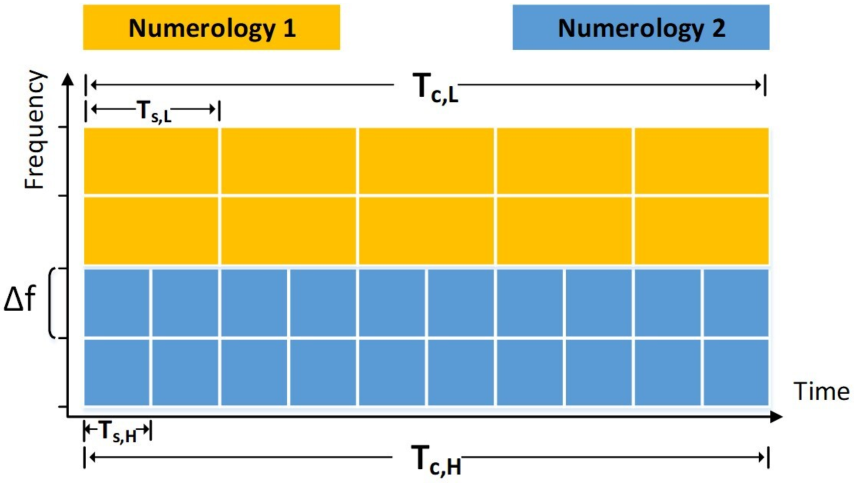

Figure 4.1: Symbol structure of the two different numerologies, where numerology 1 is the low sampling rate numerology with $N_L = 5$ and numerology 2 is the high sampling rate numerology with $N_H = 10$.

UE 2, is S_L and S_H, respectively. In addition, it is assumed that only one BS in the system, which is configured according to numerology 2. Considering the same subcarrier spacing Δf for both numerologies, we have the following relationship:

$$N_H = \frac{S_H}{\Delta f} > N_L = \frac{S_L}{\Delta f}, \tag{4.1}$$

where N_L and N_H are the DFT points of numerology 1 and numerology 2, respectively.

From Fig. 4.1, it can be seen that both signals have the same OFDM symbol length ($T_{c,L} = T_{c,H}$) but different sampling periods ($T_{s,L} > T_{s,H}$). In principle, the two numerologies in the same wireless communication system could have independent physical layer configurations. However, in practice, it is always beneficial (in terms of maintaining system performance and reducing the complexity of system design) to select the two coexisting numerologies so that $S_H/S_L = Q \in \mathbb{Z}^+$, where Q is the up-sampling rate. Such an assumption is aligned with the 3GPP specification design principle. Thus, we have the following equations:

$$T_{s,H} = 1/S_H, \qquad T_{s,L} = 1/S_L = QT_{s,H}, \tag{4.2}$$

$$T_{c,H} = N_H T_{s,H}, \qquad T_{c,L} = N_L T_{s,L} = T_{c,H}. \tag{4.3}$$

4.3 Single-User Model and Channel Estimation

In Chapter 3, it has been demonstrated that the signal distortion in the RF-differed MN system comes from the sampling difference between the Tx and Rx. This section presents a single-user scenario (as shown in Fig. 4.2) with only UE 1 and the BS such that the user is free of the INI and we can focus on the signal distortion. Note that although there is only one wireless communication link, the system constructed in the SU scenario is a mixed-numerology system as the Tx and Rx hold different PHY configurations. The multi-user scenario, which focuses on INI investigation, will be presented and discussed in the next section.

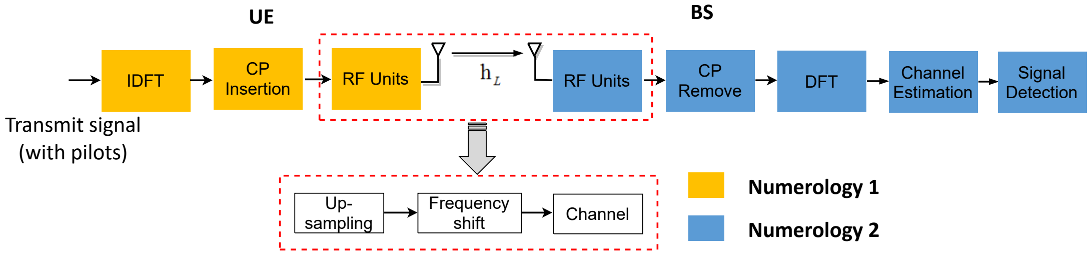

Figure 4.2: Mixed-numerology system model in single-user scenario, where yellow and blue blocks denote the components of numerology 1 and numerology 2 devices, respectively. The red dish boxes represent the equivalent process which transforms the RF processing into digital domain.

4.3.1 SU System Model

Assuming that an OFDM system with CP length longer than channel spread, and the channel stays constant over one OFDM symbol, we can divide it into a set of parallel single-carrier sub-systems [147]. In matrix notation, such a system can be simply expressed as:

$$\mathbf{y} = \mathbf{H}\mathbf{x} + \mathbf{n}, \tag{4.4}$$

where $\mathbf{x}$ and $\mathbf{y}$ are the input and output symbol vectors, respectively; $\mathbf{H}$ is the diagonal channel frequency response matrix, and $\mathbf{n}$ is the white noise. However, due to the sampling rate mismatch, such a simplification is invalidated in the proposed mixed-numerology system.

Fig. 4.2 illustrates a model for the uplink SU scenario. Assume $\mathbf{x}_L \in \mathbb{C}^{M_1 \times 1}$ is the modulated transmit signal with M_1 being the number of allocated subcarriers. After IDFT processing and CP insertion, the generated baseband signal can be expressed as:

$$\mathbf{x}_{L,bb} = \mathbf{C}_L\tilde{\mathbf{F}}_{N_L}\mathbf{x}_L, \tag{4.5}$$

where $\tilde{\mathbf{F}}_{N_L}$ corresponds to the first M_1 columns of $\mathbf{F}_{N_L}$, and $\mathbf{F}_{N_L}$ is an N_L-point normalized IDFT matrix; $\mathbf{C}_L = [\mathbf{0}_{L_{CP,L}\times(N_L-L_{CP,L})}, \mathbf{I}_{L_{CP,L}}; \mathbf{I}_{N_L}]$ is the CP insertion matrix with $L_{CP,L}$ as the CP length. Hence, we have the symbol length of the transmitted signal as $L_{sym,L} = N_L + L_{CP,L}$.

In a typical OFDM system, spectrum assignment could be performed by baseband operation, *i.e.*, allocating specific columns of the IDFT matrix to the assigned signal. Nevertheless, the processing bandwidth of UE 1 is too narrow to perform the spectrum assignment. Instead, this progress will be carried out by the RF unit. Moreover, the signal is up-sampled upon arriving at the receiver because of the Tx and the Rx sampling rate difference. To formulate the entire signal processing chain in the digital domain, an equivalent process is considered (as shown in the dashed box in Fig. 4.2), where the up-sampling and frequency shift can be performed by two matrices, *i.e.*, $\mathbf{U}$ and $\mathbf{\Phi}$, respectively. Define $L_{sym,H} = QL_{sym,L}$ as the signal length after up-sampling, matrix $\mathbf{U} \in \mathbb{Z}^{L_{sym,H}\times L_{sym,L}}$ can be formed as in Eq. (3.9). Assuming that M_1 consecutive subcarriers (indicated by $k \in \{K_L, K_L+1, \cdots, K_L+M_1-1\}$) are allocated to UE 1, and the i-th element of diagonal matrix $\mathbf{\Phi}$ can be expressed as $e^{j2\pi(i-QL_{CP,L}-1)(K_L-1)/N_H}$. At the receiver, let us define $\mathbf{R}_H = [\mathbf{0}_{N_H\times L_{CP,H}}, \mathbf{I}_{N_H}]$ as the CP removal matrix, and $\mathbf{F}_{N_H}^H$ as the normalized DFT matrix with N_H-points. The received signal $\mathbf{y}_L$ can be formulated as the following matrix form:

$$\mathbf{y}_L = \tilde{\mathbf{F}}_{N_H}^H\mathbf{R}_H\mathcal{H}_L\mathbf{\Phi}\mathbf{U}\mathbf{C}_L\tilde{\mathbf{F}}_{N_L}\mathbf{x}_L + \mathbf{n}_L, \tag{4.6}$$

where $\tilde{\mathbf{F}}_{N_H}^H$ corresponds to the $k \in \{K_L, K_L+1, \cdots, K_L+M_1-1\}$ rows of $\mathbf{F}_{N_H}^H$, and $\mathcal{H}_L$ is the Toeplitz matrix of the channel frequency response; $\mathbf{n}_L$ is a white Gaussian noise vector with a zero mean and variance of σ_L^2;

By applying the G-CCP-US theorem in Eq. (4.6), the received signal can be simplified as:

$$\mathbf{y}_L = \mathbf{H}_L\mathbf{\Gamma}\mathbf{x}_L + \mathbf{n}_L, \tag{4.7}$$

In Eq. (4.7), $\mathbf{H}_L \in \mathbb{C}^{M_1\times M_1} = \sqrt{N_H}\text{diag}(\dot{\mathbf{F}}_{N_H}^H\mathbf{h}_L)$ refers to the diagonal channel frequency response matrix, where $\mathbf{h}_L$ is the column vector of the channel impulse response with its length to be $L_{CH,L}$; $\dot{\mathbf{F}}_{N_H}^H$ is obtained by taking the first $L_{CH,L}$ columns of $\tilde{\mathbf{F}}_{N_H}^H$; $\mathbf{\Gamma} \in \mathbb{C}^{M_1\times M_1}$ is the signal distortion factor introduced by the

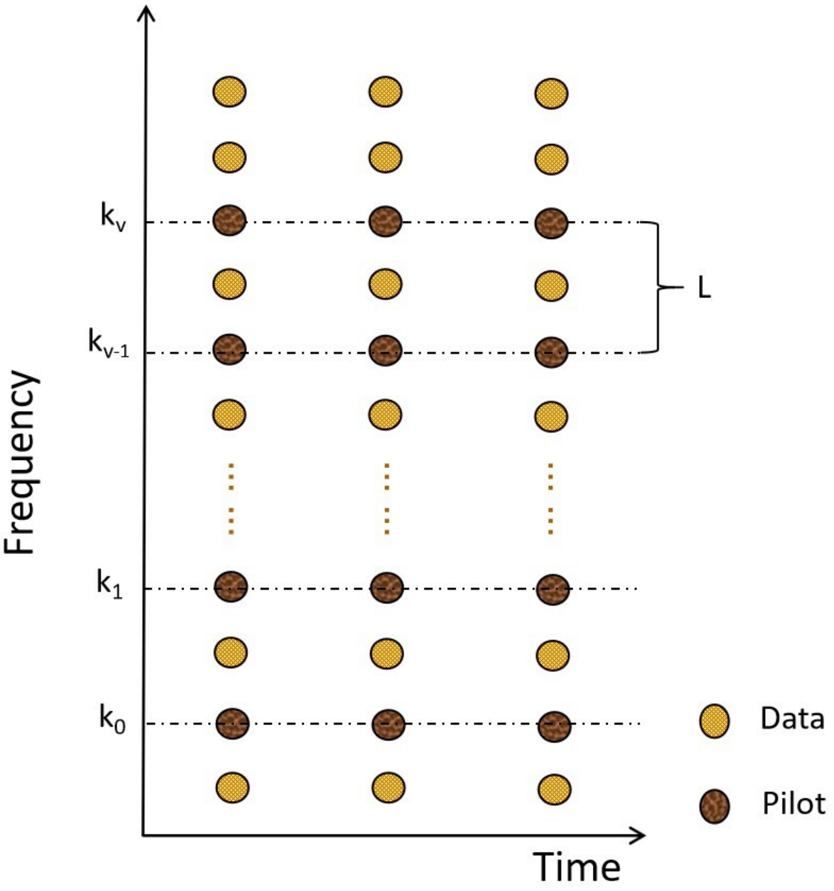

Figure 4.3: Comb-type pilot pattern applied in this chapter.

sampling rate mismatch, which can be represented as:

$$\boldsymbol{\Gamma} = \frac{1}{\sqrt{Q}} \sum_{i=1}^{Q} \boldsymbol{\Psi}_i, \tag{4.8}$$

where $\boldsymbol{\Psi}_i$ is a diagonal matrix with its k-th $(1 \leq k \leq M_1)$ diagonal element to be $e^{-j2\pi(i-1)(k-1)/N_H}$.

4.3.2 Channel Estimation in the SU Scenario

Assuming that $V+1$ pilots are uniformly inserted into the transmit signal, and the interval between every two pilots is L. We can calculate the pilot position index as $k_v = vL + k_0$ with $0 \leq v \leq V$, where k_0 is the subcarrier index of the first pilot signal. The corresponding pilot pattern is shown in Fig. 4.3. Based on such pilot signals, three CE methods, *i.e.*, LSLI, LS-DFT, and MMSE-DFT, are implemented in the proposed mixed-numerology system. Their performances in terms of channel estimation error are derived and discussed in this subsection. For simplification and to reduce the occupied space of some complex equations, we use

‘LL’, ‘LD’, and ‘MD’ as labels of LSLI, LS-DFT, and MMSE-DFT, respectively.

LSLI

Based on Eq. (4.7), the received signal at the k-th subcarrier is given by:

$$\mathbf{y}_L(k) = \mathbf{H}_L(k)\boldsymbol{\Gamma}(k)\mathbf{x}_L(k) + \mathbf{n}_L(k), \tag{4.9}$$

and the estimated channel gain at pilot subcarriers is calculated as:

$$\mathbf{H}_L^{LL}(k_v) = \frac{\mathbf{y}_L(k_v)}{\boldsymbol{\Gamma}(k_v)\mathbf{x}_L(k_v)} = \mathbf{H}_L(k_v) + \frac{\mathbf{n}_L(k_v)}{\boldsymbol{\Gamma}(k_v)\mathbf{x}_L(k_v)}. \tag{4.10}$$

Define $k = k_v + l$ with $0 \leq l \leq L-1$, we can express the estimated channel at arbitrary subcarrier as:

$$\mathbf{H}_L^{LL}(k) = \frac{L-l}{L}\mathbf{H}_L^{LL}(k_v) + \frac{l}{L}\mathbf{H}_L^{LL}(k_{v+1}). \tag{4.11}$$

Accordingly, the MSE of the LSLI channel estimation can be achieved as:

$$\begin{aligned}\epsilon_L^{LL} &= \sum_{v=0}^{V-1}\sum_{l=0}^{L-1}\mathcal{E}|\mathbf{H}_L^{LL}(k) - \mathbf{H}_L(k)|^2 \\ &= \sum_{v=0}^{V-1}\sum_{l=0}^{L-1}\mathcal{E}|\frac{L-l}{L}\mathbf{H}_L^{LL}(k_v) + \frac{l}{L}\mathbf{H}_L^{LL}(k_{v+1}) - \mathbf{H}_L(k_v+l)|^2 \\ &= \alpha_L + \beta_L,\end{aligned} \tag{4.12}$$

where α_L and β_L are error components resulting from the linear interpolation and the noise, respectively. By substituting Eq. (4.10) and Eq. (4.11) into Eq. (4.12), we have:

$$\begin{aligned}\alpha_L &= \sum_{v=0}^{V-1}\sum_{l=0}^{L-1}\mathcal{E}|\frac{L-l}{L}\mathbf{H}_L(k_v) + \frac{l}{L}\mathbf{H}_L(k_{v+1}) - \mathbf{H}_L(k_v+l)|^2 \\ &= \frac{5L-1}{3L}R_f(0) + \frac{L+1}{6L}[R_f(-L) + R_f(L)] \\ &- \frac{1}{L-1}\sum_{l=0}^{L-1}[\frac{L-l}{L}(R_f(-l) + R_f(l)) \\ &+ \frac{l}{L}(R_f(L-l) + R_f(l-L))],\end{aligned} \tag{4.13}$$

where $R_f(i)$ is the channel frequency correlation function [148]. If we assume P_L to be the uniformly distributed pilot signal power, β_L can be written as:

$$\begin{aligned}\beta_L &= \sum_{v=0}^{V-1}\sum_{l=0}^{L-1}\mathcal{E}\left|\frac{L-l}{L}\frac{\mathbf{n}_L(k_v)}{\mathbf{\Gamma}(k_v)\mathbf{x}_L(k_v)}+\frac{l}{L}\frac{\mathbf{n}_L(k_{v+1})}{\mathbf{\Gamma}(k_{v+1})\mathbf{x}_L(k_{v+1})}\right|^2\\ &= \frac{\sigma_L^2}{P_L M_1 L^2}\sum_{v=0}^{V-1}\sum_{l=0}^{L-1}\left[(L-l)^2\frac{1}{|\mathbf{\Gamma}(k_v)|^2}+l^2\frac{1}{|\mathbf{\Gamma}(k_{v+1})|^2}\right]\\ &= \frac{\sigma_L^2}{P_L M_1}\sum_{v=0}^{V-1}\left[\frac{(L+1)(2L+1)}{6L|\mathbf{\Gamma}(k_v)|^2}+\frac{(L-1)(2L-1)}{6L|\mathbf{\Gamma}(k_{v+1})|^2}\right].\end{aligned} \tag{4.14}$$

It can be seen from the mathematical expression of ϵ_L^{LL} that two components *i.e.*, α_L and β_L, jointly contribute to the LSLI estimation error. Given a fixed channel, it is interesting to notice that the linear interpolation error α_L is only determined by the pilot distance L. On the other hand, the noise-related error β_L seems to have relationships with more parameters, such as the pilot distance L and the PNR, *i.e.*, $\frac{P_L}{\sigma_L^2}$. Besides, compared to single numerology systems, a signal distortion factor $\mathbf{\Gamma}$ is introduced to the noise component of LSLI CE error because of the sampling rate mismatch.

LS-DFT

The matrix form of the received signal at pilot subcarriers can be achieved based on Eq. (4.7):

$$\mathbf{y}_{k_v} = \mathbf{x}_{k_v}\mathbf{\Gamma}_{k_v}\mathbf{H}_{k_v} + \mathbf{n}_{k_v}, \tag{4.15}$$

where $\mathbf{x}_{k_v} \in \mathbb{C}^{1\times(V+1)}$ is the vector of pilot signals, and the diagonal matrix $\mathbf{\Gamma}_{k_v} \in \mathbb{C}^{(V+1)\times(V+1)}$ is obtained by taking the corresponding elements of $\mathbf{\Gamma}$; $\mathbf{H}_{k_v} \in \mathbb{C}^{(V+1)\times(V+1)} = \sqrt{N_H}\text{diag}(\ddot{\mathbf{F}}_{N_H}^H\mathbf{h}_L)$ contains the channel frequency response at pilot subcarriers with $\ddot{\mathbf{F}}_{N_H}^H$ formed by taking the $k_v \in [k_0, k_1, \cdots, k_V]$ rows of $\dot{\mathbf{F}}_{N_H}^H$. The estimation of channel impulse response can be obtained as: $\mathbf{h}_L^{LD} \in \mathbb{C}^{L_{CH,L}\times 1} = \frac{1}{\sqrt{N_H}}[\text{diag}(\mathbf{x}_{k_v}\mathbf{\Gamma}_{k_v})\ddot{\mathbf{F}}_{N_H}^H]^\dagger\mathbf{y}_{k_v}^T$, and the LS-DFT channel estimation is given by:

$$\mathbf{H}_L^{LD} = \sqrt{N_H}\dot{\mathbf{F}}_{N_H}^H\mathbf{h}_L^{LD} = \dot{\mathbf{F}}_{N_H}^H[\text{diag}(\mathbf{x}_{k_v}\mathbf{\Gamma}_{k_v})\ddot{\mathbf{F}}_{N_H}^H]^\dagger\mathbf{y}_{k_v}^T. \tag{4.16}$$

Based on Eq. (4.16), the MSE of DFT channel estimation can be calculated as:

$$\begin{aligned}\epsilon_L^{LD} &= \mathcal{E}||\mathbf{H}_L - \mathbf{H}_L^{LD}||_F^2 \\ &= \mathcal{E}||\dot{\mathbf{F}}_{N_H}^H[\mathrm{diag}(\mathbf{x}_{k_v}\mathbf{\Gamma}_{k_v})\ddot{\mathbf{F}}_{N_H}^H]^\dagger\mathbf{n}_{k_v}||_F^2 \\ &= \frac{\sigma_L^2}{M_1}||\dot{\mathbf{F}}_{N_H}^H[\mathrm{diag}(\mathbf{x}_{k_v}\mathbf{\Gamma}_{k_v})\ddot{\mathbf{F}}_{N_H}^H]^\dagger||_F^2.\end{aligned} \tag{4.17}$$

By using $||\mathbf{A}||_F = \sqrt{\mathbf{trace}(\mathbf{A}^H\mathbf{A})}$ and $\mathbf{trace}(\mathbf{AB}) = \mathbf{trace}(\mathbf{BA})$, Eq. (4.17) can be reformed to the following expression:

$$\epsilon_L^{LD} = \frac{\sigma_L^2}{P_L M_1}\mathbf{trace}\{(\ddot{\mathbf{F}}_{N_H}\mathbf{\Gamma}_{k_v}^H\mathbf{\Gamma}_{k_v}\ddot{\mathbf{F}}_{N_H}^H)^\dagger\dot{\mathbf{F}}_{N_H}\dot{\mathbf{F}}_{N_H}^H\}. \tag{4.18}$$

Eq. (4.18) reveals that both PNR and $\mathbf{\Gamma}$ affect the value of ϵ_L^{LD}. Besides, compared to SN systems, the sampling rate mismatch introduces different submatrices of $\mathbf{F}_{N_H}$ and $\mathbf{F}_{N_H}^H$. It should be noted that $\ddot{\mathbf{F}}_{N_H}\ddot{\mathbf{F}}_{N_H}^H$ and $\dot{\mathbf{F}}_{N_H}\dot{\mathbf{F}}_{N_H}^H$ cannot generate an identity matrix since their columns are not orthogonal.

MMSE-DFT

Let us define $\mathbf{G}_L = \sqrt{N_H}\mathrm{diag}(\mathbf{x}_{k_v}\mathbf{\Gamma}_{k_v})\ddot{\mathbf{F}}_{N_H}^H$. Similar to that in LS-DFT estimation, the MMSE based channel estimation can be written as [147]:

$$\mathbf{H}_L^{MD} = \sqrt{N_H}\dot{\mathbf{F}}_{N_H}^H\mathbf{R}_t\mathbf{G}_L^H(\mathbf{G}_L\mathbf{R}_t\mathbf{G}_L^H + \sigma_H^2\mathbf{I}_{V+1})^{-1}\mathbf{y}_{k_v}^T, \tag{4.19}$$

where $\mathbf{R}_t$ is the correlation matrix of the channel impulse response. Thereby, we can obtain the MSE of the MMSE-DFT channel estimation as follows:

$$\begin{aligned}\epsilon_L^{MD} &= \mathcal{E}||\mathbf{H}_L - \mathbf{H}_L^{MD}||_F^2 \\ &= \mathbf{trace}\{\mathcal{E}[(\mathbf{H}_L - \mathbf{H}_L^{MD})\mathbf{H}_L^H] \\ &- \mathcal{E}[(\mathbf{H}_L - \mathbf{H}_L^{MD})(\mathbf{H}_L^{MD})^H]\}.\end{aligned} \tag{4.20}$$

Referring to the orthogonality principle [149], we know that the second term within the **trace** operation is zero. By substituting Eq. (4.15) and Eq. (4.19) into Eq. (4.20), ϵ_L^{MD} is finally derived as:

$$\begin{aligned}\epsilon_L^{MD} &= \mathbf{trace}\{\mathcal{E}(\mathbf{H}_L\mathbf{H}_L^H) - \mathcal{E}(\mathbf{H}_L^{MD}\mathbf{H}_L^H)\} \\ &= \frac{1}{M_1}\mathbf{trace}\{\mathbf{R}_f - \mathbf{R}_f^{(1)}[\mathbf{R}_f^{(2)} + \frac{\sigma_L^2}{P_L}(\mathbf{\Gamma}_{k_v}^H\mathbf{\Gamma}_{k_v})^{-1}]^{-1}\mathbf{R}_f^{(3)}\},\end{aligned} \tag{4.21}$$

where $\mathbf{R}_f = N_H\dot{\mathbf{F}}_{N_H}^H\mathbf{R}_t\dot{\mathbf{F}}_{N_H}$ is the correlation matrix of the channel frequency response; $\mathbf{R}_f^{(1)} = N_H\dot{\mathbf{F}}_{N_H}^H\mathbf{R}_t\ddot{\mathbf{F}}_{N_H}$, $\mathbf{R}_f^{(2)} = N_H\ddot{\mathbf{F}}_{N_H}^H\mathbf{R}_t\ddot{\mathbf{F}}_{N_H}$, and $\mathbf{R}_f^{(3)} =$

$N_H \ddot{\mathbf{F}}^H_{N_H} \mathbf{R}_t \dot{\mathbf{F}}_{N_H}$ are different submatrices of $\mathbf{R}_f$.

After Eq. (4.12), Eq. (4.18), and Eq. (4.21) have been derived, it can be observed that the estimation error of all three methods is inversely proportional to PNR. Also, the pilot distance L plays an important role in determining the performance of CEs. Although L does not appear in Eq. (4.18) and Eq. (4.21) directly, it actually affects the number of pilot signals (*i.e.*, $V + 1$) as well as the position they are placed (*i.e.*, k_v). In addition, it is noticed that the signal distortion factor $\mathbf{\Gamma}$ appears in all of these equations in the form of $\sum_{v=0}^{V-1} (\Gamma^H_{k_v} \Gamma_{k_v})^{-1}$ or $\mathbf{trace}(\mathbf{\Gamma}^H_{k_v} \mathbf{\Gamma}_{k_v})^{-1}$. In other words, the integration of all components of $(\mathbf{\Gamma}^H_{k_v} \mathbf{\Gamma}_{k_v})^{-1}$, which can be written as:

$$(\mathbf{\Gamma}^H_{k_v} \mathbf{\Gamma}_{k_v})^{-1} = \begin{cases} \frac{1}{Q}, & \text{if} \quad k_v = 1 \\ \frac{Q(1-\cos\frac{2\pi(k_v-1)}{N_H})}{1-\cos\frac{2\pi(k_v-1)}{N_L}}, & \text{if} \quad k_v \neq 1. \end{cases} \tag{4.22}$$

4.3.3 Pilot Design in the SU Scenario

To understand how $\mathbf{\Gamma}$ impacts the channel estimation performance and propose a targeted pilot design method, a figure of $(\mathbf{\Gamma}^H \mathbf{\Gamma})^{-1}$ against subcarrier index is depicted in Fig. 4.4. Basically, with the effect of $\mathbf{\Gamma}$, the last few subcarriers have more significant contributions to the channel estimation error. This ‘tail-infected’ feature is also related to the configuration difference between the numerologies, *i.e.*, the up-sampling rate Q. We can find that higher Q leads to larger tail values. It is worth noting that when $Q = 1$, *i.e.*, users hold the same sampling rate, the mixed-numerology system degrades to a conventional OFDM system where no distortion exists.

Therefore, in SU mixed-numerology systems, positions of pilot signals should be carefully selected to avoid the ’tail’ subcarriers, especially when numerologies differ markedly from each other. Let us define the pilot position set as the combination of all pilot signal indices. We can use the pilot distance L together with the index of the first pilot signal k_0 to denote a specific pilot position set as $\mathbf{P}^{k_0}_L$. Assume two sets of pilots, *i.e.*, $\mathbf{P}^1_{12}$ and $\mathbf{P}^{12}_{12}$, are separately deployed in 5 PRBs (*i.e.*, 60 subcarriers). The position index for the two sets can be illustrated as $\mathbf{P}^1_{12} = [1, 13, 25, 37, 49]$ and $\mathbf{P}^{12}_{12} = [12, 24, 56, 48, 60]$, respectively. In this way, all pilots of $\mathbf{P}^1_{12}$ lie on the first subcarrier of each PRB, while pilots of $\mathbf{P}^{12}_{12}$ are placed on the last subcarrier of each PRB. Theoretically, the former would result in a much smaller CE error than the latter.

Although the proposed pilot placement method could generate better channel estimation results, it considerably limits the available subcarriers for pilot signals.

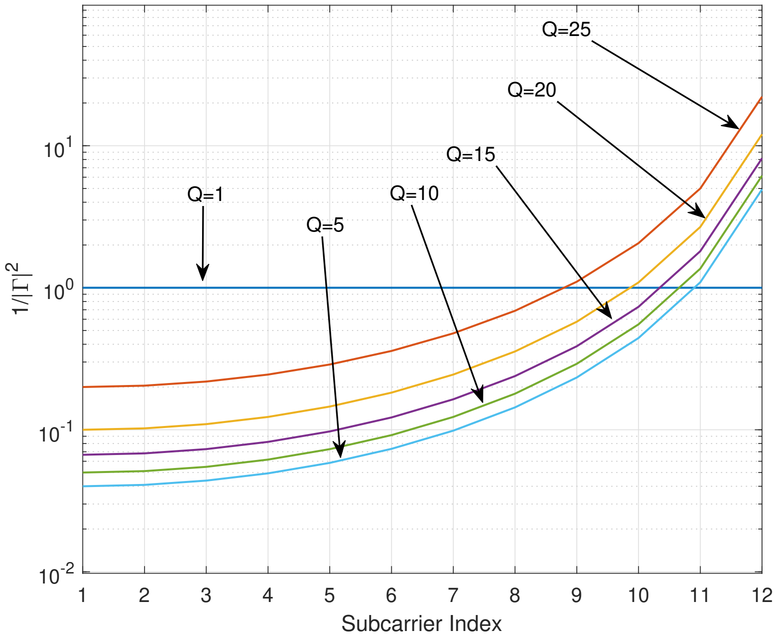

Figure 4.4: $(\mathbf{\Gamma}^H\mathbf{\Gamma})^{-1}$ v.s. subcarrier index within 1 PRB, where $\mathbf{\Gamma}$ is the signal distortion factor caused by the sampling rate mismatch between the Tx and Rx. The entries of $\mathbf{\Gamma}$ is mainly decided by the up-sampling rate, as shown in Eq. (4.8).

Hence, we propose an alternative approach to mitigate the negative effect of $\mathbf{\Gamma}$ by implementing an efficient pre-compensation in the transmitter side. To be specific, $\mathbf{x}_{k_v}\mathbf{\Gamma}_{k_v}^{-1}$ instead of $\mathbf{x}_{k_v}$ will be transmitted as pilot signals. To this end, the 'tail-infected' feature of the CE performance in mixed-numerology scenarios is expected to be eliminated. More details will be provided and discussed with simulation results in Sec 4.5.

4.4 Multi-User Model and Channel Estimation

This section investigates the mixed-numerology system with both UE 1 and UE 2 on the transmitter side. Compared to the SU scenario where only one UE is transmitting signals, UE 2 is added to the system with a higher sampling rate, as shown in Fig. 4.5. Since the orthogonality is destroyed by the configuration mismatch between UE 1 and the BS, the power leakage of the UE 1 signal may come into the subcarriers for UE 2. In contrast, benefiting from the assumption that UE 2 holds the same physical layer configurations as the BS, it does not suffer from signal distortion and does not generate interference to UE 1 (more detailed analyses are provided in the following section). Therefore, by investigating the received UE 2 signal, we can focus on the INI analysis of the mixed-numerology system.

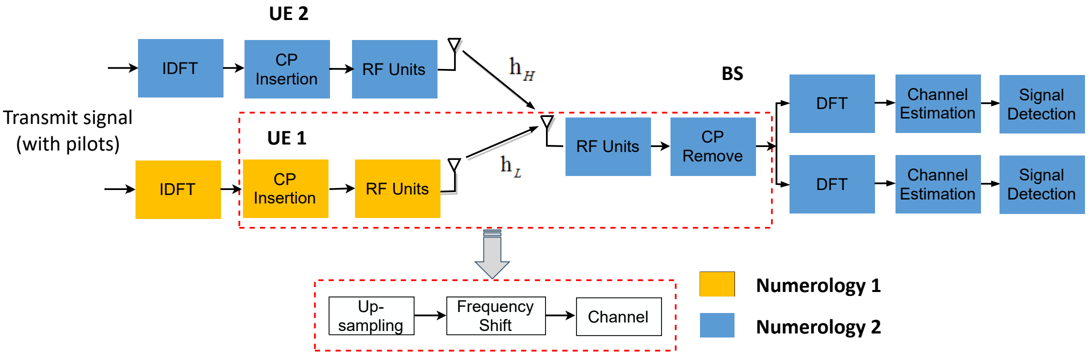
UE 2
IDFT
CP Insertion
RF Units
h_H
BS
Transmit signal (with pilots)
UE 1
IDFT
CP Insertion
RF Units
h_L
RF Units
CP Remove
DFT
Channel Estimation
Signal Detection
DFT
Channel Estimation
Signal Detection
Up-sampling
Frequency Shift
Channel
Numerology 1
Numerology 2

Figure 4.5: Mixed-numerology system model in multi-user scenario, where the yellow and blue blocks denote the components of numerology 1 and numerology 2 devices, respectively. The red dish boxes represent the equivalent process which transforms the RF processing into digital domain.

4.4.1 MU System Model

A completed MU mixed-numerology system model is shown in Fig. 4.5. Assuming $\{K_L, K_L+1, \cdots, K_L+M_1-1\}$ and $\{K_H, K_H+1, \cdots, K_H+M_2-1\}$ are two sets of non-overlapping subcarriers allocated to UE 1 and UE 2, respectively. We can express the output signals at the BS as the following matrix notations:

$$\mathbf{y}_H = \bar{\mathbf{F}}_N^H \mathbf{R}_H \mathcal{H}_H \mathbf{C}_H \bar{\mathbf{F}}_{N_H} \mathbf{x}_H + \boldsymbol{\nu}_H + \mathbf{n}_H, \tag{4.23}$$

$$\mathbf{y}_L = \tilde{\mathbf{F}}_{N_H}^H \mathbf{R}_H \mathcal{H}_L \boldsymbol{\Phi} \mathbf{U} \mathbf{C}_L \tilde{\mathbf{F}}_{N_L} \mathbf{x}_L + \boldsymbol{\nu}_L + \mathbf{n}_L, \tag{4.24}$$

where $\mathbf{x}_H$ and $\mathbf{y}_H$ are the transmit and receive signal of UE 2, respectively; $\bar{\mathbf{F}}_{N_H}^H$ corresponds to the $k \in \{K_H, K_H+1, \cdots, K_H+M_2-1\}$ columns of $\mathbf{F}_{N_H}^H$, and $\mathcal{H}_H$ is the Toeplitz matrix of the channel frequency response. In particular, ν_H refers to the interference generated from UE 1 to UE 2, and ν_L denotes the interference from UE 2 to UE 1. The equations of ν_H and ν_L can be expressed as:

$$\nu_H = \bar{\mathbf{F}}_{N_H}^H \mathbf{R}_H \mathcal{H}_L \boldsymbol{\Phi} \mathbf{U} \mathbf{C}_L \tilde{\mathbf{F}}_{N_L} \mathbf{x}_L, \tag{4.25}$$

$$\nu_L = \tilde{\mathbf{F}}_{N_H}^H \mathbf{R}_H \mathcal{H}_H \mathbf{C}_H \bar{\mathbf{F}}_{N_H} \mathbf{x}_H. \tag{4.26}$$

Since $\tilde{\mathbf{F}}_{N_H}^H$ and $\bar{\mathbf{F}}_{N_H}^H$ correspond to orthogonal columns of the same DFT matrix, we can easily know that $\boldsymbol{\nu}_L = 0$. By using the G-CCP-US theorem, $\boldsymbol{\nu}_H$ can be rewritten as $\boldsymbol{\nu}_H = \bar{\mathbf{H}}_L \boldsymbol{\Lambda} \mathbf{x}_L$, while Eq. (4.23) and Eq. (4.24) are simply presented as:

$$\mathbf{y}_H = \mathbf{H}_H\mathbf{x}_H + \bar{\mathbf{H}}_L\bar{\mathbf{\Theta}}_\eta\bar{\mathbf{\Lambda}}\mathbf{x}_L + \mathbf{n}_H \quad (4.27)$$

$$\mathbf{y}_L = \mathbf{H}_L\mathbf{\Gamma}\mathbf{x}_L + \mathbf{n}_L, \quad (4.28)$$

where $\mathbf{H}_H = \sqrt{N_H}\text{diag}(\bar{\mathbf{F}}_{N_H}^H[\mathbf{h}_H, \mathbf{0}_{1\times(N_H-L_{CH,H})}]^T)$ and $\bar{\mathbf{H}}_L = \sqrt{N_H}\text{diag}(\bar{\mathbf{F}}_{N_H}^H[\mathbf{h}_L, \mathbf{0}_{1\times(N_H-L_{CH,L})}]^T)$ are channel frequency responses of the desired UE 2 signal and the interference, respectively; $\bar{\mathbf{\Theta}}_\eta$ is a $M_2 \times N_H$ dimension matrix by taking the $k \in \{K_H, K_H+1, \cdots, K_H+M_2-1\}$ rows of $\mathbf{\Theta}_\eta$. Defining $\eta = K_L - 1$, the expression of $\mathbf{\Theta}_\eta$ can be written as:

$$\mathbf{\Theta}_\eta = [\mathbf{I}_{N_H,1}; \mathbf{I}_{N_H,2}], \quad (4.29)$$

where $\mathbf{I}_{N_H,1}$ and $\mathbf{I}_{N_H,2}$ are obtained by taking the last η and the first $N_H - \eta$ rows of $\mathbf{I}_N$. Similarly, $\bar{\mathbf{\Lambda}}$ is an $N_H \times M_1$ dimension matrix composed of the first M_1 columns of $\mathbf{\Lambda} = [\boldsymbol{\upsilon}_0, \boldsymbol{\upsilon}_1, \cdots, \boldsymbol{\upsilon}_{Q-1}]^T$, where $\boldsymbol{\upsilon}_l$ is an $N_L \times N_L$ diagonal matrix with its k-th $(1 \le k \le N_L)$ diagonal element to be:

$$\upsilon_l(k) = \frac{1}{\sqrt{Q}}\sum_{i=1}^{Q} e^{-j2\pi(i-1)(k-1+lN_L)/N_H}. \quad (4.30)$$

According to Eq. (4.27) and Eq. (4.28), we know that the output signal $\mathbf{y}_L$ has exactly the same expression as in the SU scenario; while $\mathbf{y}_H$ contains an interference term but its desired part, *i.e.*, $\mathbf{H}_H\mathbf{x}_H$, is not distorted. In other words, the orthogonality between UE 2 and the BS is well maintained, and the signal of UE 2 can be well separated from UE 1 signal in the BS. UE 1 is free from interference and shows the same feature as in the SU scenario. The following section focuses on $\mathbf{y}_H$ to investigate how the INI affects the channel estimation performance.

4.4.2 Channel Estimation in the MU Scenario

Since we only carry out the channel estimation for $\mathbf{y}_H$ in the MU scenario, the same symbols in the SU scenario will be reused to avoid complex notations. For example, the total number of pilot signals is $(V+1)$, k_v denotes the pilot position index, and L is the pilot distance. By considering $\boldsymbol{\nu}_H$ as a part of the noise, and following similar steps as that has been done in Section. 4.3, the MSE of three CE methods in the MU scenario can be derived as follows.

LL

The estimated channel gain at pilot subcarriers is calculated as:

$$\mathbf{H}_H^{LL}(k_v) = \frac{\mathbf{y}_H(k_v)}{\mathbf{x}_H(k_v)} = \mathbf{H}_H(k_v) + \frac{\boldsymbol{\nu}_H(k_v) + \mathbf{n}_H(k_v)}{\mathbf{x}_H(k_v)}. \tag{4.31}$$

Thus, we have the estimated channel at arbitrary subcarrier as:

$$\mathbf{H}_H^{LL}(k) = \frac{L-l}{L}\mathbf{H}_H^{LL}(k_v) + \frac{l}{L}\mathbf{H}_H^{LL}(k_{v+1}). \tag{4.32}$$

Accordingly, the MSE of the LSLI channel estimation for $\mathbf{y}_H$ can be obtained as:

$$\begin{aligned} \epsilon_H^{LL} &= \sum_{v=0}^{V-1}\sum_{l=0}^{L-1} \mathcal{E}|\mathbf{H}_H^{LL}(k) - \mathbf{H}_H(k)|^2 \\ &= \alpha_H + \beta_H, \end{aligned} \tag{4.33}$$

where α_H and β_H correspond to the interpolation error and noise related error, respectively. Since the interpolation error is only decided by the pilot distance, α_H has the same expression as its counterpart (α_L) in the SU scenario, *i.e.*,

$$\begin{aligned} \alpha_H = &\frac{5L-1}{3L}R_f(0) + \frac{L+1}{6L}[R_f(-L) + R_f(L)] \\ &- \frac{1}{L-1}\sum_{l=0}^{L-1}[\frac{L-l}{L}(R_f(-l) + R_f(l)) \\ &+ \frac{l}{L}(R_f(L-l) + R_f(l-L))]. \end{aligned} \tag{4.34}$$

It needs to be noted that the channel frequency correlation function $R_f(i)$ shall be calculated based on $\mathbf{H}_H$. Besides, the expression of β_H can be written as:

$$\begin{aligned} \beta_H = &\sum_{v=0}^{V-1}\sum_{l=0}^{L-1}\mathcal{E}|\frac{L-l}{L}\frac{\boldsymbol{\nu}_H(k_v) + \mathbf{n}_H(k_v)}{\mathbf{x}_H(k_v)} \\ &+ \frac{l}{L}\frac{\boldsymbol{\nu}_H(k_{v+1}) + \mathbf{n}_H(k_{v+1})}{\mathbf{x}_H(k_{v+1})}|^2 \\ = &\frac{1}{P_H M_2}\sum_{v=0}^{V-1}\left[\frac{(L+1)(2L+1)(|\boldsymbol{\nu}_H(k_v)|^2 + \sigma_H^2)}{6L}\right. \\ &+ \left.\frac{(L-1)(2L-1)(|\boldsymbol{\nu}_H(k_{v+1})|^2 + \sigma_H^2)}{6L}\right]. \end{aligned} \tag{4.35}$$

LS-DFT

Firstly, let us define $\hat{\mathbf{F}}_{N_H}^H$ as a submatrix of $\bar{\mathbf{F}}_{N_H}^H$ by taking its first $L_{CH,H}$ columns, and $\check{\mathbf{F}}_{N_H}^H$ composes of the $k_v \in [k_0, k_1, \cdots, k_V]$-th rows of $\hat{\mathbf{F}}_{N_H}^H$. Similar to Eq. (4.16), the LS-DFT channel estimation for $\mathbf{y}_H$ can be expressed as:

$$\mathbf{H}_H^{LD} = \hat{\mathbf{F}}_{N_H}^H [\text{diag}(\mathbf{x}_{k_v})\check{\mathbf{F}}_{N_H}^H]^\dagger \mathbf{y}_{k_v}^T, \tag{4.36}$$

where $\mathbf{x}_{k_v}$ and $\mathbf{y}_{k_v}$ are formed by the values of $\mathbf{x}_H$ and $\mathbf{y}_H$ in pilot positions, respectively. Based on Eq. (4.36), the corresponding MSE can be calculated as:

$$\begin{aligned}\epsilon_H^{LD} &= \mathcal{E}||\mathbf{H}_H - \mathbf{H}_H^{LD}||_F^2 \\ &= \mathcal{E}||\hat{\mathbf{F}}_{N_H}^H [\text{diag}(\mathbf{x}_{k_v})\check{\mathbf{F}}_{N_H}^H]^\dagger (\boldsymbol{\nu}_{k_v} + \mathbf{n}_{k_v})||_F^2 \\ &= \frac{\textbf{trace}\{(\check{\mathbf{F}}_{N_H}^H)^\dagger (\boldsymbol{\nu}_{k_v}\boldsymbol{\nu}_{k_v}^H + \sigma_H^2 \mathbf{I}_{V+1})(\check{\mathbf{F}}_{N_H})^\dagger \hat{\mathbf{F}}_{N_H} \hat{\mathbf{F}}_{N_H}^H\}}{P_H M_2},\end{aligned} \tag{4.37}$$

where $\boldsymbol{\nu}_{k_v}$ and $\mathbf{n}_{k_v}$ are obtained by taking the $k_v \in [k_0, k_1, \cdots, k_V]$-th values of $\boldsymbol{\nu}_H$ and $\mathbf{n}_H$, respectively; while P_H denotes the power of pilot signals.

MMSE-DFT

If we define $\mathbf{G}_H = \sqrt{N_H}\text{diag}(\mathbf{x}_{k_v})\check{\mathbf{F}}_{N_H}^H$, the MMSE based channel estimation can be written as:

$$\mathbf{H}_H^{MD} = \sqrt{N_H}\hat{\mathbf{F}}_{N_H}^H \mathbf{R}_t \mathbf{G}_H^H (\mathbf{G}_H \mathbf{R}_t \mathbf{G}_H^H + \boldsymbol{\nu}_{k_v}\boldsymbol{\nu}_{k_v}^H + \sigma_L^2 \mathbf{I}_{V+1})^{-1} \mathbf{y}_{k_v}^T, \tag{4.38}$$

where $\mathbf{R}_t$ is the correlation matrix of channel impulse response achieved from $\mathbf{h}_H$. Accordingly, the channel estimation error of $\mathbf{y}_H$ can be calculated as:

$$\begin{aligned}\epsilon_H^{MD} &= \mathcal{E}||\mathbf{H}_H - \mathbf{H}_H^{MD}||_F^2 = \textbf{trace}\{\mathcal{E}(\mathbf{H}_H\mathbf{H}_H^H) - \mathcal{E}(\mathbf{H}_H^{MD}\mathbf{H}_H^H)\} \\ &= \frac{1}{M_2}\textbf{trace}\{\mathbf{R}_f - \mathbf{R}_f^{(1)}[\mathbf{R}_f^{(2)} + \frac{\boldsymbol{\nu}_{k_v}\boldsymbol{\nu}_{k_v}^H + \sigma_L^2 \mathbf{I}_{V+1}}{P_H}]^{-1}\mathbf{R}_f^{(3)}\},\end{aligned} \tag{4.39}$$

where $\mathbf{R}_f = N_H \hat{\mathbf{F}}_{N_H}^H \mathbf{R}_t \hat{\mathbf{F}}_{N_H}$ is the channel frequency response correlation matrix; $\mathbf{R}_f^{(1)} = N_H \hat{\mathbf{F}}_{N_H}^H \mathbf{R}_t \check{\mathbf{F}}_{N_H}$, $\mathbf{R}_f^{(2)} = N_H \check{\mathbf{F}}_{N_H}^H \mathbf{R}_t \check{\mathbf{F}}_{N_H}$, and $\mathbf{R}_f^{(3)} = N_H \check{\mathbf{F}}_{N_H}^H \mathbf{R}_t \hat{\mathbf{F}}_{N_H}$ are different submatrices of $\mathbf{R}_f$.

Eq. (4.33), Eq. (4.37), and Eq. (4.39) indicate that in the proposed MU scenario, the MSE of three CE methods all inversely proportional to the average pilot signal to interference plus noise ratio (PINR) among all pilot subcarriers. Compared to single numerology OFDM systems, the involving of the interference

$\boldsymbol{\nu}_H$ discredits the results generated by the traditional channel estimation methods. As will be shown in Section. 4.5, the interference causes an error floor for both LSLI and LS-DFT CE. Therefore, constraining the negative influence from such interference is the key to achieving a decent estimation performance in mixed-numerology systems.

Given that the interference expression has been derived, the most intuitive approach is to perform the interference cancellation by the detected UE 1 signal. Assume $\hat{\mathbf{x}}_L$ and $\hat{\mathbf{h}}_L$ are the estimated UE 1 signal and channel impulse response, the interference cancellation factor can be written as:

$$\gamma = \sqrt{N_H}\text{diag}(\bar{\mathbf{F}}_{N_H}^H[\hat{\mathbf{h}}_L, \mathbf{0}_{1\times(N_H-L_{CH,L})}]^T)\bar{\mathbf{\Theta}}_\eta\bar{\mathbf{\Lambda}}\hat{\mathbf{x}}_L. \tag{4.40}$$

The UE 2 signal after interference cancellation can be achieved by $\hat{\mathbf{y}}_H = \mathbf{y}_H - \gamma$. Such a method is simple to implement with moderate complexity and is applicable in almost any situation. However, the channel estimation and signal detection error of the UE 1 signal is introduced in γ, which makes this approach less attractive.

4.4.3 Pilot Design in the MU Scenario

Alternatively, we can improve the CE performance by applying a more effective interference-free pilot transmission. Based on Eq. (4.27), the power of interference is given by:

$$\mathbf{P}_\nu = \mathcal{E}|\mathbf{diag}(\bar{\mathbf{H}}_L\bar{\mathbf{\Theta}}_\eta\bar{\mathbf{\Lambda}}\mathbf{x}_L\mathbf{x}_L^H\bar{\mathbf{\Lambda}}^H\bar{\mathbf{\Theta}}_\eta\bar{\mathbf{H}}_L^H)|. \tag{4.41}$$

Assuming UE 1 signal is modulated by BPSK/QPSK [4], which has an uniformly distributed power ρ. Also, considering an normalized channel gain, *i.e.*, $\mathcal{E}\{\sum_{i=1}^{L_{CH,L}}|h_L(i)|^2\} = 1$, Eq. (4.41) can be simplified as:

$$\mathbf{P}_\nu = \rho\mathbf{diag}(\bar{\mathbf{\Theta}}_\eta\bar{\mathbf{\Lambda}}\bar{\mathbf{\Lambda}}^H\bar{\mathbf{\Theta}}_\eta^H). \tag{4.42}$$

By substituting Eq. (4.29) and Eq. (4.30) into Eq. (4.42), the subcarriers (among the whole system bandwidth) with ($\mathbf{k}_{nz}^{<l>}$) and without ($\mathbf{k}_z^{<l>}$) interference can be written as

---

[4] Such an assumption is reasonable since users of numerology 1 have much lower sampling rate than those of numerology 2, and are considered as low-cost devices. Low order modulation is always the best choice for such devices to maintain low power consummation.

$$\begin{aligned} \mathbf{k}_{nz}^{<l>} &= \mathrm{mod}(1+lM+K_L,N_H):\mathrm{mod}(M_1+lM+K_L-1,N_H) \quad (4.43)\\ \mathbf{k}_{z}^{<l>} &= \mathrm{mod}(M_1+lM+K_L,N_H):\mathrm{mod}[(l+1)N_L+K_L,N_H] \quad (4.44) \end{aligned}$$

with $0 \le l \le Q-1$. Note that $\mathbf{k}_z^{<Q-1>}$ points to the subcarrier K_L, and thus cannot be considered as an interference free subcarrier. Detailed derivations of Eq. (4.43) and Eq. (4.44) are provided in Appendix E. Let B_G denotes the guard band between two type of signals, we can achieve the relationship between K_L and K_H as:

$$K_L = \begin{cases} K_H - M_1 - B_G, & \text{if} \quad K_L < K_H, \\ K_H + M_2 + B_G, & \text{if} \quad K_L > K_H. \end{cases} \tag{4.45}$$

By calculating the overlapping between $\{K_H, K_H+1, \cdots, K_H+M_2-1\}$ and $\mathbf{k}_z^{<l>}$ (which is simple when configurations of two numerologies have been fixed), the subcarriers of UE 2 that are free from the interference can be obtained. Thus, transmitting pilot signals only at interference-free subcarriers seems to be a more effective solution for CE performance improvement than interference cancellation. Nevertheless, this approach highly depends on the available interference-free subcarriers. The placement of pilot signals could be strictly constrained in some cases. For example, only $Q-1$ interference-free subcarriers left, *i.e.,* $\mathbf{k}_z^{<l>} = [K_L+N_L, K_L+2N_L, \cdots, K_L+(Q-1)N_L]$, when $K_1 = N_L$.

4.5 Numerical Results

In this section, simulation results for both the SU and MU scenarios are provided. Unless otherwise stated, the DFT points of UE 1 and the BS (and UE 2) are $N_H = 300$ and $N_L = 60$, respectively. The extended typical urban (ETU) channel defined by 3GPP is considered in all simulations. A normal CP (*i.e.*, 7% of the symbol length) is applied to maintain an acceptable system overhead.

4.5.1 Results for the SU Scenario

In Fig. 4.6, the relationships between PNR and different channel estimation methods are illustrated. By default, pilot signals are uniformly inserted into transmit signals with $L = 2$. According to the figure, we can see that simulated results and analytical ones are well aligned, which validates the effectiveness of our derivations in Section. 4.3. As expected, all MSE curves show a downward trend with increasing PNR irrespective of which CE method is used. We can also

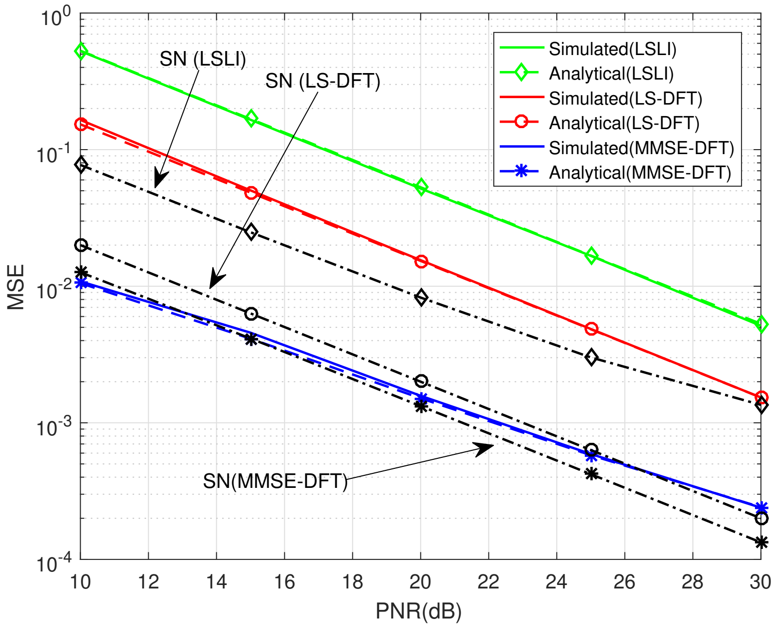

Figure 4.6: MSE of channel estimation v.s. PNR in the SU scenario. The green lines, red lines, and the blue lines corresponding to the results for LSLI, LS-DFT, and MMSE, respectively; while the black dash lines represent results in single-numerology scenarios.

find that even though configurations are mismatched between the transmitter and the receiver, MMSE-DFT still contributes to the best CE performance among the three. In addition, MSE of three CE methods in a single-numerology system, *i.e.*, traditional OFDM with ($Q = 1$), are illustrated in black dash lines as baseline performance. It is interesting to notice that compared to LSLI and LS-DFT, where the mismatched sampling rate significantly degrades the channel estimation performance, the performance of MMSE-DFT is almost untouched.

To investigate the impact of the pilot distance L, in Fig. 4.7, we present the MSE of the three CE methods against the pilot distance with 20 dB PNR. The most intuitive observation exhibited in the figure is that the parameter L affects performance differently for different CE methods. In particular, for LSLI, the appearance of $\mathbf{\Gamma}$ leads to an entirely different performance curve compared to the single numerology system: ϵ_L^{LL} grows with the pilot distance increasing when $Q = 1$. In contrast, it shows an opposite trend when $Q = 5$. As has been analyzed in Section. 4.3, the LSLI estimation error is jointly contributed by both linear interpolation (*i.e.*, α_L) and the noise (*i.e.*, β_L).

In Table. I and Table. II, exact values of α_L and β_L are illustrated with $Q = 1$ and $Q = 5$, respectively. We can see that in Table. I the noise-related error

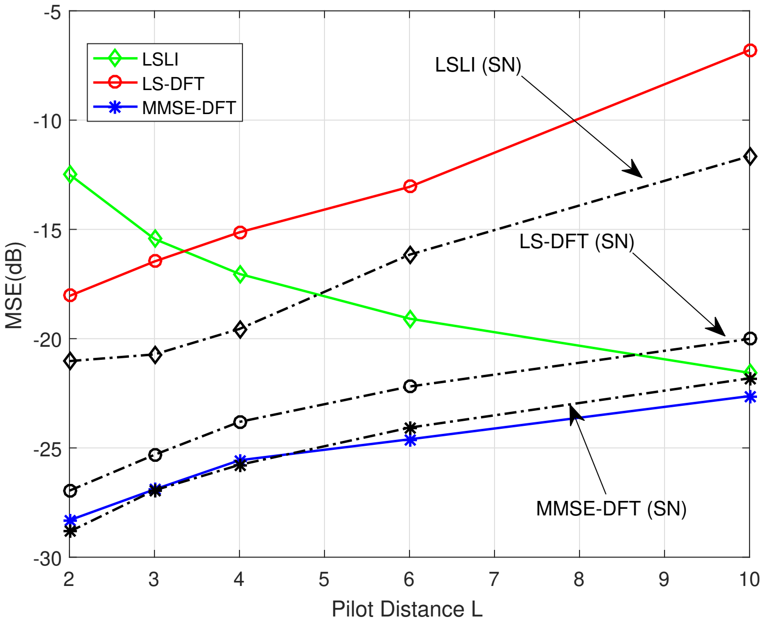

Figure 4.7: MSE of channel estimation (with the unit of dB) v.s. Pilot distance L in the SU scenario. The green line, red line, and the blue line corresponding to the result for LSLI, LS-DFT, and MMSE, respectively; while the black dash lines represent results in single-numerology scenarios.

Table 4.1: CE error component values for LSLI, $Q = 1$

Distance	2	3	4	6	10
α_L (dB)	-32.3	-26.6	-22.4	-16.8	-11.6
β_L (dB)	-21.2	-21.4	-21.5	-21.6	-21.6
ϵ_L^{LL} (dB)	-20.8	-20.3	-18.9	-15.6	-11.2

Table 4.2: CE error component values for LSLI, $Q = 5$

Distance	2	3	4	6	10
α_L (dB)	-60.1	-54.1	-49.6	-43.2	-34.6
β_L (dB)	-12.8	-15.2	-16.9	-19.1	-21.7
ϵ_L^{LL} (dB)	-12.8	-15.2	-16.9	-19.0	-21.5

remains unchanged with different L. Providing that the level of interpolation error is comparable to β_L, the variation of ϵ_L^{LL} shows the same trend as that of α_L. Relatively, noise plays the dominant role when $Q = 5$, and β_L decreases with L increasing because of $\mathbf{\Gamma}$. Hence, the variation of ϵ_L^{LL} shows a downward trend. In comparison, the variation of the red curve (*i.e.*, LS-DFT) and the blue curve (*i.e.*, MMSE-DFT) have the same trend as their single numerology counterparts. Among the three methods, MMSE-DFT not only shows the best channel estimation performance but also holds surprising robustness against the variation of L and Q.

In Section. 4.3, it is expected that the position of the pilot signals significantly affects the CE performance due to the impact of $\mathbf{\Gamma}$. To better understand the relationship between the pilot position and the channel estimation performance, we define $\mathbf{P}_L^{k_0}$ as the pilot position set with L and k_0 to be the pilot distance and the index of the first pilot signal, respectively. In Fig. 4.8, BER performance of the investigated SU mixed-numerology system is illustrated with different CE methods and pilot position sets: $\mathbf{P}_{12}^{1}$, $\mathbf{P}_{12}^{11}$, and $\mathbf{P}_{12}^{12}$. Also, results with the proposed pre-compensation method are added for comparison. MMSE channel equalization is implemented for all results to minimize the influence of data

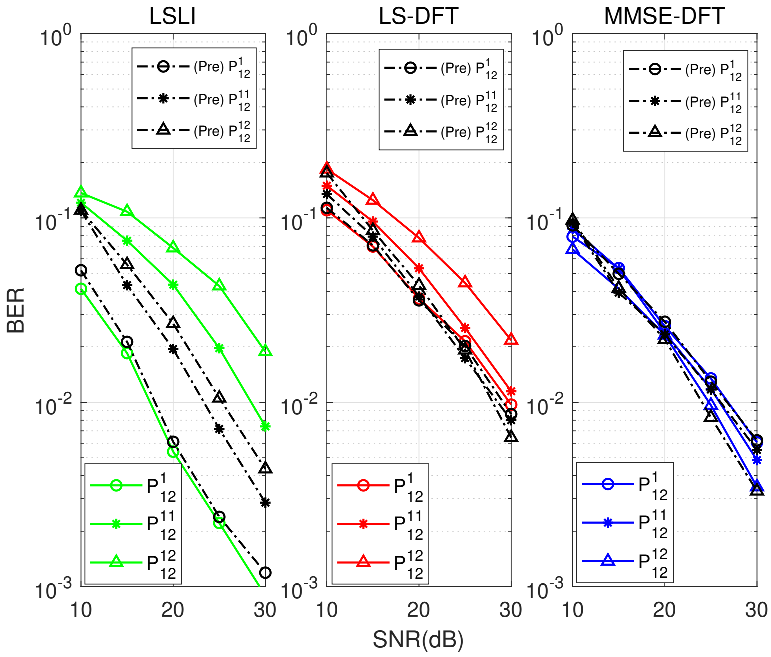

Figure 4.8: BER performance in the SU scenario with different CE methods and pilot position sets: $\mathbf{P}_{12}^{1} \in [1, 13, 25, 37, 49]$, $\mathbf{P}_{12}^{11} \in [11, 23, 35, 47, 59]$, and $\mathbf{P}_{12}^{12} \in [12, 24, 36, 48, 60]$. The results with pre-compensation are illustrated in black dash lines for comparison purpose.

detection. In addition, we assume the signal power of data and pilots is the same, *i.e.*, SNR = PNR. As can be seen, by implementing the proposed pilot placement principle, *i.e.*, to avoid the last few subcarriers in each PRB, the BER performance of $\mathbf{P}_{12}^{1}$ significantly outperforms $\mathbf{P}_{12}^{11}$ and $\mathbf{P}_{12}^{12}$ except for the case with MMSE-DFT. Furthermore, the pre-compensated pilot signal contributes to more clustered BER cures, which once again proves its effectiveness in mitigating the distortion caused by the sampling rate mismatch.

4.5.2 Results for the MU Scenario

As has been discussed in Section. 4.4, the result presented in this section is only for UE 2. In Fig. 4.9, the channel estimation error versus PNR of UE 2 (5 PRBs) is illustrated with and without the interference from UE 1 (1 PRB), where the guard band between them is $B_G = 3$. Pilot signals for UE 2 are placed in subcarriers indicated by $k_v = [1, 3, 5, \cdots, 59]$ with $L = 2$. As we can observe, the interference significantly degrades the channel estimation performance for LSLI and LS-DFT, especially in the high PNR region, where the error floor appears. In contrast, by taking advantage of the prior known information about the interference, MMSE-DFT CE maintains its good performance.

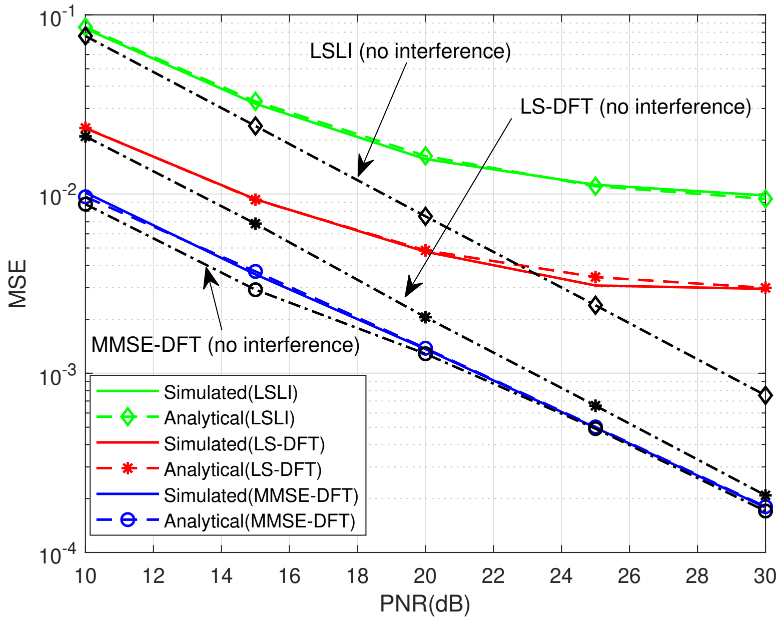

Figure 4.9: MSE of channel estimation v.s. PNR in the MU scenario. The green lines, red lines, and the blue lines corresponding to the results for LSLI, LS-DFT, and MMSE, respectively; while the black dash lines are the results in single-numerology system, *i.e.*, without interference.

Next, simulation results are provided to show how much performance improvement can be achieved by applying the proposed interference cancellation (IC) and interference free pilot placement (IF), respectively. Since the estimated channel and detected signal of UE 1 are needed for realizing the interference cancellation, we choose the most effective way to achieve $\hat{\mathbf{h}}_L$ and $\hat{\mathbf{x}}_L$ to minimize the influence of corresponding errors, *i.e.*, MMSE-DFT channel estimation with pilot distance being 2 (according to Fig. 4.7) and MMSE channel equalization. Besides, transmission configurations of UE 1 and UE 2 are as follows: $K_L = 1$, $M_1 = 12$ (1 PRB), $K_H = 24$, $M_1 = 120$ (10 PRBs). Based on Eq. (4.43), the interfered UE 2 subcarriers are indicated as $[39 : 49]$ and $[99 : 109]$. In such case, we implement two pilot position sets $\mathbf{P}^1_{12} = [1, 13, 25, 37, \underline{49}, 61, 73, 85, 97, \underline{109}]$ and $\mathbf{P}^2_{12} = [2, 14, 26, 38, 50, 62, 74, 86, 98, 110]$ for UE 2, so that $\mathbf{P}^1_{12}$ suffers from interference while $\mathbf{P}^2_{12}$ is not. Thus, $\mathbf{P}^2_{12}$ refers to the interference free pilot placement.

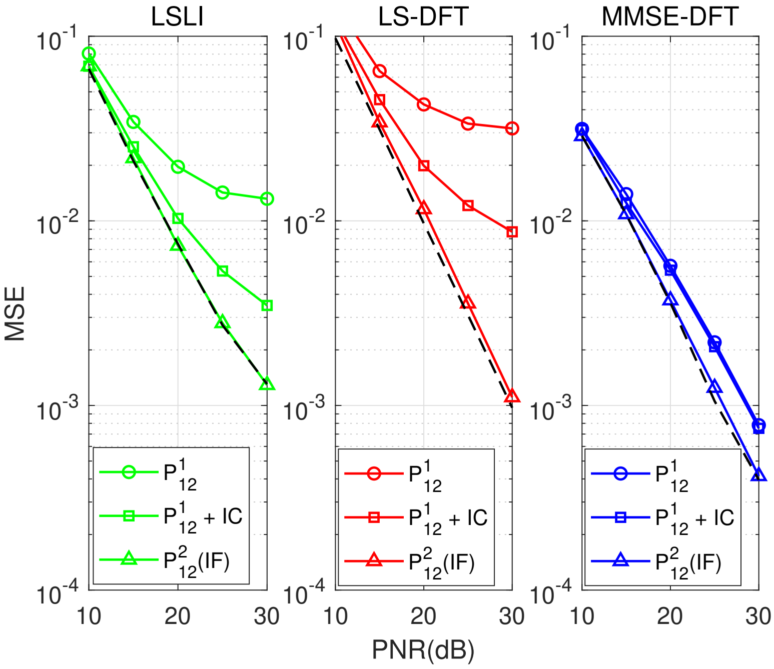

Figure 4.10: CE performance with interference cancellation (labeled as '$\mathbf{P}^1_{12}$ + IC') and interference free pilot transmission (labeled as '$\mathbf{P}^2_{12}$(IF)') in the MU scenario. The black dash lines are the results in the single-numerology system, *i.e.*, without interference.

Fig. 4.10 illustrates the MSE of different channel estimations by applying the two methods. Again, black dash lines are presented as baseline performance generated in the single numerology system. It can be found that IC decently reduces the MSE value except for MMSE-DFT, while IF leads to even better performances. In particular, at most 5.7 dB and 15.1 dB performance gain can be achieved by using IC and IF, respectively. As can be expected, IF completely eliminates the influence caused by the interference and generates comparable results to those in the single numerology system.

4.6 Conclusion

This chapter systematically investigates the uplink channel estimation of the SBDR mixed-numerology system. Three CE methods, *i.e.*, LSLI, LS-DFT, and MMSE-DFT, are implemented and theoretically analyzed in the proposed single-user and multi-user scenarios. The analysis reveals that the PNR, pilot distance, and position of pilot signals jointly affect the CE performance. A pre-compensation method is proposed to compensate for the negative effect of the signal distortion caused by the sampling rate mismatch. In addition, we propose an interference cancellation method based on the derived closed-form expression of the INI and demonstrate the existence of interference-free subcarriers. An interference-free pilot signal placement strategy is developed accordingly.

The work presented in this chapter can be regarded as the foundation of the channel estimation for mixed-numerology systems. It provides guidance on how to design the pilot signals efficiently in such kinds of systems, and it can be directly extended to include advanced wavforms such as windowed-OFDM [150] and filtered-OFDM [151]. By considering the CE analysis in this chapter, signal processing algorithms such as synchronization and channel equalization could be more pertinently developed to fit the mixed-numerology environment. Moreover, this work paves the way to establish a comprehensive framework for the RAN slicing system.

Chapter 5

Power Allocation in the Presence of Mixed-Numerology

5.1 Introduction

Network slicing is considered one of the most promising techniques for future wireless communications to support heterogeneous services efficiently [152]. Different services have disparate QoS requirements and always operate on various types of devices. Some of them require high data rate [153], others emphasize extremely low latency [154]. Besides, cost and energy efficiency are considered the first priority in designing IoT devices such as smart meters [155]. Meanwhile, mixed-numerology techniques forms the PHY foundations for network slicing. As has been discussed in Chapter 3, MN is categorized into four scenarios, i.e., SBSR, DBSR, SBDR and DBDR. During the past several years, DBSR (or BB-differed MN where only based SCS is different among numerologies) has been thoroughly investigated from different perspectives such as INI analysis [110, 115], PAPR reduction [120,122], and resource allocation [130,156]. On the other hand, a two-numerology framework is established in the context of SBDR (or RF-differed MN where only RF sampling rate is different among numerologies) scenario in this thesis, and channel equalization/interference cancellation algorithms are proposed. It is revealed that apart from being affected by the INI, sampling rate misalignment between the transmitter and receiver also results in the distortion of the signal. Consequently, it becomes outstandingly important to introduce an efficient subcarrier-level power allocation scheme in such kinds of systems to counter the performance degradation caused by the sampling rate mismatch.

To complete the puzzle of MN system investigations, an iterative convex approximation power allocation algorithm is implied in an RF-differed MN system to maximize the achievable system data rate. For the same reason as in Chapter

4, the investigation in this chapter focused on the uplink and the extension to downlink is straightforward. Subband filtering, *i.e.*, filtered OFDM, is considered for each numerology to restrain the INI[1]. The main contributions of this chapter are summarized as follows:

- A generalized RF-differed MN system model (with 'M' numerologies) is constructed considering subband filtering, and detailed digital domain signal processing chain is presented in the form of matrix notations;
- The power of the desired/interference signal and the noise is analytically investigated based on the system model, and the closed-form expression of SINR is derived.
- An iterative convex approximation power allocation algorithm is implemented to maximize the achievable system data rate, and its performance is compared with other schemes.

The rest of this chapter is organized as follows. In Section II, the generalized RF-differed MN system model is constructed. The mathematical derivations of desired signal, interference, noise, and SINR are provided in Section III. In the same Section, the power allocation algorithm is introduced. In Section IV, numerical results are presented. Finally, Section V concludes this chapter.

Notations: Uppercase and lowercase bold letters, *e.g.*, $\mathbf{A}$ and $\mathbf{a}$, to denote matrices and vectors, respectively. $\{\cdot\}^H$ represents the Hermitian conjugate, and $\{\cdot\}^T$ refers to transpose operation. $\mathcal{E}\{\mathbf{A}\}$ are used to express the expectation of $\mathbf{A}$. $\odot$ is applied as the point-wise multiplication. It should be noted that $\text{diag}\{\mathbf{A}\}$ means a vector formed by taking the diagonal elements of matrix $\mathbf{A}$, and $\text{diag}\{\mathbf{a}\}$ forms a diagonal matrix by taking each element of vector $\mathbf{a}$. $\mathbf{I}_M$ and $\mathbf{0}_{M\times N}$ denote an M-dimension identity matrix and an $M \times N$ zero matrix, respectively. Concerning the matrix combination, ',' is used to denote row combination and ';' denotes column combination.

5.2 System Model

Fig. 5.1 shows a typical uplink MN model with M numerologies represented by different colors of blocks, and each of them has a unique sampling rate. Without loss of generality, it is assumed that one user per numerology. Note that the numerology of the base station represents the system numerology, which could be the same as one of the user equipment. Hence, it is not counted into the number of numerologies. Denoting $S^{(i)}$ and $N^{(i)}$ as the sampling rate and DFT size of the UE i, while S^b and N^b as the sampling rate and DFT size of the BS (or system), respectively. Considering the same SCS for all numerologies, the configurations between the UE i and the BS can be related by:

---

[1] F-OFDM or W-OFDM is one of the most effective methods to maintain the MN system performance, especially for scenarios with plenty of numerologies.

$$\frac{N^b}{N^{(i)}} = \frac{S^b}{S^{(i)}} = Q^{(i)}, \tag{5.1}$$

where $Q^{(i)}$ is the upsampling rate. Generally, different numerologies could have independent physical layer configurations. However, it is assumed that $Q^{(i)} \in \mathbb{Z}^+$ to reduce the complexity of system design and to align with the 3GPP specification design.

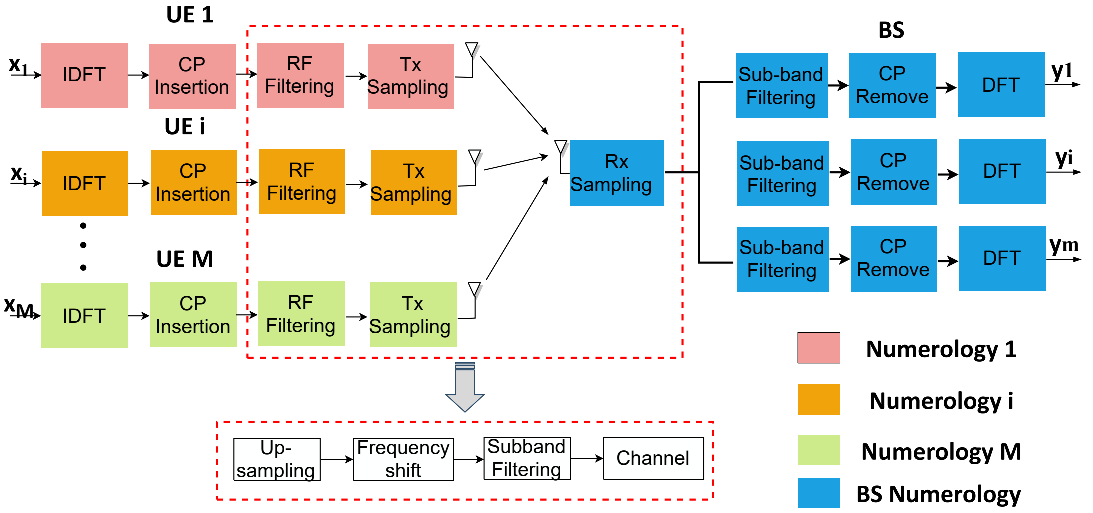
UE 1
x1
IDFT
CP Insertion
RF Filtering
Tx Sampling
UE i
xi
IDFT
CP Insertion
RF Filtering
Tx Sampling
UE M
xM
IDFT
CP Insertion
RF Filtering
Tx Sampling
Rx Sampling
BS
Sub-band Filtering
CP Remove
DFT
y1
Sub-band Filtering
CP Remove
DFT
yi
Sub-band Filtering
CP Remove
DFT
ym
Up-sampling
Frequency shift
Subband Filtering
Channel
Numerology 1
Numerology i
Numerology M
BS Numerology

Figure 5.1: Uplink model of an RF-differed mixed-numerology system. It composes of M numerologies in the Tx side and a BS numerology in the Rx side.

5.2.1 Transmitter Baseband Processing of Numerology i

The transmitter baseband processing of the numerology i is exactly the same as that of a legacy OFDM system, which includes IDFT operation and CP insertion. Denote $\mathbf{F}^{(i)} \in \mathbb{C}^{N^{(i)}\times N^{(i)}}$ as the $N^{(i)}$-points normalized IDFT matrix, whose element in the m-th row and n-th column is $\frac{1}{\sqrt{N^{(i)}}} \exp \frac{j2\pi mn}{N^{(i)}}$. Assuming $L_{cp}^{(i)}$ as the CP length of numerology i. The corresponding CP insertion matrix can be written as $\mathbf{C}^{(i)} \in \mathbb{Z}^{(N^{(i)}+L_{cp}^{(i)})\times N^{(i)}} = [\mathbf{0}_{L_{cp}^{(i)}\times(N^{(i)}-L_{cp}^{(i)})}, \mathbf{I}_{L_{cp}^{(i)}}; \mathbf{I}_{N^{(i)}}]$. If we indicate $\mathbf{d}^{(i)} \in \mathbb{C}^{K^{(i)}\times 1} = \{d_1^{(i)}, d_2^{(i)}, \cdots, d_{K^{(i)}}^{(i)}\}$ as the independent and identically distributed (i.i.d.) modulated data symbol vector, and $K^{(i)}$ as the number of subcarriers allocated to the i-th numerology, the CP-inserted OFDM symbol vector can be generated as:

$$\mathbf{x}^{(i)} \in \mathbb{C}^{(N^{(i)}+L_{cp}^{(i)})\times 1} = \mathbf{C}^{(i)}\mathbf{F}^{(i)}\mathbf{J}_t^{(i)}\mathbf{d}^{(i)}, \tag{5.2}$$

where matrix $\mathbf{J}_t^{(i)} = [\mathbf{I}_{K^{(i)}}; \mathbf{0}_{(N_i-K^{(i)},K^{(i)})}]$ is used to bridge each modulated data symbol to its corresponding column of $\mathbf{F}^{(i)}$.

5.2.2 Equivalent RF Processing and MN Multiplexing

To formulate the entire signal processing chain in the digital domain, an equivalent digital domain implementation is used to replace RF functionalities (as shown in the red dash box of Fig. 5.1). Specifically, a matrix $\mathbf{U}^{(i)}$ is implemented to perform the upsampling when the UE i signal arrives at the BS. With $L_{cp}^b = Q^{(i)}L_{cp}^{(i)}$ being the CP length after upsampling, matrix $\mathbf{U}^{(i)} \in \mathbb{Z}^{(N^b+L_{cp}^b)\times(N^{(i)}+L_{cp}^{(i)})}$ is formed as in Eq. (3.9). In addition, a diagonal frequency shifting matrix $\mathbf{\Phi}^{(i)} \in \mathbb{C}^{(N^b+L_{cp}^b)\times(N^b+L_{cp}^b)}$ is constructed for numerology i to move the signals to its assigned subcarriers. Assuming $\{K_0^{(i)}, K_0^{(i)}+1, \cdots, K_0^{(i)}+K^{(i)}-1\}$ indicate the $K^{(i)}$ subcarriers allocated to the numerology i, the k-th diagonal element of $\mathbf{\Phi}^{(i)}$ is calculated as:

$$\mathbf{\Phi}_k^{(i)} = e^{\frac{j2\pi(k-L_{cp}^b-1)(K_0^{(i)}-1)}{N^b}}. \tag{5.3}$$

It should be mentioned that the allocated subcarriers for each numerology are not overlapped with any others. The guard band between the i-th numerology and the j-th numerology is calculated as: $B_g = K_0^{(j)} - K_0^{(i)} - K^{(i)}$ for $K_0^{(j)} > K_0^{(i)}$.

In a normal F-OFDM system as in [151], signal $\mathbf{x}^{(i)}$ is due to be passed through a baseband filter. However, considering the processing bandwidth of numerology i is smaller than the system bandwidth, the filtering is carried out by RF units. In the derivation, the RF filter is replaced with an equivalent subband filter in the digital domain. Considering $L_{gt}^{(i)}$ as the filter length, the filter impulse responses are denoted as $\mathbf{g}_t^{(i)} = [\mathbf{g}_t^{(i)}(1), \mathbf{g}_t^{(i)}(2), \cdots, \mathbf{g}_t^{(i)}(L_{gt}^{(i)})]$. In theory, the filter tails will extend to the adjacent symbols and cause inter-symbol-interference. However, with properly designed filter and system frame structure, ISI can be negligible compared to the INI. Hence, ISI is not considered in the derivations and the focus is on the interference between the numerologies.

The last block of the equivalent process is to pass the signal through the channel. Define $\mathbf{h}^{(i)} = [\mathbf{h}^{(i)}(1), \mathbf{h}^{(i)}(2), \cdots, \mathbf{h}^{(i)}(L_h^{(i)})]$ as the i.i.d. multi-path fading channel impulse responses of numerology i, and the channel is power normalized as $\mathcal{E}\{\mathbf{h}^{(i)}(\mathbf{h}^{(i)})^H\} = 1$. The signal of numerology i before receiver baseband processing is expressed as:

$$\mathbf{s}^{(i)} \in \mathbb{C}^{(N^b+L^b_{cp})\times 1} = \mathcal{H}^{(i)}\mathcal{G}_t^{(i)}\mathbf{\Phi}^{(i)}\mathbf{U}^{(i)}\mathbf{x}^{(i)}, \tag{5.4}$$

where $\mathcal{H}^{(i)}$ and $\mathcal{G}_t^{(i)}$ are Toeplitz matrices, and their first columns and first rows are $[\mathbf{h}^{(i)}, \mathbf{0}_{1\times(N^b+L^b_{cp}-L_h^{(i)})}]^T$, $[\mathbf{g}_t^{(i)}, \mathbf{0}_{1\times(N^b+L^b_{cp}-L_{gt}^{(i)})}]^T$, and $[\mathbf{h}^{(i)}(1), \mathbf{0}_{1\times(N^b+L^b_{cp}-1)}]$, $[\mathbf{g}_t^{(i)}(1), \mathbf{0}_{1\times(N^b+L^b_{cp}-1)}]$, respectively.

In a BB-differed MN system (as in [110]), the various SCSs of numerologies imply their different symbol duration. Therefore, the multiplexing of them results in adjacent symbol overlapping. For example, the k-th symbol of the i-th numerology may overlap with the $(k+1)$-th symbol of the j-th numerology. In contrast, the investigated RF-differed MN system differentiates numerologies by their sampling rates only. As shown in Fig. 5.2, signals of three numerologies are illustrated in the time-frequency domain, and they cannot be distinguished from the symbol level. Hence, the multiplexing of them would not result in adjacent symbol overlapping. Moreover, the length of $\mathbf{s}^{(i)}$ only depends on BS configurations. We can achieve the multiplexed signal by simply combine $\mathbf{s}^{(1)}$ to $\mathbf{s}^{(M)}$ together:

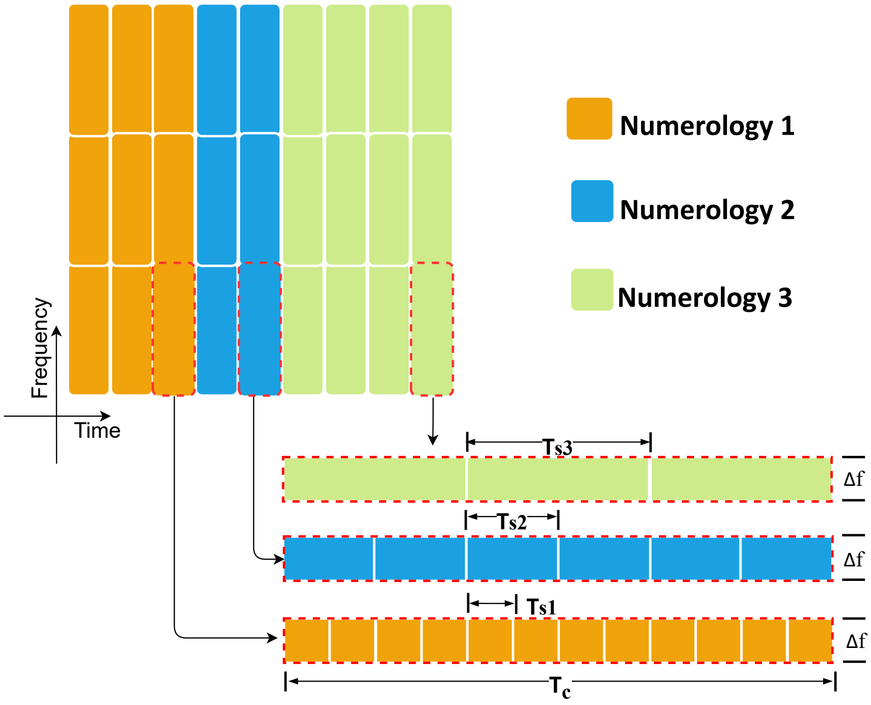

Figure 5.2: Example of mixed-numerology signal structure

$$\mathbf{s}^{m} \in \mathbb{C}^{(N^b+L^b_{cp})\times 1} = \sum_{i\in\mathcal{S}} \mathbf{s}^{(i)} + \mathbf{w}, \tag{5.5}$$

where $\mathbf{w}$ represents an additive white Gaussian noise vector with zero mean and σ^2 variance, and $\mathcal{S} = \{1, 2, \cdots, M\}$ is the set of all numerologies.

5.2.3 Receiver Baseband Processing of Numerology i

In the receiver, the multiplexed signal $\mathbf{s}^m$ is supposed to experience an inverse baseband processing to the transmitter so that the signal of the i-th numerology can be recovered.

Let us define $\mathbf{g}_r^{(i)} = [\mathbf{g}_r^{(i)}(1), \mathbf{g}_r^{(i)}(2), \cdots, \mathbf{g}_r^{(i)}(L_{gr}^{(i)})]$ as receiver filter impulse responses, where $L_{gr}^{(i)}$ is the filter length. In practice, the filter $\mathbf{g}_r^{(i)}$ should be independent with its counterpart in the transmitter (*i.e.*, $\mathbf{g}_t^{(i)}$) according to the 3GPP standardization that waveform should be transparent [143]. However, without loss of generality, matched filters are implemented in this chapter to make the expression compact and the extension is straightforward. Defining $\mathbf{R}^b \in \mathbb{Z}^{N^b \times (N^b + L_{cp}^b)} = [\mathbf{0}_{N^b \times L_{cp}^b}, \mathbf{I}_{N^b}]$ as the CP removal matrix, the isolated numerology i signal than be expressed in the following matrix form:

$$\mathbf{y}^{(i)} \in \mathbb{C}^{K^{(i)} \times 1} = \mathbf{J}_r^{(i)} (\mathbf{F}^b)^H \mathbf{R}^{(i)} \mathcal{G}_r^{(i)} \mathbf{s}^m, \tag{5.6}$$

where $\mathcal{G}_r^{(i)}$ is the Toeplitz matrix corresponding to $\mathbf{g}_r^{(i)}$; matrix $\mathbf{J}_r^{(i)} \in \mathbb{Z}^{K^{(i)} \times N^b}$ is used to collect the numerology i signal in the assigned subcarriers, and it can be written as:

$$\mathbf{J}_r^{(i)} = [\mathbf{0}_{(K^{(i)}, K_0^{(i)} - 1)}, \mathbf{I}_{K^{(i)}}, \mathbf{0}_{(K^{(i)}, N^b - K_0^{(i)} - K^{(i)} + 1)}]. \tag{5.7}$$

5.3 SINR Analysis and Signal Power Allocation

5.3.1 SINR Analysis

With regard to a normal OFDM system, the desired numerology i signal $\mathbf{y}_{\text{des}}^{(i)}$ can be easily extracted from the multiplexed signal $\mathbf{s}^m$ by the receiver DFT processing. However, different sampling rates among numerologies destroy the system orthogonality and result in INI within the system bandwidth. In the proposed MN system, Eq. (5.6) can be further written as:

$$\begin{aligned} \mathbf{y}^{(i)} &= \mathbf{y}_{\text{des}}^{(i)} + \mathbf{y}_{\text{INI}}^{(i)} + \mathbf{w}^{(i)} \\ &= \mathbf{J}_r^{(i)} (\mathbf{F}^b)^H \mathbf{R}^{(i)} \mathcal{G}_r^{(i)} \mathbf{s}^{(i)} + \mathbf{J}_r^{(i)} (\mathbf{F}^b)^H \mathbf{R}^{(i)} \mathcal{G}_r^{(i)} \sum_{j \in \mathcal{S}/i} \mathbf{s}^{(j)} \\ &+ \mathbf{J}_r^{(i)} (\mathbf{F}^b)^H \mathbf{R}^{(i)} \mathcal{G}_r^{(i)} \mathbf{w} \end{aligned} \tag{5.8}$$

By applying the G-CCP-US theorem in Eq. (5.8), the desired and interference signal in $\mathbf{y}^{(i)}$ can be separately written as:

$$\begin{aligned}\mathbf{y}_{\text{des}}^{(i)} &= \mathbf{J}_r^{(i)}\mathbf{G}_r^{(i)}\mathbf{H}^{(i)}\mathbf{G}_t^{(i)}\boldsymbol{\Gamma}^{(i)}\mathbf{J}_t^{(i)}\mathbf{d}^{(i)}, && (5.9)\\ \mathbf{y}_{\text{INI}}^{(i)} &= \mathbf{J}_r^{(i)}\mathbf{G}_r^{(i)}\sum_{j\in\mathcal{S}/i}\mathbf{H}^{(j)}\mathbf{G}_t^{(j)}\boldsymbol{\Gamma}^{(j)}\mathbf{J}_t^{(j)}\mathbf{d}^{(j)}, && (5.10)\end{aligned}$$

and the noise vector is simplified as:

$$\mathbf{w}^{(i)} = \mathbf{J}_r^{(i)}\mathbf{G}_r^{(i)}\mathbf{w}, \tag{5.11}$$

where $\mathbf{H}^{(i)} \in \mathbb{C}^{N^b\times N^b} = \sqrt{N^b}\text{diag}\{(\mathbf{F}^b)^H[\mathbf{h}^{(i)}, \mathbf{0}_{1\times(N^b-L_h^{(i)})}]^T\}$, $\mathbf{G}_t^{(i)} \in \mathbb{C}^{N^b\times N^b} = \sqrt{N^b}\text{diag}\{(\mathbf{F}^b)^H[\mathbf{g}_t^{(i)}, \mathbf{0}_{1\times(N^b-L_{gt}^{(i)})}]^T\}$, and $\mathbf{G}_r^{(i)} \in \mathbb{C}^{N^b\times N^b} = \sqrt{N^b}\text{diag}\{(\mathbf{F}^b)^H[\mathbf{g}_r^{(i)}, \mathbf{0}_{1\times(N^b-L_{gr}^{(i)})}]^T\}$ are the frequency response of multi-path channel, transmitter filter, and receiver filter of numerology i, respectively; $\boldsymbol{\Gamma}^{(i)} \in \mathbb{C}^{N^b\times K^{(i)}}$ is the signal distortion factor introduced by the sampling rate mismatch, which can be represented as:

$$\boldsymbol{\Gamma}^{(i)} = \boldsymbol{\Theta}^{(i)}\boldsymbol{\Lambda}^{(i)}. \tag{5.12}$$

Defining $\eta^{(i)} = K_0^{(i)} - 1$, we can write $\boldsymbol{\Theta}^{(i)} \in \mathbb{Z}^{N^b\times N^b}$ as $\boldsymbol{\Theta}^{(i)} = [\bar{\mathbf{I}}_{N^b}; \tilde{\mathbf{I}}_{N^b}]$, where $\bar{\mathbf{I}}_{N^b}$ and $\tilde{\mathbf{I}}_{N^b}$ are obtained by taking the last $\eta^{(i)}$ and the first $N^b - \eta^{(i)}$ rows of $\mathbf{I}_{N^b}$, respectively. Additionally, defining $\boldsymbol{v}_l^{(i)}$ as a $N^{(i)} \times N^{(i)}$ diagonal matrix with its k-th diagonal element being:

$$v_l^{(i)}(k) = \frac{1}{\sqrt{Q^{(i)}}}\sum_{m=1}^{Q^{(i)}} e^{\frac{-j2\pi(m-1)(k-1+lN^{(i)})}{N^b}}. \tag{5.13}$$

$\boldsymbol{\Lambda}^{(i)} \in \mathbb{C}^{N^b\times N^{(i)}}$ can be written as $\boldsymbol{\Lambda}^{(i)} = [\boldsymbol{v}_0; \boldsymbol{v}_1; \cdots; \boldsymbol{v}_{Q-1}]$.

Further define $\bar{\mathbf{G}}_r^{(i)}$, $\bar{\mathbf{H}}^{(i)}$, $\bar{\mathbf{G}}_t^{(i)}$, and $\bar{\boldsymbol{\Gamma}}^{(i)}$ as the $K^{(i)} \in \{K_0^{(i)}, K_0^{(i)}+1, \cdots, K_0^{(i)} + K^{(i)} - 1\}$ rows and first $K^{(i)}$ columns of $\mathbf{G}_r^{(i)}$, $\mathbf{H}^{(i)}$, $\mathbf{G}_t^{(i)}$, and $\boldsymbol{\Gamma}^{(i)}$, respectively; $\dot{\mathbf{G}}_r^{(j)}$, $\dot{\mathbf{H}}^{(j)}$, $\dot{\mathbf{G}}_t^{(j)}$, and $\dot{\boldsymbol{\Gamma}}^{(j)}$ are the $K^{(i)} \in \{K_0^{(i)}, K_0^{(i)} + 1, \cdots, K_0^{(i)} + K^{(i)} - 1\}$ rows and first $K^{(j)}$ columns of $\mathbf{G}_r^{(j)}$, $\mathbf{H}^{(j)}$, $\mathbf{G}_t^{(j)}$, and $\boldsymbol{\Gamma}^{(j)}$, respectively. Let $\mathbf{d}^{(i)} = \sqrt{\mathbf{p}^{(i)}} \odot \bar{\mathbf{d}}^{(i)}$, where $\mathbf{p}^{(i)} = \{p_1^{(i)}, p_2^{(i)}, \cdots, p_{K^{(i)}}^{(i)}\}^T$ is the symbol power allocation vector of numerology i, and $\bar{\mathbf{d}}^{(i)}$ denotes the normalized data symbol vector. The power of each component in $\mathbf{y}^{(i)}$ on the k-th subcarrier is written as:

$$\begin{aligned}
p^{(i)}_{\mathrm{des,k}} &= \mathcal{E}\{|y^{(i)}_{\mathrm{des,k}}|^2\} \\
&= \mathcal{E}\{|\bar{G}^{(i)}_{r,k}\bar{H}^{(i)}_k\bar{G}^{(i)}_{t,k}\bar{\Gamma}^{(i)}_k d^{(i)}_k|^2\} \\
&= |\bar{G}^{(i)}_{r,k}\bar{G}^{(i)}_{t,k}\bar{\Gamma}^{(i)}_k|^2 p^{(i)}_k, \qquad (5.14) \\
p^{(i)}_{\mathrm{INI},k} &= \mathcal{E}\{|y^{(i)}_{\mathrm{INI,k}}|^2\} \\
&= \mathcal{E}\{|\bar{G}^{(i)}_{r,k}\sum_{j\in\mathcal{S}/i}\dot{H}^{(j)}_k\dot{G}^{(j)}_{t,k}\dot{\Gamma}^{(j)}_k d^{(j)}_k|^2\} \\
&= \sum_{j\in\mathcal{S}/i}|\bar{G}^{(i)}_{r,k}\dot{G}^{(j)}_{t,k}\dot{\Gamma}^{(j)}_k|^2 p^{(j)}_k, \qquad (5.15) \\
p^{(i)}_{\mathrm{noise,k}} &= \mathcal{E}\{|w^{(i)}_k|^2\} = |\bar{G}^{(i)}_{r,k}|^2\sigma^2, \qquad (5.16)
\end{aligned}$$

where the subscript k refers to the k-th element/diagonal element of the corresponding vectors/matrices. Consequently, the SINR on the k-th subcarrier of numerology i be calculated as:

$$\begin{aligned}
\Upsilon^{(i)}_k &= \frac{p^{(i)}_{\mathrm{des,k}}}{p^{(i)}_{\mathrm{INI},k}+p^{(i)}_{\mathrm{noise,k}}} \\
&= \frac{|\bar{G}^{(i)}_{r,k}\bar{G}^{(i)}_{t,k}\bar{\Gamma}^{(i)}_k|^2 p^{(i)}_k}{\sum_{j\in\mathcal{S}/i}|\bar{G}^{(i)}_{r,k}\dot{G}^{(j)}_{t,k}\dot{\Gamma}^{(j)}_k|^2 p^{(j)}_k+|\bar{G}^{(i)}_{r,k}|^2\sigma^2}.
\end{aligned} \tag{5.17}$$

Removing the filter responses in Eq. (5.17) fits the SINR expression to an OFDM MN system. In that case, the SINR on each numerology i's subcarrier would only be decided by the distortion factor $\mathbf{\Gamma}$ given a fixed signal and noise power. By recalling the definition of $\mathbf{\Gamma}$, it is found that the interference generated from numerology j to numerology i mainly relates to the upsampling rate $(Q^{(i)}/Q^{(j)})$ and the spacing between their allocated subcarriers $|K^{(i)}_0 - K^{(j)}_0|$ (or equivalent to the guard band between them). In contrast, the filtering operation could significantly constrain the interference. We can therefore approximate the SINR as: $\tilde{\Upsilon}^{(i)}_k = \zeta|\bar{G}^{(i)}_{r,k}\bar{\Gamma}^{(i)}_k|^2$, where $\zeta = p^{(i)}_k/\sigma^2$ is a constant. Such an approximation reveals that the SINR distribution of numerology i's signal is determined by the combination of its transmitter filter response and the distortion factor.

5.3.2 Subcarrier-Level Power Allocation

Problem formulation

By considering continuous bit-loading, the achievable data rate of the i-th numerology is obtained as:

$$r^{(i)} = \sum_{k=1}^{K^{(i)}} \Delta f \log_2(1 + \Upsilon_k^{(i)}). \tag{5.18}$$

The achievable data rate of the entire system can be further calculated as:

$$r = \sum_{i \in \mathcal{S}} r^{(i)}, \tag{5.19}$$

As r is a function of $\mathbf{P} = \{\mathbf{p}^{(1)}; \mathbf{p}^{(2)}; \cdots; \mathbf{p}^{(M)}\}$, *i.e.*, the power allocation vector of all assigned subcarriers. We can formulate the following optimization problem to maximize the system achievable data rate subject to a given system power constraint P_{max}:

$$\begin{aligned} & \arg\max \quad r(\mathbf{P}) \\ s.t. \quad & \sum_{i \in \mathcal{S}} \sum_{k=1}^{K^{(i)}} p_k^{(i)} \leq P_{max}, \\ & p_k^{(i)} \geq 0, \quad \forall i \in \mathcal{S} \quad \& \quad \forall k \in [1, K^{(i)}]. \end{aligned} \tag{5.20}$$

Problem solution

Substitute Eq. (5.17) and Eq. (5.18) into Eq. (5.19) producing the following fully expended sum rate equation:

$$\begin{aligned} r(\mathbf{P}) &= \Delta f \sum_{i \in \mathcal{S}} \sum_{k=1}^{K^{(i)}} \log_2(1 + \Upsilon_k^{(i)}) \\ &= \Delta f \sum_{i \in \mathcal{S}} \sum_{k=1}^{K^{(i)}} \Big[\log_2(|H_{eq,k}^{(i)}|^2 p_k^{(i)} + \sum_{j \in \mathcal{S}/i} |H_{eq,k}^{(j \to i)}|^2 p_k^{(j)} + |\bar{G}_{r,k}^{(i)}|^2 \sigma^2) \\ &- \log_2(\sum_{j \in \mathcal{S}/i} |H_{eq,k}^{(j \to i)}|^2 p_k^{(j)} + |\bar{G}_{r,k}^{(i)}|^2 \sigma^2) \Big], \end{aligned} \tag{5.21}$$

where $H_{eq,k}^{(i)} = \bar{G}_{r,k}^{(i)} \bar{G}_{t,k}^{(i)} \bar{\Gamma}_k^{(i)}$ and $H_{eq,k}^{(j \to i)} = \bar{G}_{r,k}^{(i)} \dot{G}_{t,k}^{(j)} \dot{\Gamma}_k^{(j)}$ are used to simplify the notations. Eq. (5.21) reveals that the sum rate r is a difference of concave (d.c.) function of $\mathbf{P}$. Problems with d.c. structure objective functions have been proved to be NP-hard and it is difficult to find efficient solutions [157]. Fortunately, a bunch of approximated methods have been proposed during the past decades, such as the iterative water falling (IWF) approach [158], the low-complexity near-Optimal spectrum balancing approach [159], and the successive convex approximation for low complexity (SCALE) approach [160]. In particular, the SCALE approach is implemented to solve the optimization problem in Eq. (5.20) due to its low complexity and rapid convergence ability.

Specifically, a lower band $\alpha \log_2(\gamma) + \beta \leq \log_2(1+\gamma)$ is used to relax the problem, where

$$\begin{cases} \alpha = \frac{\gamma_0}{1+\gamma_0}, \\ \beta = \log_2(1+\gamma_0) - \frac{\gamma_0}{1+\gamma_0} \log_2 \gamma_0. \end{cases} \tag{5.22}$$

Such bound is tight with equality at a chosen value γ_0 when α and β are calculated as in Eq. (5.22). The relaxed objective function becomes:

$$\check{r}(\mathbf{P}) = \Delta f \sum_{i\in\mathcal{S}} \sum_{k=1}^{K^{(i)}} \left[\alpha^{(i)} \log_2(\Upsilon_k^{(i)}) + \beta^{(i)} \right], \tag{5.23}$$

where $\alpha^{(i)}$ and $\beta^{(i)}$ are constant values given a fixed $\mathbf{P}$. Moreover, substitute variable $2^{\bar{\mathbf{P}}}$ to replace $\mathbf{P}$ in Eq. (5.23) generating the following convex optimization problem:

$$\begin{aligned} &\arg\max \quad \check{r}(2^{\bar{\mathbf{P}}}) \\ s.t. \quad &\sum_{i\in\mathcal{S}} \sum_{k=1}^{K^{(i)}} 2^{p_k^{(i)}} \leq P_{max}. \end{aligned} \tag{5.24}$$

(5.24) is a standard concave maximization because the constraint is a sum of convex exponential terms, and the objective function is composed of the sum of $\log_2(\Upsilon_k^{(i)})$, which can be expended as a sum of linear and convex log-sum-exp terms [161]:

$$\log_2(\Upsilon_k^{(i)}) = 2\log_2 |H_{eq,k}^{(i)}| + \bar{p}_k^{(i)} - \left[\log_2 (\sum_{j\in\mathcal{S}/i} |H_{eq,k}^{(j\to i)}|^2 2^{\bar{p}_k^{(j)}} + |\bar{G}_{r,k}^{(i)}|^2 \sigma^2) \right]. \tag{5.25}$$

Therefore, a normal solution such as gradient-based method can be applied to solve $\bar{\mathbf{P}}^*$, and the optimal power allocation scheme is achieved as $\mathbf{P}^* = 2^{\bar{\mathbf{P}}^*}$.

By solving the problem in (5.24), we maximize a lower bound of the achievable sum-rate, and this lower bound can be iteratively tightened following Algorithm 1.

Algorithm 1 Iteration Algorithm for problem (5.20)

```
Input: initial power allocation vector $\mathbf{P}_0$, configurations of each numerology
    $\mathcal{C}^{(i)} = \{N^{(i)}, K^{(i)}, K_0^{(i)}, \mathbf{g}_t^{(i)}, \mathbf{g}_r^{(i)}\}$ for all $i \in \mathcal{S}$, and the noise power $\sigma^2$
Output: optimal power allocation scheme $\mathbf{P}^*$
    Initialization:
calculate $\mathbf{G}_r^{(i)}$, $\mathbf{G}_t^{(i)}$, and $\mathbf{\Gamma}^{(i)}$ for all $i \in \mathcal{S}$
set $n = 0$ as the iteration counter
$\mathbf{P}^{<n>} = \mathbf{P}_0$, $\bar{\mathbf{P}}^{<n>} = \log_2(\mathbf{P}^{<n>})$
    Allocation Procedure:
repeat
    update $\mathbf{\Upsilon}^{(i)}$ for all $i \in \mathcal{S}$ with Eq. (5.17)
    update $\alpha^{(i)}$ and $\beta^{(i)}$ for all $i \in \mathcal{S}$ with Eq. (5.22)
    obtain $\bar{\mathbf{P}}^{<n>}$ by solving optimization problem (5.24)
    update $\mathbf{P}^{<n>} = 2^{\bar{\mathbf{P}}^{<n>}}$
    $n \leftarrow n + 1$
until convergence
return $\mathbf{P}^* = \mathbf{P}^{<n>}$
```

5.4 Numerical Results

Table 5.1: Configurations of all numerologies

Parameters	UE 1	UE 2	UE 3	BS
Sampling rate (MHz)	0.36	0.72	0.9	3.6
SCS (kHz)	15	15	15	15
DFT size	24	48	60	240
Upsampling rate	10	5	4	
Assigned subcarriers	24	24	24	

In this section, the analytical derivations in Section. 5.3.1 are examined in the proposed MN system considering both OFDM and F-OFDM waveforms. In addition, the performance of the power allocation algorithm implemented in Section. 5.3.2 is demonstrated in terms of system spectrum efficiency. Table. 5.4 lists configurations of all numerologies considered in the simulations. The subcarriers of UE 1, UE 2, and UE 3 are placed from left to right alone the system bandwidth with a guard band B_g between each two of them. The ETU channel is considered in all simulations. A normal CP (*i.e.*, 7% of the symbol length) is applied to maintain an acceptable system overhead. With regard to the subband filtering, we implement the windowed *sinc* filter with the length being half of the symbol duration in the transmitter, and matched filters are used in the receiver for simplicity.

In Fig. 5.3, the SINR distributions of three numerologies are illustrated with different guard bands among them. The simulated results match with the analytical ones perfectly, which verifies the effectiveness of the derivations in Section. 5.3.1. It can be observed that the SINR distributions of three numerologies with OFDM waveform vary a lot with each other. Such dramatic results indicate that the three UEs experienced completely different interference. Increasing the guard band, *e.g.*, from 0.5 PRB (blue curves) to 1.5 PRB (yellow curves), cannot reduce the interference level. However, the varying B_g do cause the interference shifting among subcarriers. On the other hand, apparent SINR improvement can be found for all three numerologies with subband filtering. As has been analyzed in Section. 5.3.1, the SINR distribution of numerology i in F-OFDM is shaped by the transmitter filter and $\bar{\mathbf{\Gamma}}^{(i)}$. Therefore, the guard band is not an impact factor, and we only illustrate one SINR curve in F-OFDM with $B_g = 0.5$ PRB. It is interesting to notice that UE 1 has the most unevenly distributed SINR compared to UE 2 and UE 3, *i.e.*, large at the left-hand side and small at the other side. It comes from the largest upsampling rate of UE 1, which contributes to the most serious signal distortion. The results in Fig.5.3 inspire us to avoid mixing numerologies with large upsampling rates.

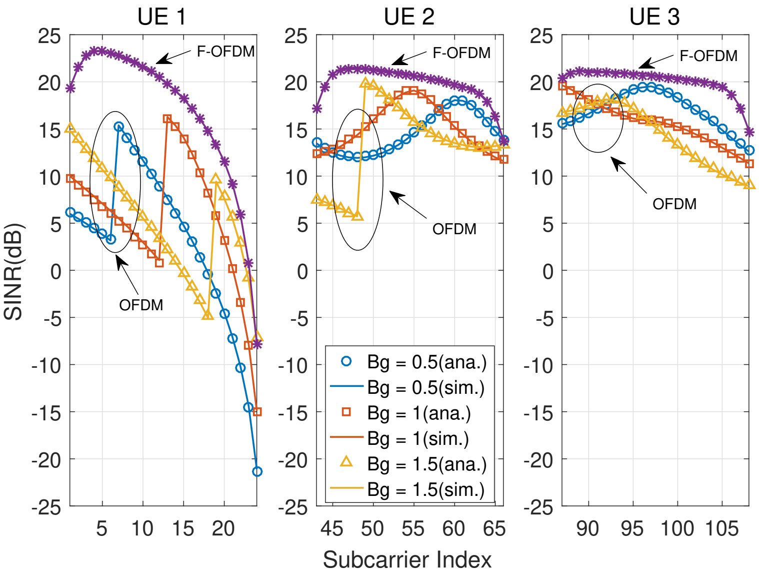

Figure 5.3: SINR distribution among subcarriers with $B_g = [0.5, 1, 1.5]$PRB. Both OFDM and F-OFDM waveforms are simulated for comparison. Signal power is evenly allocated to all symbols with $E_b/N_0 = 20$ dB.

Fig. 5.4 shows the BER v.s. E_b/N_0 results for the three numerologies. It is known from Fig. 5.3 that numerology 1 experiences the worst SINR among the three. Thereby we introduce a power offset ($\rho = \frac{\mathbf{p^{(1)}}}{\mathbf{p^{(2)}}} = \frac{\mathbf{p^{(1)}}}{\mathbf{p^{(3)}}}$) to improve its performance. In addition, convolutional code with 0.5 coding rate is adopted for performance improvement purposes. It can be observed that the power offset is able to balance the BER performance of three numerologies to a certain degree when no filtering is utilized (dotted cyan lines with square markers). However, in F-OFDM, the interference is filtered out whether power offset exists or not. Reducing the signal power of numerology 2 and numerology 3 can hardly improve the BER performance of numerology 1.

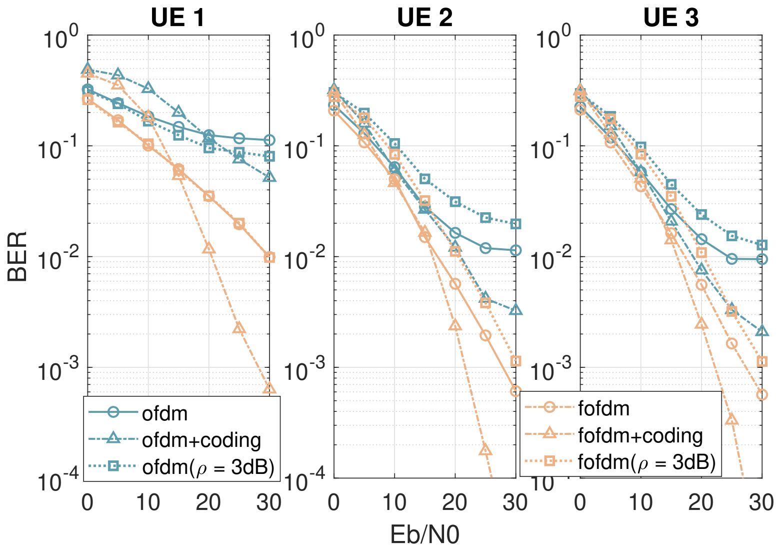

Figure 5.4: BER v.s. E_b/N_0 for each numerology by considering different configurations. The guard band is 1 PRB and the coding rate is 0.5. Signal power is evenly allocated in each $\mathbf{p}^{(\mathbf{i})}$, and the power offset is defined as $\rho = \frac{\mathbf{p}^{(\mathbf{1})}}{\mathbf{p}^{(\mathbf{2})}} = \frac{\mathbf{p}^{(\mathbf{1})}}{\mathbf{p}^{(\mathbf{3})}}$.

Fig. 5.5 compares the spectrum efficiency of the implemented power allocation algorithm in Section. 5.3.2 with other two schemes, *i.e.*, equal power allocation and IWF power allocation. In addition, the SE of the OFDM system without interference is considered as the benchmark. As expected, the proposed power allocation algorithm decently improves the SE of the OFDM MN system compared to the others especially in the interference-limited region. To be specific, with $E_b/N_0 = 27$dB, the proposed scheme outperforms the equal power allocation and IWF power allocation by 30% and 23%, respectively. Moreover, the coordination of subband filtering and the proposed scheme brings about a comparable result with the case that no interference and signal distortion appear. It further improves the system SE by almost 90% and 80% compared to the equal power allocation and IWF power allocation.

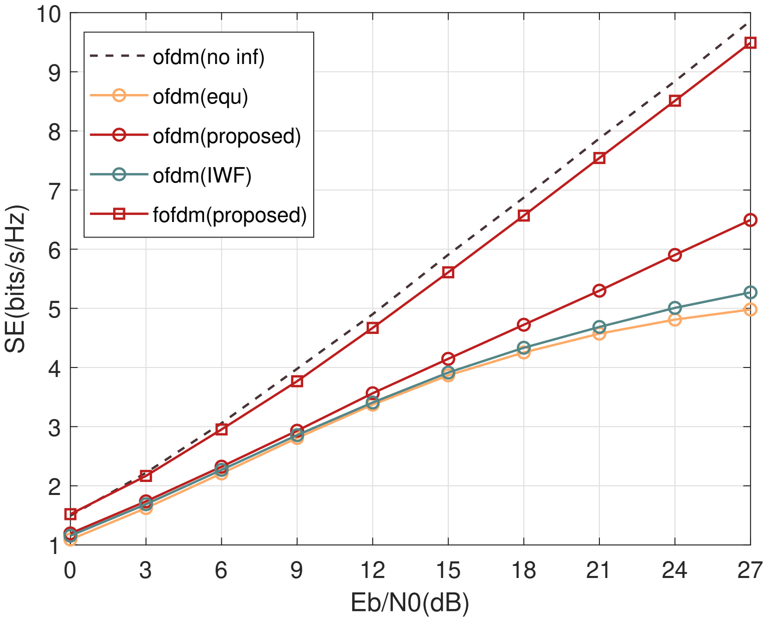

Figure 5.5: System spectrum efficiency versus E_b/N_0 with different power allocation schemes. In addition, the SE of a traditional single numerology OFDM system is presented as the benchmark.

5.5 Conclusion

In this chapter, a generalized RF-differed MN system model is developed in the presence of subband filtering. Based on the developed model, the closed-form expressions of desired/interference signal and noise power are derived as the function of numerology configurations. In addition, the expression of SINR is derived and analytically investigated. Moreover, an effective power allocation algorithm is implemented in the proposed system to maximize the achievable data rate. Numerical results verify the effectiveness of the derivations/analyses and the power allocation algorithm. The work in this chapter is an indispensable part of the MN system investigations, and it paves the way to establish a comprehensive framework for network slicing.

Chapter 6

Conclusions and Future Trends

Considering the promising application prospects of network slicing in future wireless communication networks, a profound cognition of its technical foundation in the physical layer, *i.e.*, mixed-numerology techniques, becomes particularly important. This thesis comprehensively investigated the mixed-numerology systems in framework construction, system parameters selection, and algorithm design. In this chapter, this thesis's main work and contributions are drawn, together with a brief discussion on the future trends of mixed-numerology investigations.

6.1 Conclusions

Future networks are expected to support the gradually increasing service and device types concurrently. For example, 5G includes three operation scenarios, each with quite different communication requirements such as data rate and latency, or deployment requirements such as deployment density and energy efficiency. Variety types of services (and their corresponding devices) associated with each operation scenario are needed to be supported in the same time. Instead of constructing a wireless network for each of them, both academia and industry believe that network slicing is the solution to support all service types in the same physical infrastructure efficiently. However, supporting services with different communication requirements and devices with different hardware constraints produces the so-called mixed-numerology systems, where interference and signal distortion are generated because of the baseband and radio frequency configurations mismatch among slices or between the transmitter and receiver. Consequently, the widely used signal processing algorithms and system design principles might be invalidated. It has profound significance to thoroughly investigate the mixed-numerology systems to build a concrete foundation for network slicing and future wireless networks.

In this context, this thesis comprehensively investigates the mixed-numerology systems from different perspectives. First, overviews of multiple access techniques, current radio access networks, and advanced waveforms are provided in Chapter 2. Meanwhile, a literature review of mixed-numerology sate-of-the-arts is presented, followed by the technical background. After that, the basis of this thesis is presented in Chapter 3. Since the conventional frame structure and the alignment of the resource grid are not valid in mixed-numerology systems, a new framework considering both baseband and RF configuration imparities is proposed, based on which mixed-numerology systems are divided into four categories: SBSR, SBDR, DBSR, DBDR. Thus, one can simply set up the parameter configurations for a desired multi-numerology system. Two theorems named G-CCP-US and C-CCP-DS are proposed to describe the unpaired DFT/IDFT processing caused by the RF configuration difference, which builds a theoretical foundation for signal isolation, collaboration and detection in such kinds of systems. With the proposed theorems, the most general mixed-numerology system (DBDR) is expressed mathematically in terms of signal transmission, which reveals the feasibility of one-tap channel equalization and indicates that the INIs among slices are linearly superposed in the receiver. In addition, power compensation and INI cancellation algorithms are proposed to encounter the signal distortion and interference. Simulation results are provided to verify the effectiveness of the proposed algorithms, which also show that 4-5 subcarriers' guardband between slices in F-OFDM based mixed-numerology systems can reduce INI to a negligible level. The work presented in this Chapter provides guidance for multi-numerology system design in terms of parameter and waveform selection, as well as the frame structure and algorithms design. Moreover, it presents a solution as to how the RAN slicing can be underpinned in the physical layer in a spectrum efficient way.

Next, uplink channel estimation of the mixed-numerology system is investigated in Chapter 4. In particular, to separately study the impact of INI and signal distortion on the channel estimation performance, two scenarios, *i.e.*, single-user and multi-user scenario, are proposed. Different combinations of estimation and interpolation methods, *i.e.*, least-square linear interpolation (denoted as LSLI), least-square '*sinc*' interpolation (denoted as LS-DFT), and minimum mean square error '*sinc*' interpolation (denoted as MMSE-DFT) are implemented and theoretically analyzed in both scenarios. The analysis reveals that the CE performance is jointly affected by pilot signal to noise ratio, pilot distance, and position of pilot signals. A pre-compensation method is proposed to compensate for the negative effect of the signal distortion caused by the sampling rate mismatch. In addition, an interference cancellation method based on the derived closed-form expression of the INI is proposed, and the existence of interference-free subcarriers is demonstrated. Based on the theoretical analysis in this Chapter, pilots placement principles are proposed for both single-user and multi-user scenarios. Again, simulation results show that the proposed algorithms and pilots placement principles contribute to considerable system performance improvement in terms of BER and channel estimation error. The work presented in this Chapter can be regarded as the foundation of the channel estimation for mixed-numerology systems. It provides guidance on how to design the pilot signals efficiently in such kinds of systems. Although it is based on the OFDM waveform, extensions are straightforward to include advanced wavforms such as windowed-OFDM and filtered-OFDM. By considering the CE analysis in this Chapter, signal processing algorithms such as synchronization and channel equalization could be more pertinently developed to fit the mixed-numerology environment. Moreover, this work paves the way to establish a comprehensive framework for the RAN slicing system.

Lastly, for the purpose to maximize the achievable rate of mixed-numerology systems, subcarrier level power allocation algorithms are investigated in Chapter 5. To achieve this goal, a generalized mixed-numerology system model with 'M' numerologies are constructed considering subband filtering, and a detailed digital domain signal processing chain is presented in the form of matrix notations. In addition, mathematical expressions of the desired/interference/noise signal and their power are derived as the function of numerology configurations, and the closed-form expression of SINR is presented. Moreover, an effective power allocation algorithm is implemented in the proposed system to maximize the achievable data rate. Numerical results verify the effectiveness of the derivations/analyses and the power allocation algorithm. The work in this Chapter paves the way to establish a comprehensive framework for network slicing.

6.2 Future Trends

6.2.1 Extension of Current Researches

Although a relatively comprehensive mixed-numerology framework together with system design guidance and some signal processing algorithms have been presented, there are a couple of limitations pertaining to the current researches.

In the following, some of these limitations are illustrated and potential extensions are discussed.

- This thesis focuses on the basic investigations of the mixed-numerology system, *e.g.*, framework construction, system design principles, and system performance evaluations, which forms the theoretical foundation for the mixed-numerology. On the other hand, the proposed signal processing methods such as the power compensation and INI cancellation algorithms in Chapter 3 and pilots placement strategy in Chapter 4 are designed in a less-complex way. In the next step, more advanced algorithms that lead to optimal system performance could be investigated.

- PAPR evaluations have been performed for DBSR mixed-numerology systems in several researches as discussed in Chapter 2. However, neither such researches nor this thesis studies the PAPR of the SBDR or DBDR mixed-numerology systems. Therefore, based on the proposed framework and system model in this thesis, PAPR in SBDR and DBDR mixed-numerology systems could be examined, and PAPR reduction approaches could be explored. Additionally, the investigations in this thesis are conducted for synchronized systems. An alternative extension could be the examination of asynchronous mixed-numerology systems.

- Researches in this thesis are based on mathematical analysis and simulations evaluation. Although a number of field experiments have been conducted in a test bed which is constructed by computers and universal software radio peripherals (USRPs), they are in a preliminary stage and not presented here. A meaningful study would be the compensation of the test bed to include all the features of a mixed-numerology system (such as different waveforms and parameter configurations), based on which the proposed algorithms and system design method could be examined in the real world.

6.2.2 Promising Future Directions

Without any doubt, the application of network slicing has a promising prospect in the future wireless communication networks. However, the potential of this technique has not been explored at the current stage where 5G is just come out and most of its assuring features are still under investigation. As the foundation of network slicing, mixed-numerology systems are necessary to be developed with the consideration of the important features in 5G and further wireless networks.

In the following, some of the promising research directions of mixed-numerology are discussed.

- Massive MIMO is definitely an indispensable part of the 5G technology which has the potential to largely improve the system throughput and capacity by exploring the spatial resource. When combining the massive MIMO with mixed-numerology, it could be interesting to figure out whether the current mixed-numerology investigations are valid or not. For instance, the interference generated from different slices may no longer linearly suppressed in the receiver because of the interactive MIMO links. On the other hand, it worth studying whether the characteristics of massive MIMO could be utilized to isolate the slices or to eliminate the INI.

- As is known that 5G reserves the OFDMA, which makes the application of low-complexity receiver possible in the cost of high synchronization requirement. However, the orthogonality of OFDM are destroyed in the presence of mixed-numerology, which inevitably degrades the system performance. Many advanced waveforms such as F-OFDM and W-OFDM are developed for 5G to reduce the OoBE and constrain the INI. Despite these waveforms are carefully designed, the system complexity are more or less increased, and the interference can only be mitigated instead of eliminated. In comparison, NOMA techniques provide an expectant solution for mixed-numerology systems. Specifically, there is no difference between single-numerology and mixed-numerology in NOMA based systems by isolating different slices in, *e.g.*, power domain.

- Recently, intelligent reflecting surface (IRS) has attracted extensive attention from wireless communication communities and is considered as a competitive technique in 6G due to its capability of shaping wireless propagation channels [162–164]. With the aid of IRS, the wireless channel becomes controllable to a certain extent instead of completely random. A potential utilization of IRS in mixed-numerology systems is the signal redirection, *i.e.*, only reflect the radio signal to its assigned users. Thus the interference from other slices could be minimized. This application is similar to the massive MIMO where spatial domain is adopted to separate slices. It is believed that mature IRS techniques could help to perfectly encounter the negative effects caused in mixed-numerology systems.

Appendix A

Generality Proof of the Two-Slice Model

The scenario with three slices is more realistic than the two-slice scenario. However, the multi-slice scenario (include the three-slice scenario) can be investigated based on the two-slice model. Because the desired signal detection is not affected by the number of slices, we can focus on the interference analysis in different models. Next, the proof is provided in two circumstances, respectively.

Circumstance 1 : large middle subband

According to the analysis in [109], the interference between different slices in a subband filtering based MN system mainly comes from a couple of adjacent subcarriers. The simulation results in Section. 3.6 can support this viewpoint as well. As can be seen from Fig. 3.5 and ig. 3.9, a guardband of 4 to 5 subcarriers can help to mitigate the INI to a negligible level. For a three-slices scenario as shown in Fig. A.1, where the subband bandwidth of the middle slice (slice 2) is wide enough, the INI that is generated between slice 1 and slice 3 can be ignored. Hence, for the two side slices, i.e., slice 1 and slice 3, they only suffer from the interference from the slice 2. For the slice 2, it suffers from the interference from both slice 1 and slice 3. If we define v_i as the received interference in the slice i's subband, and $v_{j,i}$ is the interference generated from slice j to slice i. We can write the interference model as:

$$v_1 \approx v_{2,1}, \quad v_2 = v_{1,2} + v_{3,2}, \quad v_3 \approx v_{2,3}. \tag{A.1}$$

It should be noted that each $v_{i,j}$ only depend on two slices, and its expression can be derived based on the proposed two-slice model. Although v_2 compose of two interference components: $v_{1,2}$ and $v_{3,2}$, they can be separately obtained by decoupling the three-slice model as two simple ones, i.e., slice 1-slice 2 and slice

2-slice 3.

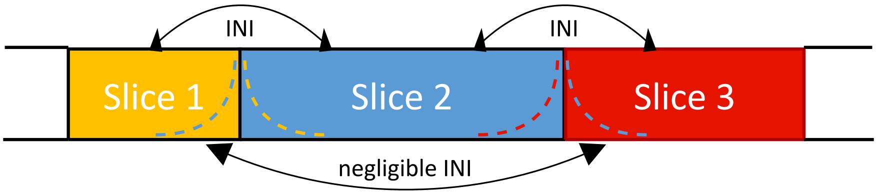

Figure A.1: Frequency band division for a MN system with three slices: slice1, slice2 and slice3. The bandwidth for slice2 is wide enough to prevent the interference between slice1 and slice3.

Circumstance 2 : small middle subband

On the other hand, if the subband bandwidth of slice2 is too narrow to prevent the INI between slice1 and slice3 (as shown in Fig. A.2), the interference model for each slice can be written as:

$$v_1 = v_{2,1} + v_{3,1}, \quad v_2 = v_{1,2} + v_{3,2}, \quad v_3 = v_{1,3} + v_{2,3}. \tag{A.2}$$

Similarly, the interference in each subband can be achieved by separately investigating its components. The only thing need to be noted is that the subband bandwidth of slice2 should be considered as the guardband while calculating the INI between slice1 and slice3 (i.e., $v_{1,3}$ and $v_{3,1}$).

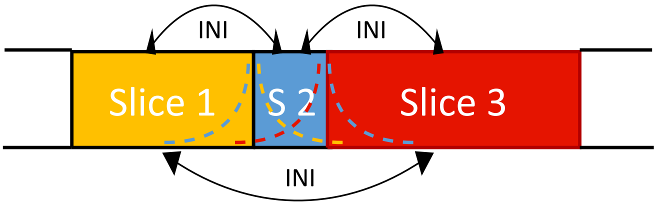

Figure A.2: Frequency band division for a MN system with three slices: slice1, slice2 and slice3. The bandwidth for slice2 is very small so that the slice1 and slice3 suffer from the INI generated by each other.

As is shown in Chapter. 5, the proposed system model can be generalized to N slices. Assume $i, j \in \mathbf{n} = \{1, 2, \cdots, N\}$, the interference model can be written as:

$$v_i = \sum_{j \in \mathbf{n}, j \neq i} v_{j,i}. \tag{A.3}$$

Because the interference generated from each slice can be linearly superposed, such an N slices model can be decoupled to $\frac{N(N-1)}{2}$ two-slice models.

Appendix B

Proof of Theorem 1

Firstly, by using $\mathbf{F}_N\mathbf{F}_N^H = \mathbf{I}_N$, we can write

$$\begin{aligned}\mathbf{H}_U =&\mathbf{F}_N^H\mathcal{H}\mathbf{\Phi}_\eta\mathbf{U}_Q\mathbf{F}_M \\ =&(\mathbf{F}_N^H\mathcal{H}\mathbf{F}_N)\cdot(\mathbf{F}_N^H\mathbf{\Phi}_\eta\mathbf{F}_N)\cdot(\mathbf{F}_N^H\mathbf{U}_Q\mathbf{F}_M).\end{aligned} \tag{B.1}$$

Since $\mathcal{H}$ is a circular matrix with the first column being $\mathbf{h}$, by using the original circular convolution property [30], we have $(\mathbf{F}_N^H\mathcal{H}\mathbf{F}_N) = \mathbf{H}_O$. Note that $\mathbf{\Phi}_\eta$ is a spectrum shifting matrix and by using Eq. (3.8), we have $\mathbf{F}_N^H\mathbf{\Phi}_\eta\mathbf{F}_N = \mathbf{\Theta}$.

Next, let us first divide the N-point DFT matrix $\mathbf{F}_N^H$ into Q equal size sub-matrices, each taking M consecutive rows of $\mathbf{F}_N^H$, i.e., $\mathbf{F}_N^H = [\mathbf{F}_N^H(0),\mathbf{F}_N^H(1),\cdots,\mathbf{F}_N^H(Q-1)]^T$. By using the structure information of the up-sampling matrix $\mathbf{U}_Q$, we have $(\mathbf{F}_N^H(l)\mathbf{U}_Q\mathbf{F}_M) = \frac{1}{\sqrt{Q}}\sum_{k=0}^{Q-1}\mathbf{F}_{M,k}^H(l)\mathbf{F}_M$, where $\mathbf{F}_{M,k}^H(l)$ is a sub-matrix of $\mathbf{F}_N^H(l)$ taking every M-th column of $\mathbf{F}_N^H(l)$, starting from the k-th column, i.e, taking the k-th, $(k+M)$-th, $\cdots$, $[k+(Q-1)M]$-th column of $\mathbf{F}_N^H(l)$. By using $\mathbf{F}_{M,k}^H(l) = \frac{1}{\sqrt{Q}}\mathbf{\Omega}_k(l)\mathbf{F}_M^H$, where $\mathbf{\Omega}_k(l)$ is a diagonal matrix with its i-th diagonal element being $e^{j\cdot 2\pi i(k+lM)/N}$, it is easy to obtain the i-th diagonal element of $\sum_{k=0}^{Q-1}\mathbf{F}_{M,k}^H(l)\mathbf{F}_M$ as

$$\sum_{k=0}^{Q-1} e^{j\cdot 2\pi i(k+lM)/N} = (1-e^{j\cdot i\epsilon_1})/(1-e^{j\cdot i\epsilon_2}) = \upsilon_l(i), \tag{B.2}$$

where $\epsilon_1 = 2\pi(Q+lM)/N$ and $\epsilon_2 = 2\pi(1+lM)/N$. Thus, we have $\mathbf{F}_N^H\mathbf{U}_Q\mathbf{F}_M = \mathbf{\Upsilon}$. Substituting into $\mathbf{H}_U$, we have Eq. (3.10). By using triangle equations, we obtain Eq. (3.14):

$$\begin{aligned}|\upsilon_l(i)|^2 =&|1-e^{j\cdot i\epsilon_1}|^2/|1-e^{j\cdot i\epsilon_2}|^2 \\ =&[1-2\cos(i\epsilon_1)]/[1-2\cos(i\epsilon_2)] \\ =&[\sin(i\epsilon_1/2)]^2/[\sin(i\epsilon_2)/2]^2\end{aligned} \tag{B.3}$$

Appendix C

Proof of Theorem 2

Firstly, by using $\mathbf{F}_N\mathbf{F}_N^H = \mathbf{I}_N$, we can write:

$$\mathbf{H}_D = (\mathbf{F}_M^H\mathbf{D}_Q\mathbf{F}_N) \cdot (\mathbf{F}_N^H\mathbf{\Phi}_\eta\mathbf{F}_N) \cdot (\mathbf{F}_N^H\mathcal{H}\mathbf{F}_N). \tag{C.1}$$

Similar to the proof to Theorem 1, we can easily achieve $\mathbf{H}_D = (\mathbf{F}_M^H\mathbf{D}_Q\mathbf{F}_N)\mathbf{\Theta}\mathbf{H}_O$. Let us first split the N-point IDFT matrix $\mathbf{F}_N$ into Q equal size sub-matrices, each taking M consecutive columns of $\mathbf{F}_N^H$, i.e., $\mathbf{F}_N = [\mathbf{F}_N(0), \mathbf{F}_N(1), \cdots, \mathbf{F}_N(Q-1)]$. Note that the down sampling matrix $\mathbf{D}_Q$ multiplying with $\mathbf{F}_N(l)$ equals to an M-dimension DFT matrix $1/\sqrt{Q}\mathbf{F}_M$, thus, $\mathbf{F}_M^H\mathbf{D}_Q\mathbf{F}_N(l) = 1/\sqrt{Q}\mathbf{I}_M$. Substituting into $\mathbf{H}_D$ we can obtain Eq. (3.19).

Appendix D

Proof of Eq. (3.27) and Eq. (3.28)

The desired signal at slice 1 can be written as

$$\mathbf{\Pi}_1(k) = \tilde{\mathbf{F}}_{N_{B1}}^H \mathbf{\Psi}_1^H \mathbf{R}_1 \mathcal{G}_1^H \bar{\mathcal{H}}_1 \mathcal{G}_1 \mathbf{C}_1 \mathbf{\Psi}_1 \tilde{\mathbf{F}}_{N_{U1}} \mathbf{G}_1(k). \tag{D.1}$$

With sufficient CP length and well-designed filter, we can omit the ISI as discussed in Section. 3.4.1. Then we can have

$$\begin{aligned} \mathbf{R}_1 \mathcal{G}_1^H \bar{\mathcal{H}}_1 \mathcal{G}_1 \mathbf{C}_1 =& (\mathbf{R}_1 \mathcal{G}_1^H \mathbf{C}_1)(\mathbf{R}_1 \bar{\mathcal{H}}_1 \mathbf{C}_1)(\mathbf{R}_1 \mathcal{G}_1 \mathbf{C}_1) \\ =& \mathbf{G}_{cir,1}^H \bar{\mathbf{H}}_{cir,1} \mathbf{G}_{cir,1}, \end{aligned} \tag{D.2}$$

where $\mathbf{G}_{cir,1}^H$, $\bar{\mathbf{H}}_{cir,1}$ and $\mathbf{G}_{cir,1}$ are circular matrix of receiver filter, channel and transmitter filter, respectively. Hence, $\mathbf{\Pi}_1(k)$ can be written as

$$\begin{aligned} \mathbf{\Pi}_1(k) =& (\tilde{\mathbf{F}}_{N_{B1}}^H \mathbf{\Psi}_1^H \mathbf{G}_{cir,1}^H \mathbf{\Psi}_1 \mathbf{F}_{N_{B1}}) \cdot (\mathbf{F}_{N_{B1}}^H \mathbf{\Psi}_1^H \mathbf{H}_{cir,1} \mathbf{\Psi}_1 \mathbf{F}_{N_{B1}}) \\ & \cdot (\mathbf{F}_{N_{B1}}^H \mathbf{\Psi}_1^H \mathbf{G}_{cir,1} \mathbf{\Psi}_1 \mathbf{F}_{N_{B1}}) \cdot (\mathbf{F}_{N_{B1}}^H \tilde{\mathbf{F}}_{N_{U1}}) \cdot \mathbf{G}_1(k) \\ =& 1/\sqrt{Q} \mathbf{G}_1^H \mathbf{H}_1 \mathbf{G}_1 \mathbf{G}_1(k) = \mathbf{H}_{eff,1} \mathbf{G}_1(k) \end{aligned} \tag{D.3}$$

and thus we have equation Eq. (3.27).

For slice 2, following the same approach, the desired signal can be written as

$$\begin{aligned} \mathbf{\Pi}_2 =& \tilde{\mathbf{F}}_{N_{B2}}^H \mathbf{\Psi}_2^H \bar{\mathbf{R}}_2 \mathcal{G}_2^H \bar{\mathcal{H}}_2 \mathcal{G}_2 \tilde{\mathbf{\Psi}}_2 \mathbf{U}_Q \bar{\mathbf{C}}_2 \mathbf{F}_{N_{U2}} \mathbf{G}_2 \\ =& \mathbf{G}_2^H \mathbf{H}_2 \mathbf{G}_2 \tilde{\mathbf{F}}_{N_{N2}}^H \mathbf{U}_Q \mathbf{F}_{N_{U2}} \mathbf{G}_2. \end{aligned} \tag{D.4}$$

By using Theorem 1, we can have $\mathbf{F}_{N_{B2}}^H \mathbf{U}_Q \mathbf{F}_{N_{U2}} = 1/\sqrt{Q}\mathbf{\Lambda}$. Hence, the desired signal at slice 2 can be achieved as $\mathbf{\Pi}_2 = \mathbf{H}_{eff,2}$, and thus equation Eq. (3.28) is obtained.

Appendix E

Derivation of Eq. (4.43) and Eq. (4.44)

Based on Eq. (4.30), we have $\mathbf{\Lambda}\mathbf{\Lambda}^H \in \mathbb{C}^{N_H \times N_H}$ as:

$$\begin{pmatrix} \mathbf{p}^{<0,0>} & \mathbf{p}^{<0,1>} & \cdots & \mathbf{p}^{<0,Q-1>} \\ \mathbf{p}^{<1,0>} & \mathbf{p}^{<1,1>} & \cdots & \mathbf{p}^{<1,Q-1>} \\ \vdots & \vdots & \ddots & \vdots \\ \mathbf{p}^{<Q-1,0>} & \mathbf{p}^{<Q-1,1>} & \cdots & \mathbf{p}^{<Q-1,Q-1>} \end{pmatrix}, \tag{E.1}$$

where $\mathbf{p}^{<l_1,l_2>} = \mathbf{v}_{l_1}\mathbf{v}_{l_2}^H$ $(0 \leq l_1, l_2 \leq Q-1)$ with its k-th $\in [1, N_L]$ diagonal element be:

$$\mathbf{p}^{<l_1,l_2>}(k) = \frac{(1 - e^{-j2\pi\frac{k-1+l_1N_L}{N_L}})(1 - e^{j2\pi\frac{k-1+l_2N_L}{N_L}})}{Q(1 - e^{-j2\pi\frac{k-1+l_1N_L}{N_H}})(1 - e^{j2\pi\frac{k-1+l_2N_L}{N_H}})}. \tag{E.2}$$

If we define $\bar{\mathbf{p}}^{<l_1,l_2>} \in \mathbb{C}^{N_L \times N_L}$ as:

$$\begin{pmatrix} \mathbf{p}^{<l_1,l_2>}(1) & 0 & \cdots & 0 & \cdots & 0 \\ 0 & \mathbf{p}^{<l_1,l_2>}(2) & \cdots & 0 & \cdots & 0 \\ \vdots & \vdots & \ddots & \vdots & \cdots & 0 \\ 0 & 0 & \cdots & \mathbf{p}^{<l_1,l_2>}(M_1) & \cdots & 0 \\ \vdots & \vdots & \ddots & \vdots & \ddots & \vdots \\ 0 & 0 & 0 & 0 & \cdots & 0 \end{pmatrix}. \tag{E.3}$$

It can be easily proved that $\bar{\mathbf{\Lambda}}\bar{\mathbf{\Lambda}}^H \in \mathbb{C}^{N_H \times N_H}$, and its expression can be represented as:

$$\begin{pmatrix} \bar{\mathbf{p}}^{<0,0>} & \bar{\mathbf{p}}^{<0,1>} & \cdots & \bar{\mathbf{p}}^{<0,Q-1>} \\ \bar{\mathbf{p}}^{<1,0>} & \bar{\mathbf{p}}^{<1,1>} & \cdots & \bar{\mathbf{p}}^{<1,Q-1>} \\ \vdots & \vdots & \ddots & \vdots \\ \bar{\mathbf{p}}^{<Q-1,0>} & \bar{\mathbf{p}}^{<Q-1,1>} & \cdots & \bar{\mathbf{p}}^{<Q-1,Q-1>} \end{pmatrix}. \tag{E.4}$$

Next, according to Eq. (4.29), we can have $\bar{\mathbf{\Theta}}_\eta = \bar{\mathbf{I}}_{N_H}\mathbf{\Theta}_\eta$, where $\bar{\mathbf{I}}_{N_H}$ is formed by taking $k \in \{K_H, K_H+1, \cdots, K_H+M_2-1\}$ rows of $\mathbf{I}_{N_H}$. Thus, we can have $\bar{\mathbf{\Theta}}_\eta\bar{\mathbf{\Lambda}}\bar{\mathbf{\Lambda}}^H\bar{\mathbf{\Theta}}_\eta^H = \bar{\mathbf{I}}_{N_H}\mathbf{\Theta}_\eta\bar{\mathbf{\Lambda}}\bar{\mathbf{\Lambda}}^H\mathbf{\Theta}_\eta^H\bar{\mathbf{I}}_{N_H}^H$.

The multiplication $\mathbf{\Theta}_\eta\bar{\mathbf{\Lambda}}\bar{\mathbf{\Lambda}}^H\mathbf{\Theta}_\eta^H$ is equivalent to shift the matrix $\bar{\mathbf{\Lambda}}\bar{\mathbf{\Lambda}}^H$ by η alone its diagonal line. Considering that $\bar{\mathbf{p}}^{<l_1,l_2>}(1) = 0$ for $l_1 = l_2 \neq 0$ and $\eta = K_L - 1$, the index of zero ($\mathbf{k}_z$) and non-zero ($\mathbf{k}_{nz}$) diagonal elements of $\mathbf{\Theta}_\eta\bar{\mathbf{\Lambda}}\bar{\mathbf{\Lambda}}^H\mathbf{\Theta}_\eta^H$ can be calculated as

$$\begin{aligned} \mathbf{k}_{nz}^{<l>} &= \mathrm{mod}(1 + lN_L + K_L, N_H) : \mathrm{mod}(K_1 + lN_L + K_L - 1, N_H), && \text{(E.5)} \\ \mathbf{k}_{z}^{<l>} &= \mathrm{mod}(K_1 + lN_L + K_L, N_H) : \mathrm{mod}[(l+1)N_L + K_L, N_H], && \text{(E.6)} \end{aligned}$$

where $0 \leq l \leq Q-1$. Go back to Eq. (4.42), $\mathbf{k}_z^{<l>}$ and $\mathbf{k}_{nz}^{<l>}$ also indicate the interference free and interfered subcarriers among the whole system bandwidth. Note that $\mathbf{k}_{nz}^{<0>}$ denotes subcarriers occupied by UE 1 signal.

Bibliography

[1] K. Tsagkaris, I. Gridabenyahia, A. Georgakopoulos, and P. Demestichas, "Emerging management challenges for the 5G era: Multi-service provision through optimal end-to-end resource slicing in virtualized infrastructures problem statements and solution approaches," in *Network Operations and Management Symposium (NOMS), 2016 IEEE/IFIP*. IEEE, 2016, pp. 1297–1300.

[2] H. Ji, S. Park, J. Yeo, Y. Kim, J. Lee, and B. Shim, "Ultra-reliable and low-latency communications in 5G downlink: Physical layer aspects," *IEEE Wireless Communications*, vol. 25, no. 3, pp. 124–130, JUNE 2018.

[3] "IMT Vision–Framework and overall objectives of the future development of IMT for 2020 and beyond," *Recommendation ITU M.2083-0*, 2015. [Online]. Available: https://www.itu.int/dms_pubrec/itu-r/rec/m/R-REC-M.2083-0-201509-I!!PDF-E.pdf

[4] A. Ijaz *et al.*, "Enabling massive IoT in 5G and beyond systems: PHY radio frame design considerations," *IEEE Access*, vol. 4, pp. 3322–3339, 2016.

[5] "Description of network slicing concept," *NGMN Alliance, white paper*, 2016, version 1.0.8. [Online]. Available: https://www.ngmn.org/wp-content/uploads/Publications/2016/161010_NGMN_Network_Slicing_framework_v1.0.8.pdf

[6] M. Richart, J. Baliosian, J. Serrat, and J.-L. Gorricho, "Resource slicing in virtual wireless networks: A survey," *IEEE Transactions on Network and Service Management*, vol. 13, no. 3, pp. 462–476, 2016.

[7] C. Liang and F. R. Yu, "Wireless network virtualization: A survey, some research issues and challenges," *IEEE Communications Surveys & Tutorials*, vol. 17, no. 1, pp. 358–380, 2015.

[8] Q. Li, G. Wu, A. Papathanassiou, and U. Mukherjee, "An end-to-end network slicing framework for 5G wireless communication systems," *arXiv preprint arXiv:1608.00572*, 2016.

[9] "5G white paper," *NGMN Alliance, white paper*, 2015, version 1.0. [Online]. Available: https://www.ramonmillan.com/documentos/bibliografia/NGMN5GWhitePaper_NGMNAlliance.pdf

[10] "View on 5G architecture," *5G PPP Architecture Working Group and others, White Paper, July*, 2016, version 3.0. [Online]. Available: https://5g-ppp.eu/wp-content/uploads/2020/02/5G-PPP-5G-Architecture-White-Paper_final.pdf

[11] K. Bonawitz, H. Eichner, W. Grieskamp, D. Huba, A. Ingerman, V. Ivanov, C. Kiddon, J. Konečnỳ, S. Mazzocchi, H. B. McMahan *et al.*, "Towards federated learning at scale: System design," *arXiv preprint arXiv:1902.01046*, 2019.

[12] X. Foukas, G. Patounas, A. Elmokashfi, and M. K. Marina, "Network slicing in 5G: Survey and challenges," *IEEE Communications Magazine*, vol. 55, no. 5, pp. 94–100, May 2017.

[13] R. H. Wen, G. Feng, W. Tan, N. Rui, W. Cao, and S. Qin, "Protocol stack mapping of software defined protocol for next generation mobile networks," *IEEE Transaction on Mobile Computing*, pp. 1651–1665, Jul. 2018.

[14] M. R. Sama, X. An, Q. Wei, and S. Beker, "Reshaping the mobile core network via function decomposition and network slicing for the 5g era," in *2016 IEEE Wireless Communications and Networking Conference.* Doha, Qatar, 2016, pp. 1–7.

[15] C. H. T. Arteaga, A. Ordoñez, and O. M. C. Rendon, "Scalability and performance analysis in 5g core network slicing," *IEEE Access*, vol. 8, pp. 142 086–142 100, 2020.

[16] H. Hawilo, A. Shami, M. Mirahmadi, and R. Asal, "NFV: state of the art, challenges, and implementation in next generation mobile networks (vEPC)," *IEEE Network*, vol. 28, no. 6, pp. 18–26, 2014.

[17] A. Basta, W. Kellerer, M. Hoffmann, H. J. Morper, and K. Hoffmann, "Applying NFV and SDN to LTE mobile core gateways, the functions placement problem," in *Proceedings of the 4th workshop on All things*

cellular: operations, applications, & challenges. Chicago Illinois, USA, 2014, pp. 33–38.

[18] X. Zhou, R. Li, T. Chen, and H. Zhang, "Network slicing as a service: enabling enterprises' own software-defined cellular networks," *IEEE Communications Magazine*, vol. 54, no. 7, pp. 146–153, 2016.

[19] H. Zhang, N. Liu, X. Chu, K. Long, A.-H. Aghvami, and V. C. Leung, "Network slicing based 5G and future mobile networks: mobility, resource management, and challenges," *IEEE Communications Magazine*, vol. 55, no. 8, pp. 138–145, 2017.

[20] P. Rost, A. Banchs, I. Berberana, M. Breitbach, M. Doll, H. Droste, C. Mannweiler, M. A. Puente, K. Samdanis, and B. Sayadi, "Mobile network architecture evolution toward 5G," *IEEE Communications Magazine*, vol. 54, no. 5, pp. 84–91, 2016.

[21] V.-G. Nguyen, A. Brunstrom, K.-J. Grinnemo, and J. Taheri, "SDN/NFV-based mobile packet core network architectures: A survey," *IEEE Communications Surveys & Tutorials*, vol. 19, no. 3, pp. 1567–1602, 2017.

[22] K. Sood, S. Liu, S. Yu, and Y. Xiang, "Dynamic access point association using software defined networking," in *2015 International Telecommunication Networks and Applications Conference (ITNAC).* Sydney, NSW, Australia, 2015, pp. 226–231.

[23] R. Kokku, R. Mahindra, H. Zhang, and S. Rangarajan, "NVS: A substrate for virtualizing wireless resources in cellular networks," *IEEE/ACM transactions on networking*, vol. 20, no. 5, pp. 1333–1346, 2011.

[24] "Network sharing; architecture and functional description (release 13)," 3GPP, Technical Specification (TS) 23.251, Mar 2015, version 13.1.0. [Online]. Available: https://www.3gpp.org/ftp/Specs/archive/23_series/23.251

[25] Y. Xiao, M. Krunz, and T. Shu, "Multi-operator network sharing for massive IoT," *IEEE Communications Magazine*, vol. 57, no. 4, pp. 96–101, 2019.

[26] O. Sallent, J. Perez-Romero, R. Ferrus, and R. Agusti, "On radio access network slicing from a radio resource management perspective," *IEEE Wireless Communications*, vol. 24, no. 5, pp. 166–174, 2017.

[27] A. Yazar and H. Arslan, “A flexibility metric and optimization methods for mixed numerologies in 5G and beyond,” *IEEE Access*, vol. 6, pp. 3755–3764, 2018.

[28] RAN1, “NR Physical Channels and Modulation.” 3GPP, Technical Specification (TS) 38.211, Sep 2018, version 15.3.0. [Online]. Available: https://www.3gpp.org/ftp/Specs/archive/38_series/38.211/

[29] Y. P. E. Wang, X. Lin, A. Adhikary, A. Grovlen, Y. Sui, Y. Blankenship, J. Bergman, and H. S. Razaghi, “A primer on 3GPP narrowband internet of things,” *IEEE Communications Magazine*, vol. 55, no. 3, pp. 117–123, March 2017.

[30] G. H. Golub and C. F. Van Loan, *Matrix Computations (3rd Ed.)*. Baltimore, MD, USA: Johns Hopkins University Press, 1996.

[31] A. Yazar and H. Arslan, “Flexible multi-numerology systems for 5G new radio,” *Journal of Mobile Multimedia*, vol. 14, no. 4, pp. 367–394, 2018.

[32] J. Choi, B. Kim, K. Lee, and D. Hong, “A transceiver design for spectrum sharing in mixed numerology environments,” *IEEE Transactions on Wireless Communications*, vol. 18, no. 5, pp. 2707–2721, May 2019.

[33] L. Zhang, A. Ijaz, J. Mao, P. Xiao, and R. Tafazolli, “Multi-service Signal Multiplexing and Isolation for Physical-Layer Network Slicing (PNS),” in *Vehicular Technology Conference (VTC-Fall), 2017 IEEE 86th.* Toronto, Canada, 2017, pp. 1–6.

[34] L. Zhang, A. Ijaz, P. Xiao, A. Quddus, and R. Tafazolli, “Subband filtered multi-carrier systems for multi-service wireless communications,” *IEEE Transactions on Wireless Communications*, vol. 16, no. 3, pp. 1893–1907, 2017.

[35] A. F. Molisch, *Wireless communications.* John Wiley & Sons, 2012, vol. 34.

[36] Z. Chen, Z. Ding, X. Dai, and R. Zhang, “An optimization perspective of the superiority of NOMA compared to conventional OMA,” *IEEE Transactions on Signal Processing*, vol. 65, no. 19, pp. 5191–5202, 2017.

[37] Y. Saito, Y. Kishiyama, A. Benjebbour, T. Nakamura, A. Li, and K. Higuchi, “Non-orthogonal multiple access (NOMA) for cellular future radio access,” in *2013 IEEE 77th vehicular technology conference (VTC Spring).* Dresden, Germany, 2013, pp. 1–5.

[38] L. Dai, B. Wang, Z. Ding, Z. Wang, S. Chen, and L. Hanzo, "A survey of non-orthogonal multiple access for 5G," *IEEE communications surveys & tutorials*, vol. 20, no. 3, pp. 2294–2323, 2018.

[39] S. Chen, B. Ren, Q. Gao, S. Kang, S. Sun, and K. Niu, "Pattern division multiple access—A novel nonorthogonal multiple access for fifth-generation radio networks," *IEEE Transactions on Vehicular Technology*, vol. 66, no. 4, pp. 3185–3196, 2016.

[40] A. J. Viterbi, "The History of Multiple Access and the Future of Multiple Services through Wireless Communication," 1999.

[41] V. H. Mac Donald, "Advanced mobile phone service: The cellular concept," *The bell system technical Journal*, vol. 58, no. 1, pp. 15–41, 1979.

[42] E. Zanoio and S. Urvik, "White Paper: CDMA Network Technologies: A Decade of Advances and Challenges," *Tektronix Inc. November*, 2003. [Online]. Available: https://download.tek.com/document/whitepaper_WP_CDMA.pdf

[43] D. Tse and P. Viswanath, *Fundamentals of wireless communication.* Cambridge university press, 2005.

[44] M. Cohn and A. Lempel, "On fast M-sequence transforms (Corresp.)," *IEEE Transactions on Information Theory*, vol. 23, no. 1, pp. 135–137, 1977.

[45] S. Tamura, S. Nakano, and K. Okazaki, "Optical code-multiplex transmission by gold sequences," *Journal of lightwave technology*, vol. 3, no. 1, pp. 121–127, 1985.

[46] A. M. Turkmani and U. Goni, "Performance evaluation of maximal-length, Gold and Kasami codes as spreading sequences in CDMA systems," in *Proceedings of 2nd IEEE International Conference on Universal Personal Communications*, vol. 2. Ottawa, Canada, 1993, pp. 970–974.

[47] A. J. Paulraj and C. B. Papadias, "Space-time processing for wireless communications," *IEEE signal processing magazine*, vol. 14, no. 6, pp. 49–83, 1997.

[48] A. Alexiou and M. Haardt, "Smart antenna technologies for future wireless systems: trends and challenges," *IEEE communications Magazine*, vol. 42, no. 9, pp. 90–97, 2004.

[49] R. A. Soni, R. M. Buehrer, and R. D. Benning, "Intelligent antenna system for cdma2000," *IEEE Signal Processing Magazine*, vol. 19, no. 4, pp. 54–67, 2002.

[50] B. Li, D. Xie, S. Cheng, J. Chen, P. Zhang, W. Zhu, and B. Li, "Recent advances on TD-SCDMA in China," *IEEE Communications Magazine*, vol. 43, no. 1, pp. 30–37, 2005.

[51] L. Lu, G. Y. Li, A. L. Swindlehurst, A. Ashikhmin, and R. Zhang, "An overview of massive MIMO: Benefits and challenges," *IEEE journal of selected topics in signal processing*, vol. 8, no. 5, pp. 742–758, 2014.

[52] E. G. Larsson, O. Edfors, F. Tufvesson, and T. L. Marzetta, "Massive MIMO for next generation wireless systems," *IEEE communications magazine*, vol. 52, no. 2, pp. 186–195, 2014.

[53] R. Nogueroles, M. Bossert, A. Donder, and V. Zyablov, "Improved performance of a random OFDMA mobile communication system," in *VTC'98. 48th IEEE Vehicular Technology Conference. Pathway to Global Wireless Revolution (Cat. No. 98CH36151)*, vol. 3. Ottawa, Canada, 1998, pp. 2502–2506.

[54] D. S. Sesia, M. M. Baker, and M. I. Toufik, *LTE: The UMTS Long Term Evolution: from Theory to Practice*, 2nd ed. Wiley-Blackwell, 2011.

[55] M. F. L. Abdullah and A. Yonis, "Performance of LTE Release 8 and Release 10 in wireless communications," in *Proceedings Title: 2012 International Conference on Cyber Security, Cyber Warfare and Digital Forensic (CyberSec)*. Kuala Lumpur, Malaysia, 2012, pp. 236–241.

[56] "Evolved Universal Terrestrial Radio Access (E-UTRA) Physical channels and modulation," TS 36.211 v.13.2.0, 3GPP RAN1, 2016. [Online]. Available: https://www.3gpp.org/ftp/Specs/archive/36_series/36.211

[57] S. Parkvall, E. Dahlman, A. Furuskar, Y. Jading, M. Olsson, S. Wanstedt, and K. Zangi, "LTE-advanced-evolving LTE towards IMT-advanced," in *2008 IEEE 68th Vehicular Technology Conference*. Calgary, Canada, 2008, pp. 1–5.

[58] S. Abeta, "Toward LTE commercial launch and future plan for LTE enhancements (LTE-Advanced)," in *2010 IEEE International Conference on Communication Systems*. Singapore, 2010, pp. 146–150.

[59] J. Oh and Y. Han, "Cell selection for range expansion with almost blank subframe in heterogeneous networks," in *2012 IEEE 23rd International Symposium on Personal, Indoor and Mobile Radio Communications-(PIMRC)*. Sydney, Australia, 2012, pp. 653–657.

[60] F. Qamar, K. B. Dimyati, M. N. Hindia, K. A. B. Noordin, and A. M. Al-Samman, "A comprehensive review on coordinated multi-point operation for LTE-A," *Computer Networks*, vol. 123, pp. 19–37, 2017.

[61] Y. Wang and K. I. Pedersen, "Performance analysis of enhanced inter-cell interference coordination in LTE-Advanced heterogeneous networks," in *2012 IEEE 75th Vehicular Technology Conference (VTC Spring)*. Yokohama, Japan, 2012, pp. 1–5.

[62] K. I. Pedersen, Y. Wang, S. Strzyz, and F. Frederiksen, "Enhanced inter-cell interference coordination in co-channel multi-layer LTE-advanced networks," *IEEE Wireless Communications*, vol. 20, no. 3, pp. 120–127, 2013.

[63] F. Xia, L. T. Yang, L. Wang, and A. Vinel, "Internet of things," *International journal of communication systems*, vol. 25, no. 9, p. 1101, 2012.

[64] K. Ashton *et al.*, "That 'internet of things' thing," *RFID journal*, vol. 22, no. 7, pp. 97–114, 2009.

[65] L. Atzori, A. Iera, and G. Morabito, "The internet of things: A survey," *Computer networks*, vol. 54, no. 15, pp. 2787–2805, 2010.

[66] "Ericsson Mobility Report on the Pulse of the Network Society," Telefonaktiebolaget L. M. Ericsson, Tech. Rep., Jun 2016. [Online]. Available: https://www.ericsson.com/assets/local/mobility-report/documents/2016/ericsson-mobility-report-june-2016.pdf

[67] "NarrowBand IoT Wide Range of Opportunities," Huawei Technologies Co., Ltd., Tech. Rep., Feb 2016. [Online]. Available: http://www-file.huawei.com/{~}/media/CORPORATE/minisite/mwc2016/pdf/NarrowBand-IoT-Wide-Range-of-Opportunities-en.pdf?la=en

[68] "Evolved Universal Terrestrial Radio Access (E-UTRA) NB-IOT Technical Report for BS and UE radio transmission and reception." 3rd Generation Partnership Project (3GPP), Technical Report (TR) 36.802, Jun 2016,

version 13.0.0. [Online]. Available: http://www.3gpp.org/ftp/Specs/archive/36_series/36.802/

[69] G. J. González, F. H. Gregorio, and J. Cousseau, "Interference analysis in the LTE and NB-IoT uplink multiple access with RF impairments," in *2018 IEEE 23rd International Conference on Digital Signal Processing (DSP).* Shanghai, China, 2018, pp. 1–4.

[70] S. Liu, L. Xiao, Z. Han, and Y. Tang, "Eliminating NB-IoT interference to LTE system: A sparse machine learning-based approach," *IEEE Internet of Things Journal*, vol. 6, no. 4, pp. 6919–6932, 2019.

[71] K. Shi, Y. Zhou, B. Kelleci, T. W. Fischer, E. Serpedin, and A. lker Karsilayan, "Impacts of narrowband interference on OFDM-UWB receivers: Analysis and mitigation," *IEEE Transactions on Signal Processing*, vol. 55, no. 3, pp. 1118–1128, 2007.

[72] D. Darsena and F. Verde, "Successive NBI cancellation using soft decisions for OFDM systems," *IEEE Signal Processing Letters*, vol. 15, pp. 873–876, 2008.

[73] B. Tan, J. Lu, J. Wu, D. Zhang, and Z. Zhang, "Toward a network slice design for ultra high definition video broadcasting in 5G," *IEEE Wireless Communications*, vol. 25, no. 4, pp. 88–94, 2018.

[74] J. Chakareski, "VR/AR immersive communication: Caching, edge computing, and transmission trade-offs," in *Proceedings of the Workshop on Virtual Reality and Augmented Reality Network.* Los Angeles, USA, 2017, pp. 36–41.

[75] A. Anand and G. de Veciana, "Resource allocation and HARQ optimization for URLLC traffic in 5G wireless networks," *IEEE Journal on Selected Areas in Communications*, vol. 36, no. 11, pp. 2411–2421, 2018.

[76] Z. Li, M. A. Uusitalo, H. Shariatmadari, and B. Singh, "5G URLLC: Design challenges and system concepts," in *2018 15th International Symposium on Wireless Communication Systems (ISWCS).* Lisbon, Portugal, 2018, pp. 1–6.

[77] E. Dahlman, S. Parkvall, and J. Skold, *5G NR: The next generation wireless access technology.* Academic Press, 2020.

[78] N. Al-Falahy and O. Y. Alani, "Millimetre wave frequency band as a candidate spectrum for 5G network architecture: A survey," *Physical Communication*, vol. 32, pp. 120–144, 2019.

[79] "NR User Equipment (UE) Radio Transmission and Reception Part 1: Range 1 Standalone," 3GPP RAN4, Technical Specification (TS) 38.101, Jun 2018, version 15.2.0. [Online]. Available: https://www.3gpp.org/ftp/Specs/archive/38_series/38.101-1/

[80] T. L. Marzetta, *Fundamentals of massive MIMO.* Cambridge University Press, 2016.

[81] B. Farhang-Boroujeny, "Ofdm versus filter bank multicarrier," *IEEE signal processing magazine*, vol. 28, no. 3, pp. 92–112, 2011.

[82] X. Zhang, M. Jia, L. Chen, J. Ma, and J. Qiu, "Filtered-ofdm - enabler for flexible waveform in the 5th generation cellular networks," in *2015 IEEE Global Communications Conference (GLOBECOM).* San Diego, USA, 2015, pp. 1–6.

[83] X. Zhang, L. Zhang, P. Xiao, D. Ma, J. Wei, and Y. Xin, "Mixed numerologies interference analysis and inter-numerology interference cancellation for windowed ofdm systems," *IEEE Transactions on Vehicular Technology*, 2018.

[84] L. Zhang, A. Farhang, G. Feng, and O. Onireti, *Radio Access Network Slicing and Virtualization for 5G Vertical Industries.* John Wiley & Sons, 2020.

[85] D. Demmer, R. Gerzaguet, J.-B. Doré, D. Le Ruyet, and D. Kténas, "Block-Filtered OFDM: a novel waveform for future wireless technologies," in *2017 IEEE International Conference on Communications (ICC).* Paris, France, 2017, pp. 1–6.

[86] G. Fettweis, M. Krondorf, and S. Bittner, "GFDM-generalized frequency division multiplexing," in *VTC Spring 2009-IEEE 69th Vehicular Technology Conference.* Barcelona, Spain, 2009, pp. 1–4.

[87] Y. Chen, F. Schaich, and T. Wild, "Multiple access and waveforms for 5G: IDMA and universal filtered multi-carrier," in *IEEE Vehicular Technology Conference (VTC Spring).* Seoul, Korea (South), 2014, pp. 1–5.

[88] A. Ikhlef and J. Louveaux, "Per subchannel equalization for MIMO FBMC/OQAM systems," in *2009 IEEE Pacific Rim Conference on Communications, Computers and Signal Processing.* Victoria, Canada, 2009, pp. 559–564.

[89] N. Michailow, M. Matthé, I. S. Gaspar, A. N. Caldevilla, L. L. Mendes, A. Festag, and G. Fettweis, "Generalized frequency division multiplexing for 5th generation cellular networks," *IEEE Transactions on Communications*, vol. 62, no. 9, pp. 3045–3061, 2014.

[90] "3gpp tsg ran wg1 meeting #86," Gothenburg, Sweden, 2016. [Online]. Available: https://www.3gpp.org/ftp/tsg_ran/WG1_RL1/TSGR1_86/Report

[91] T. Levanen, J. Pirskanen, K. Pajukoski, M. Renfors, and M. Valkama, "Transparent Tx and Rx waveform processing for 5G new radio mobile communications," *IEEE Wireless Communications*, vol. 26, no. 1, pp. 128–136, 2018.

[92] E. Bala, J. Li, and R. Yang, "Shaping spectral leakage: A novel low-complexity transceiver architecture for cognitive radio," *IEEE Vehicular Technology Magazine*, vol. 8, no. 3, pp. 38–46, 2013.

[93] S.-Y. Lien, S.-L. Shieh, Y. Huang, B. Su, Y.-L. Hsu, and H.-Y. Wei, "5G new radio: Waveform, frame structure, multiple access, and initial access," *IEEE communications magazine*, vol. 55, no. 6, pp. 64–71, 2017.

[94] R. Zayani, Y. Medjahdi, H. Shaiek, and D. Roviras, "WOLA-OFDM: A potential candidate for asynchronous 5G," in *2016 IEEE Globecom Workshops (GC Wkshps)*, Washington, USA, 2016, pp. 1–5.

[95] E. Güvenkaya, E. Bala, R. Yang, and H. Arslan, "Time-asymmetric and subcarrier-specific pulse shaping in OFDM-based waveforms," *IEEE Transactions on Vehicular Technology*, vol. 64, no. 11, pp. 5070–5082, 2014.

[96] D. Wu, X. Zhang, J. Qiu, L. Gu, Y. Saito, A. Benjebbour, and Y. Kishiyama, "A field trial of f-OFDM toward 5G," in *2016 IEEE Globecom Workshops (GC Wkshps).* Washington, USA, 2016, pp. 1–6.

[97] P. Guan, D. Wu, T. Tian, J. Zhou, X. Zhang, L. Gu, A. Benjebbour, M. Iwabuchi, and Y. Kishiyama, "5G Field Trials: OFDM-based Waveforms and Mixed Numerologies," *IEEE Journal on Selected Areas in Communications*, vol. 35, no. 6, pp. 1234–1243, 2017.

[98] F. Di Stasio, M. Mondin, and F. Daneshgaran, "Multirate 5G downlink performance comparison for f-OFDM and w-OFDM schemes with different numerologies," in *2018 international symposium on networks, computers and communications (ISNCC).* Rome, Italy, 2018, pp. 1–6.

[99] H. Chen, J. Hua, F. Li, F. Chen, and D. Wang, "Interference Analysis in the Asynchronous f-OFDM Systems," *IEEE Transactions on Communications*, vol. 67, no. 5, pp. 3580–3596, May 2019.

[100] M. Biguesh and A. B. Gershman, "Training-based mimo channel estimation: a study of estimator tradeoffs and optimal training signals," *IEEE transactions on signal processing*, vol. 54, no. 3, pp. 884–893, 2006.

[101] S. Omar, A. Ancora, and D. T. Slock, "Performance analysis of general pilot-aided linear channel estimation in lte ofdma systems with application to simplified mmse schemes," in *2008 IEEE 19th International symposium on personal, indoor and mobile radio communications.* Cannes, France, 2008, pp. 1–6.

[102] F. Argenti, M. Biagini, E. Del Re, and S. Morosi, "Time-frequency mse analysis of linear channel estimation methods for the lte downlink," *Transactions on Emerging Telecommunications Technologies*, vol. 26, no. 4, pp. 704–717, 2015.

[103] M. Raghavendra and K. Giridhar, "Improving channel estimation in ofdm systems for sparse multipath channels," *IEEE Signal Processing Letters*, vol. 12, no. 1, pp. 52–55, 2004.

[104] J. Oliver, R. Aravind, and K. Prabhu, "Sparse channel estimation in ofdm systems by threshold-based pruning," *Electronics Letters*, vol. 44, no. 13, pp. 830–832, 2008.

[105] Y. Zhao and A. Huang, "A Novel Channel Estimation Method for OFDM Mobile Communication Systems Based on Pilot Signals and Transform-domain Processing," in *1997 IEEE 47th Vehicular Technology Conference. Technology in Motion*, vol. 3. Phoenix, USA, 1997, pp. 2089–2093.

[106] Y. Kang, K. Kim, and H. Park, "Efficient dft-based channel estimation for ofdm systems on multipath channels," *IET communications*, vol. 1, no. 2, pp. 197–202, 2007.

[107] M. Soltani, V. Pourahmadi, A. Mirzaei, and H. Sheikhzadeh, "Deep learning-based channel estimation," *IEEE Communications Letters*, vol. 23, no. 4, pp. 652–655, 2019.

[108] A. B. Kihero, M. S. J. Solaija, and H. Arslan, "Multi-numerology multiplexing and inter-numerology interference analysis for 5G," *arXiv preprint arXiv:1905.12748*, 2019.

[109] L. Zhang, A. Ijaz, P. Xiao, and R. Tafazolli, "Multi-service system: An enabler of flexible 5G air interface," *IEEE Communications Magazine*, vol. 55, no. 10, pp. 152–159, 2017.

[110] J. Mao, L. Zhang, P. Xiao, and K. Nikitopoulos, "Interference analysis and power allocation in the presence of mixed numerologies," *IEEE Transactions on Wireless Communications*, vol. 19, no. 8, pp. 5188–5203, 2020.

[111] H. Lin, "Flexible configured OFDM for 5G air interface," *IEEE Access*, vol. 3, pp. 1861–1870, 2015.

[112] M. Fuhrwerk, J. Peissig, and M. Schellmann, "On the design of an FBMC based AIR interface enabling channel adaptive pulse shaping per sub-band," in *2015 23rd European Signal Processing Conference (EUSIPCO)*, Nice, France, Aug 2015, pp. 384–388.

[113] X. Cheng, R. Zayani, H. Shaiek, and D. Roviras, "Analysis and cancellation of mixed-numerologies interference for massive mimo-ofdm ul," *IEEE wireless communications letters*, vol. 9, no. 4, pp. 470–474, 2019.

[114] X. Cheng, R. Zayani, H. Shaiek, and D. Roviras, "Inter-numerology interference analysis and cancellation for massive MIMO-OFDM downlink systems," *IEEE Access*, vol. 7, pp. 177 164–177 176, 2019.

[115] A. B. Kihero, M. S. J. Solaija, and H. Arslan, "Inter-numerology interference for beyond 5G," *IEEE Access*, vol. 7, pp. 146 512–146 523, 2019.

[116] E. Memisoglu, A. B. Kihero, E. Basar, and H. Arslan, "Guard band reduction for 5G and beyond multiple numerologies," *IEEE Communications Letters*, vol. 24, no. 3, pp. 644–647, 2019.

[117] F. Wu, R. Tan, C. Zhang, W. Fan, X. Chen, D. Niyato, and Y. Liu, "Mixed Numerology Interference Recognition Approach for 5G NR," *IEEE Wireless Communications Letters*, vol. 10, no. 10, pp. 2135–2139, 2021.

[118] X. Liu, L. Zhang, J. Xiong, X. Zhang, L. Zhou, and J. Wei, “Peak-to-average power ratio analysis for OFDM-based mixed-numerology transmissions,” *IEEE Transactions on Vehicular Technology*, vol. 69, no. 2, pp. 1802–1812, 2019.

[119] P. H. Brill *et al.*, *Level crossing methods in stochastic models.* Springer, 2008, vol. 13.

[120] X. Liu, X. Zhang, L. Zhang, P. Xiao, J. Wei, H. Zhang, and V. C. Leung, “PAPR reduction using iterative clipping/filtering and ADMM approaches for OFDM-based mixed-numerology systems,” *IEEE Transactions on Wireless Communications*, vol. 19, no. 4, pp. 2586–2600, 2020.

[121] Y. Huang and B. Su, “Circularly pulse-shaped precoding for OFDM: A new waveform and its optimization design for 5G new radio,” *IEEE Access*, vol. 6, pp. 44 129–44 146, 2018.

[122] S. Gökceli, T. Levanen, J. Yli-Kaakinen, T. Riihonen, M. Renfors, and M. Valkama, “PAPR reduction with mixed-numerology OFDM,” *IEEE Wireless Communications Letters*, vol. 9, no. 1, pp. 21–25, 2019.

[123] E. Memisoglu, A. E. Duranay, and H. Arslan, “Numerology Scheduling for PAPR Reduction in Mixed Numerologies,” *IEEE Wireless Communications Letters*, 2021.

[124] A. F. Demir and H. Arslan, “Inter-numerology interference management with adaptive guards: A cross-layer approach,” *IEEE Access*, vol. 8, pp. 30 378–30 386, 2020.

[125] A. Yazar and H. Arslan, “Reliability enhancement in multi-numerology-based 5G new radio using ini-aware scheduling,” *EURASIP Journal on Wireless Communications and Networking*, vol. 2019, no. 1, p. 110, 2019.

[126] P. K. Korrai, E. Lagunas, A. Bandi, S. K. Sharma, and S. Chatzinotas, “Joint Power and Resource Block Allocation for Mixed-Numerology-Based 5G Downlink Under Imperfect CSI,” *IEEE Open Journal of the Communications Society*, vol. 1, pp. 1583–1601, 2020.

[127] S. McWade, M. F. Flanagan, J. Mao, L. Zhang, and A. Farhang, “Resource Allocation for Mixed Numerology NOMA,” *arXiv preprint arXiv:2102.01005*, 2021.

[128] L. Zhang, A. Ijaz, P. Xiao, and R. Tafazolli, "Channel Equalization and Interference Analysis for Uplink Narrowband Internet of Things (NB-IoT)," *IEEE Communications Letters*, vol. 21, no. 10, pp. 2206–2209, 2017.

[129] B. Yang, L. Zhang, D. Qiao, G. Zhao, and M. A. Imran, "Narrowband internet of things (nb-iot) and lte systems co-existence analysis," in *2018 IEEE Global Communications Conference (GLOBECOM).* Abu Dhabi, United Arab Emirates, 2018, pp. 1–6.

[130] L. Marijanovic, S. Schwarz, and M. Rupp, "A Novel Optimization Method for Resource Allocation based on Mixed Numerology," in *ICC 2019-2019 IEEE International Conference on Communications (ICC).* Shanghai, China, 2019, pp. 1–6.

[131] S. B. Weinstein, "The history of orthogonal frequency-division multiplexing [history of communications]," *IEEE Communications Magazine*, vol. 47, no. 11, pp. 26–35, 2009.

[132] A. Peled and A. Ruiz, "Frequency domain data transmission using reduced computational complexity algorithms," in *ICASSP'80. IEEE International Conference on Acoustics, Speech, and Signal Processing*, vol. 5. Denver, USA, 1980, pp. 964–967.

[133] L. Cimini, "Analysis and simulation of a digital mobile channel using orthogonal frequency division multiplexing," *IEEE transactions on communications*, vol. 33, no. 7, pp. 665–675, 1985.

[134] L. R. Rabiner and B. Gold, "Theory and application of digital signal processing," *Englewood Cliffs: Prentice-Hall*, 1975.

[135] V. Oppenheim Alan, S. Willsky Alan, and T. Young Ian, "Signals and systems," 1997.

[136] J. G. Proakis and D. G. Manolakis, "Digital signal processing," *MPC, New York*, 1992.

[137] A. V. Oppenheim, *Discrete-time signal processing.* Pearson Education India, 1999.

[138] J. G. Andrews, S. Buzzi, W. Choi, S. V. Hanly, A. Lozano, A. C. K. Soong, and J. C. Zhang, "What will 5G be?" *IEEE J. Select. Areas Commun.*, vol. 32, no. 6, pp. 1065–1082, 2014.

[139] V. F. Monteiro, M. Ericson, and F. R. P. Cavalcanti, "Fast-RAT Scheduling in a 5G Multi-RAT Scenario," *IEEE Communications Magazine*, vol. 55, no. 6, pp. 79–85, 2017.

[140] L. Zhang, P. Xiao, A. Zafar, A. ul Quddus, and R. Tafazolli, "FBMC system: An insight into doubly dispersive channel impact," *IEEE Transactions on Vehicular Technology*, vol. 66, no. 5, pp. 3942–3956, 2017.

[141] A. Ghosh, N. Mangalvedhe, R. Ratasuk, B. Mondal, M. Cudak, E. Visotsky, T. A. Thomas, J. G. Andrews, P. Xia, H. S. Jo *et al.*, "Heterogeneous cellular networks: From theory to practice," *IEEE communications magazine*, vol. 50, no. 6, pp. 54–64, 2012.

[142] H. Claussen, L. T. Ho, and L. G. Samuel, "An overview of the femtocell concept," *Bell Labs Technical Journal*, vol. 13, no. 1, pp. 221–245, 2008.

[143] R1-166103, "Discussion on flexible frame structure with different numerologies," 3GPP TSG RAN1 Meeting #86, Tech. Rep., August 2016. [Online]. Available: https://www.3gpp.org/ftp/tsg_ran/WG1_RL1/TSGR1_86/Docs

[144] S. Song and A. Singer, "Pilot-aided OFDM Channel Estimation in the Presence of the Guard Band," *IEEE Transactions on Communications*, vol. 55, no. 8, pp. 1459–1465, 2007.

[145] S. Coleri, M. Ergen, A. Puri, and A. Bahai, "Channel Estimation Techniques Based on Pilot Arrangement in OFDM Systems," *IEEE Transactions on Broadcasting*, vol. 48, no. 3, pp. 223–229, 2002.

[146] D. Diallo, M. Hélard, L. Cariou, and R. Rabineau, "DFT Based Channel Estimation Methods for MIMO-OFDM Systems," *Vehicular Technologies: Increasing Connectivity*, pp. 97–114, 2011.

[147] O. Edfors, M. Sandell, J.-J. Van de Beek, S. K. Wilson, and P. O. Borjesson, "OFDM Channel Estimation by Singular Value Decomposition," *IEEE Transactions on Communications*, vol. 46, no. 7, pp. 931–939, 1998.

[148] Y. Li, L. J. Cimini, and N. R. Sollenberger, "Robust Channel Estimation for OFDM Systems with Rapid Dispersive Fading Channels," *IEEE Transactions on Communications*, vol. 46, no. 7, pp. 902–915, 1998.

[149] S. K. Sengijpta, "Fundamentals of Statistical Signal Processing: Estimation Theory," 1995.

[150] D. Mattera and M. Tanda, "Windowed OFDM for small-cell 5G uplink," *Physical Communication*, vol. 39, p. 100993, 2020.

[151] J. Abdoli, M. Jia, and J. Ma, "Filtered OFDM: A new waveform for future wireless systems," in *2015 IEEE 16th International Workshop on Signal Processing Advances in Wireless Communications (SPAWC).* Stockholm, Sweden, 2015, pp. 66–70.

[152] I. Afolabi, T. Taleb, K. Samdanis, A. Ksentini, and H. Flinck, "Network slicing and softwarization: A survey on principles, enabling technologies, and solutions," *IEEE Communications Surveys & Tutorials*, vol. 20, no. 3, pp. 2429–2453, 2018.

[153] P. Popovski, K. F. Trillingsgaard, O. Simeone, and G. Durisi, "5G wireless network slicing for eMBB, URLLC, and mMTC: A communication-theoretic view," *IEEE Access*, vol. 6, pp. 55 765–55 779, 2018.

[154] J. Harding, G. Powell, R. Yoon, J. Fikentscher, C. Doyle, D. Sade, M. Lukuc, J. Simons, J. Wang *et al.*, "Vehicle-to-vehicle communications: readiness of V2V technology for application." United States. National Highway Traffic Safety Administration, Tech. Rep., 2014. [Online]. Available: https://rosap.ntl.bts.gov/view/dot/2799900

[155] S. S. S. R. Depuru, L. Wang, V. Devabhaktuni, and N. Gudi, "Smart meters for power grid—challenges, issues, advantages and status," in *2011 IEEE/PES Power Systems Conference and Exposition.* Phoenix, USA, 2011, pp. 1–7.

[156] L. Marijanovic, S. Schwarz, and M. Rupp, "Multi-user resource allocation for low latency communications based on mixed numerology," in *2019 IEEE 90th Vehicular Technology Conference (VTC2019-Fall).* Honolulu, USA, 2019, pp. 1–7.

[157] R. Horst and H. Tuy, *Global optimization: Deterministic approaches.* Springer Science & Business Media, 2013.

[158] W. Yu, G. Ginis, and J. M. Cioffi, "Distributed multiuser power control for digital subscriber lines," *IEEE Journal on Selected areas in Communications*, vol. 20, no. 5, pp. 1105–1115, 2002.

[159] R. Lui and W. Yu, "Low-complexity near-optimal spectrum balancing for digital subscriber lines," in *IEEE International Conference on*

Communications, 2005. ICC 2005. 2005, vol. 3. Seoul, Korea (South), 2005, pp. 1947–1951.

[160] J. Papandriopoulos and J. S. Evans, "Low-complexity distributed algorithms for spectrum balancing in multi-user DSL networks," in *2006 IEEE International Conference on Communications*, vol. 7. Istanbul, Turkey, 2006, pp. 3270–3275.

[161] S. Boyd, S. P. Boyd, and L. Vandenberghe, *Convex optimization.* Cambridge university press, 2004.

[162] Q. Wu and R. Zhang, "Towards smart and reconfigurable environment: Intelligent reflecting surface aided wireless network," *IEEE Communications Magazine*, vol. 58, no. 1, pp. 106–112, 2019.

[163] M. Cui, G. Zhang, and R. Zhang, "Secure wireless communication via intelligent reflecting surface," *IEEE Wireless Communications Letters*, vol. 8, no. 5, pp. 1410–1414, 2019.

[164] Q. Wu and R. Zhang, "Intelligent reflecting surface enhanced wireless network via joint active and passive beamforming," *IEEE Transactions on Wireless Communications*, vol. 18, no. 11, pp. 5394–5409, 2019.